

**Elastodynamic Modeling of Fluid-Loaded
Cylindrical Shells with Multiple Layers and
Internal Attachments**

by

David C. Ricks

M.S., Ocean Engineering, M.I.T. (1983)

B.S., Ocean Engineering, M.I.T. (1983)

Submitted to the Department of Ocean Engineering
in partial fulfillment of the requirements for the degree of


Doctor of Philosophy in Acoustics

at the


Massachusetts Institute of Technology

May 1994

© Massachusetts Institute of Technology 1994. All rights reserved.

Author 

Department of Ocean Engineering

May 6, 1994


Certified by 

Henrik Schmidt

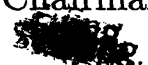
Professor, Massachusetts Institute of Technology

Thesis Supervisor

Accepted by

Professor A. Douglas Carmichael

Chairman, Departmental Graduate Committee

 Eng.
MASSACHUSETTS INSTITUTE

JUN 20 1994

This page is blank.

Elastodynamic Modeling of Fluid-Loaded Cylindrical Shells with Multiple Layers and Internal Attachments

by

David C. Ricks

Submitted to the Department of Ocean Engineering
on May 6, 1994, in partial fulfillment of the
requirements for the degree of
Doctor of Philosophy in Acoustics

Abstract

First, a technique is developed to model the dynamics of cylindrical shells that can have multiple viscoelastic layers and external compliant coatings. The technique is based on well-known wavenumber transform properties, with the novel feature here being the development of a Direct Global Matrix formulation (DGM) to obtain numerically stable solutions over a wide range of axial wavenumbers and circumferential orders. The resulting computer program can model any combination of solid, fluid, and vacuum layers, arranged in any order. Fluid-loaded shells are modeled by letting the outermost layer be a fluid that radiates to infinity. The excitations used here are time-harmonic ring forces that can push on any solid layer in the radial, circumferential, or axial directions. The ring forces can have a linear phase shift around the circumference of the shell, so helical waves can be excited and studied for any circumferential order. Analytically, the order can be complex, although the software is presently implemented for real orders.

Second, the method is used as a reference model to check the accuracy of three different thin shell theories. Cases of agreement and disagreement are shown and interpreted.

Third, a technique is developed to attach a thin elastic plate inside the DGM shell model. To make the problem more tractable, the plate is described with a thin plate theory, while the DGM shell model is based on the full 3D elastic theory. The approximate nature of the plate theory introduces a slight incompatibility at the interface between the two theories, so a technique is developed to connect the two theories. Newton's third law is satisfied in an integral sense by matching the resultant forces and moments, and structural continuity is satisfied in an integral sense by matching the instantaneous power transferred between the plate and the shell.

Finally, it is shown how these techniques can be used to model the scattering of acoustic waves from multi-layered shells.

Thesis Supervisor: Henrik Schmidt

Title: Professor, Massachusetts Institute of Technology

Acknowledgments

First, I thank my Mom and Dad. When I was little, they didn't get me every toy I wanted, but they did get me any book I wanted. Their values and their support have made a lifetime of continuing education possible. This thesis is dedicated to my parents, Robert and Patricia Ricks.

Second, I thank my advisor and supervisor, Henrik Schmidt. His Direct Global Matrix approach was a strong idea that was ripe for development in cylindrically layered systems. I was fortunate to be the right person in the right place at the right time to make this contribution to acoustics. Henrik has also been a very supportive figure in my professional development.

Third, everyone else in my thesis committee was helpful, as well. Yueping Guo and I shared spirited discussions, which prepared me to defend my point of view. Leo Felsen gave us his valuable point of view about travelling waves in the circumferential direction. Paul Sclavounos asked elegant questions.

Many other people played supporting roles. Ira Dyer was essential in getting this funding, and also in keeping this funding by keeping us directed toward the sponsor's point of view. I thank my office mates for good times and intellectual rapport: Matt Conti, Joe Bondaryk, Tarun Kapoor, and Chick Corrado. And, of course, the women downstairs really run the place: Marilyn Staruch, Denise Cormier, and Sabina Rataj.

Also, I should thank some musicians for supporting my continuing development during this period of my life, as I am a trumpet and flügelhorn player, composer, and band leader. I thank Jamshied Sharifi (synthesizer) and Ole Mathisen (saxaphones) for their help with the issues of signal processing and amplification. Also, thanks to Ali Azarbajani (trumpet, flügelhorn, and now bass) for comraderie.

Finally, I thank some good friends who give my life pleasure and meaning: John Simmons, Forrest Buzan, Betsy Gynn, Virginia Clark, and Christine Paquay.

This page is blank.

Contents

Nomenclature	11
1 Introduction	15
1.1 Previous Work	15
1.2 The MIT/NRL Project	18
1.3 This Thesis	19
2 A Technique for Layered Shells	21
2.1 Previous Techniques	21
2.2 Analytical Formulation	23
2.3 The Direct Global Matrix	28
2.4 Stability in Wavenumber	30
2.5 Transforming to Space	33
2.6 Computing Input Power	35
3 Comparison to Thin Shell Models	39
3.1 Thin Shell Theories	41
3.2 Agreement	44

3.2.1	Agreement in Wavenumber	44
3.2.2	Agreement in Space	49
3.2.3	Agreement in Power Input	51
3.3	Disagreement	54
3.3.1	Disagreement for High Frequencies	54
3.3.2	Disagreement for Large Orders	57
3.3.3	Disagreement for Drive Displacements	58
3.3.4	Disagreement for Moment Impedance	61
3.3.5	Disagreement for Very Low Frequencies	63
3.4	Accounting for Eccentric Forcing	68
4	A Technique for Attaching a Plate	73
4.1	Possible Approaches	74
4.2	Resultant Forces and Moments	76
4.3	Solution via Admittance Matrices	78
5	Acoustic Scattering	83
5.1	Scattering from Empty Shells	84
5.2	Scattering from Stiffened Shells	89
6	Conclusions and Future Work	91
6.1	Structural Acoustics	91
6.2	The DGM Method Itself	97
6.2.1	Numerical Stability	97

6.2.2	Numerical Accuracy	99
6.2.3	Numerical Efficiency	101
6.3	Other Applications	102
Appendices		103
A Particular Solutions for Time-Harmonic Ring Forces		105
A.1	Radial Ring Forcing	107
A.2	Circumferential Ring Forcing	109
A.3	Axial Ring Forcing	110
A.4	Wronskians	111
B Suppressing Wrap-Around		113
B.1	Definitions of Transforms	113
B.2	Wrap-Around	114
B.3	Contour Offset	115
C Elastodynamic Response to a Time-Harmonic Point Force		119
D Branch Cut Implementation		123
D.1	EJP Branch Cuts	124
D.2	Pekeris Branch Cuts	125
E Admittance Matrix for a Thin Elastic Plate		127
E.1	Symmetric Inplane Motions	128
E.2	Flexural Motions	131

E.3	Symmetry vs. Antisymmetry	136
E.4	Checking Admittances	138
F	Admittance Matrix for the DGM Shell Model	141
F.1	Resultant Forces and Moments	141
F.2	Power Transfer	143
F.3	Defining Admittances	146
F.4	Convolution Properties	149
F.5	Evaluating Admittances	151
F.6	Checking Admittances	157
F.7	Velocities for the Empty Shell	159
G	Form Functions	163
G.1	An Obliquely Incident Plane Wave	164
G.2	Cylindrically Spreading Waves	166
G.2.1	Acoustically Soft Body	168
G.2.2	Acoustically Hard Body	169
G.3	Spherically Spreading Waves	170
	Bibliography	175

Nomenclature

Nomenclature for geometry:

r, θ, z The coordinates in the radial, circumferential, and axial directions.

$\mathbf{a}_r, \mathbf{a}_\theta, \mathbf{a}_z$ The unit vectors in the radial, circumferential, and axial directions.

Nomenclature for the 3D equations of elastodynamics:

n The layer number. The layers are numbered from $n = 1$ to N , where layer 1 includes $r = 0$ and layer N extends to infinity.

N The layer number of the outermost layer.

R_n The outer interface of layer n . The system has $N - 1$ interfaces, because layer N does not have an outer interface.

ρ_n The density of layer n .

λ_n, μ_n The Lamé constants for layer n .

$u_r|_n, u_\theta|_n, u_z|_n$ The displacements in the radial, circumferential, and axial directions, respectively.

\mathbf{u}_n The vector displacement $\mathbf{u}_n = \mathbf{a}_r u_r|_n + \mathbf{a}_\theta u_\theta|_n + \mathbf{a}_z u_z|_n$.

$\sigma_{rr}|_n, \sigma_{r\theta}|_n, \sigma_{rz}|_n$ The stresses on the positive r -face of an infinitesimal element in layer n , acting in the r, θ , and z -directions, respectively.

\mathbf{f}_n The applied force per unit volume in layer n .

c_{cn}, c_{sn} The speed of compression and shear waves in layer n , respectively, where $c_{cn} = \sqrt{(\lambda_n + 2\mu_n)/\rho_n}$ and $c_{sn} = \sqrt{\mu_n/\rho_n}$.

h_n, k_n The wavenumbers for compression and shear waves in layer n , respectively, where $h_n = \omega/c_{cn}$ and $k_n = \omega/c_{sn}$.

h_{rn}, k_{rn} The radial wavenumbers for compression and shear waves, respectively, where $h_{rn}^2 = h_n^2 - s^2$ and $k_{rn}^2 = k_n^2 - s^2$.

ϕ_n, ψ_n, χ_n Displacement potentials for the homogeneous waves in layer n .

H, P As superscripts, H indicates a homogeneous solution and P indicates a particular solution. For example, $\mathbf{u}_n = \mathbf{u}_n^H + \mathbf{u}_n^P$.

Nomenclature for transforms:

- ω The frequency in radians per second. The frequency ω may be complex.
- s The axial wavenumber of a Fourier integral transform. The axial wavenumber s may be complex.
- ν The circumferential order, which may be complex.
- $\hat{\quad}$ The hat over a quantity indicates the axial wavenumber transform has been applied to transform that quantity to the axial wavenumber domain.

Nomenclature for the global matrix equations:

- $\{V\}$ A vector containing the known displacements and stresses for the particular solutions, observed at the interfaces. Also called “the right-hand side.”
- $\{A\}$ A vector containing the unknown amplitudes of the homogeneous waves. The entries in $\{A\}$ for layer n are called A_n through F_n .
- $[G]$ The direct global matrix. The boundary conditions at the interfaces are stated as $[G]\{A\} = \{V\}$. The entries in $[G]$ and $\{A\}$ are suitably normalized to work together to give stable solutions.
- g_{ij} The individual entries that make up the global matrix.

Nomenclature for ring forces:

- r' The radius of a ring force.
- F_r, F_θ, F_z The magnitudes of the ring forces acting in the radial, circumferential, and axial directions, respectively. The magnitudes have units of force per length around the circumference of the ring.
- ϕ_I, ψ_I, χ_I Displacement potentials for the particular solutions observed over $0 \leq r < r'$ (i.e., the interior region).
- ϕ_E, ψ_E, χ_E Displacement potentials for the particular solutions observed over $r' < r < \infty$ (i.e., the exterior region).

Nomenclature for a thin cylindrical shell:

- U_r, U_θ, U_z The displacements of the middle surface of a cylindrical shell in the Donnell thin shell theory. They are 2D functions of θ and z .
- T_s, R_s The thickness and mean radius of the shell.
- E_s, G_s, ν_s The Young's modulus, shear modulus, and Poisson ratio of the shell.
- ρ_s The density of the shell material.
- c_{Ls} The speed of longitudinal waves in a thin flat plate made of the same material as the shell, given by $c_{Ls} = \sqrt{E_s/[\rho_s(1 - \nu_s^2)]}$.
- ∇_s^4 The biharmonic operator for the displacements of the shell. Considering that the displacements are observed at $r = R_s$, I define $\nabla_s^4 \equiv R_s^{-4} \partial^4 / \partial \theta^4 + 2R_s^{-2} \partial^4 / \partial \theta^2 \partial z^2 + \partial^4 / \partial z^4$.
- ω_r The ring frequency of the shell in radians per second. The ring frequency is the breathing mode of the shell in vacuum. This is predicted by the Donnell equations to be $\omega_r \equiv c_{Ls}/R_s$.

Nomenclature for beam bending of the shell:

- $U_b(z)$ The transverse displacement of a beam as a function of z .
- I_b The cross-sectional moment of inertia of a beam, in units of length to the fourth power. For a thin shell acting as a beam, $I_b \approx 2\pi R_s^3 T_s / \sqrt{2}$.
- ρ_b The linear density of a beam, in units of mass per length. For a thin shell acting as a beam, $\rho_b \approx 2\pi R_s T_s \rho_s$.
- k_b The flexural wavenumber of a beam in classical bending theory. For a thin shell acting as a beam, $k_b^4 = [\rho_b / (E_s I_b)] \omega^2$.

Nomenclature for a thin flat plate:

- $U_{rp}, U_{\theta p}, U_{zp}$ The displacements of particles in a flat plate in the Mindlin plate theory. In the Mindlin theory, $U_{rp}(r, \theta, z)$ and $U_{\theta p}(r, \theta, z)$ are 3D functions, while $U_{zp}(r, \theta)$ is 2D.
- T_p, R_p The thickness and outer radius of the plate.
- E_p, G_p, ν_p The Young's modulus, shear modulus, and Poisson ratio of the plate.
- ρ_p The density of the plate material.
- M_p The mass of the plate, given by $M_p = \rho_p \pi R_p^2 T_p$.
- c_{Lp} The speed of longitudinal waves in a thin flat plate, given by $c_{Lp} = \sqrt{E_p / [\rho_p (1 - \nu_p^2)]}$.
- D_c The bending stiffness given by the classical theory of plate bending, given by $D_c = E_p T_p^3 / [12(1 - \nu_p^2)] = \rho_p c_{Lp}^2 T_p^3 / 12$.
- k_c The flexural wavenumber given by the classical theory of plate bending, given by $k_c^4 = \rho_p T_p \omega^2 / D_c = 12 \omega^2 / (c_{Lp}^2 T_p^2)$.
- F_r, F_θ, F_z Resultant forces applied to the outer edge of a circular plate. The forces act in the r , θ , and z -directions, respectively.
- M_r, M_θ Resultant moments applied to the outer edge of a circular plate. M_r is the twisting moment about the r -axis, and M_θ is the bending moment about the θ -axis.

Miscellaneous:

- $H_\nu^*(x)$ A Hankel function of the 1st kind, normalized as $[(x/2)^\nu / \Gamma(\nu)] H_\nu^{(1)}(x)$.
- $J_\nu^*(x)$ A Bessel function of the 1st kind, normalized as $[\Gamma(\nu) / (x/2)^\nu] J_\nu(x)$.
- F_o The magnitude of a time-harmonic point force.
- $\langle \Pi \rangle$ Time-averaged power flow.
- α The angle of integration in the s -plane for computing the time-averaged power injected by an applied force.
- β The angle of incidence for an obliquely incident plane wave.

Chapter 1

Introduction

This thesis was written as part of a project to study how acoustic waves in water scatter off of cylindrical metal shells that contain internal stiffeners and structures. The basic question being asked is, “What affects the scattering?” For example, how is the scattering affected by the orientation of a cylindrical shell relative to an incident plane wave? How is the scattering affected by internal stiffeners and structures? What else might be important? Or, to ask these questions in a more abstract way, what patterns can be discovered in data from scattering experiments?

1.1 Previous Work

Of course, acoustic scattering from shells has been studied before. The scattering from infinitely long cylindrical shells has been computed for the case of acoustic plane waves at normal incidence, using thin-shell equations [1] [2] and using the full elastodynamic equations [3] [4] [5] [6] [7] [8] [9]. The case of obliquely incident plane waves has been computed for the infinite cylindrical shell using the full elastodynamic equations [10] [11]. Also, spherical shells have been studied, using thin-shell equations [1] [12], the full elastodynamic equations [13], and physical experiments [14].

However, all of the papers mentioned above model empty shells that contain no internal structures. Such simple models are educational to some degree, but real objects like submarines contain internal stiffeners and structures, and we would like to know how these structural details might affect the scattering. To address this issue, a few papers have computed the dynamics of infinite cylindrical shells containing internal stiffeners or structures, in vacuum [15] [16] [17] and with external fluid loading [18] [19] [20].

Ultimately, though, any real applications will involve scattering from *finite* cylindrical shells, *with* internal stiffeners and structures. Finite cylindrical shells will exhibit some effects that have not yet been seen in the references listed above. For example, a finite cylindrical shell can be hit on its endcap by an incident wave traveling parallel to the shell's axis, while the infinite cylindrical shell cannot be hit this way. Also, if an obliquely incident plane wave hits a finite cylindrical shell, then the structural waves excited in the shell will build up as a function of time t and axial location z . In contrast, if an obliquely incident plane wave hits an infinite cylindrical shell, then the incident wave was always touching the shell back in time $t \rightarrow -\infty$ and space $z \rightarrow -\infty$. Thus, an obliquely incident "transient" plane wave hitting an infinite cylindrical shell forms a "steady-state" pattern in some sense, like a ship traveling at constant speed forming a fixed wake pattern attached to the ship. This artifact will not occur for finite cylindrical shells.

These issues were addressed to some degree by Harari and Sandman, who modeled a finite length of a fluid-loaded shell with internal stiffeners [21]. However, the shell in their model was set in between rigid baffles that extended to infinity in the axial direction, so the issue of endcaps was avoided. Also, Rumerman studied the role of membrane waves in the scattering from finite shells in water, where the shells had flat endcaps [22]. However, Rumerman's study emphasized the role of the membrane waves excited by acoustic waves at $\pm 35^\circ$ from normal incidence, so there is still more to learn about the physics of near-axial incidence and the role of other endcap configurations.

Also, a mention should be made here about the way we look at physics in terms of Fourier transform relations. The classical Fourier transform between time and frequency involves integrals over all time t and all frequency ω :

$$f(t) = \int_{-\infty}^{\infty} F(\omega)e^{-i\omega t}d\omega \quad \iff \quad F(\omega) = \frac{1}{2\pi} \int_{-\infty}^{\infty} f(t)e^{i\omega t}dt$$

These equations define a “time-domain representation” $f(t)$ and a “frequency-domain representation” $F(\omega)$. This approach is a powerful tool for *solving differential equations*, but it’s often a poor tool for *interpreting data*. For example, scattering data has commonly been presented in the frequency domain as the “form function,” which is the Fourier transform $F(\omega)$ of the pressure observed in the far-field, normalized to remove the effect of geometric spreading. This function is useful to some degree, but it cannot show us *when* different contributions to the scattering arrived. Thus, it will be helpful to explore more modern definitions of “time-frequency representations” that seek to show how the frequency content of a signal depends on time (or, how the time content of a signal depends on frequency). For future reference, some good tutorial papers on time-frequency representations have been written by Hlawatsch and Boudreaux-Bartels [23] and Cohen [24]. A paper by Hodges, Power, and Woodhouse applies one time-frequency technique (the short-time Fourier transform) to the vibrations of cylindrical shells [25].

Also, just as it will be helpful to go beyond the classical duality between time and frequency, it will also be helpful to explore modern signal processing techniques for filtering in space, such as beamforming. Acoustic fields are 4-dimensional, involving time and 3 spatial dimensions, and we need all the help we can get in interpreting them. Just as the physical interactions between the various wave types and the structural junctions may be localized roughly in time, these interactions may also be localized roughly in space.

1.2 The MIT/NRL Project

To address these issues, the Office of Naval Research (ONR) is presently funding basic research in the structural acoustics of fluid-loaded shells. One of the projects funded by ONR involves the Massachusetts Institute of Technology (MIT) and the Naval Research Laboratory (NRL) in Washington, DC. At the center of the MIT/NRL project is a series of physical experiments, where air-filled cylindrical shells were immersed in a tank of water, and bursts of sound were scattered off of them.

All of the shells have the same external dimensions and thickness, but some of the shells were empty, some were stiffened internally by mass-like rings, and some were stiffened by the mass-like rings and contained rubber mounts holding metal masses and plastic rods. This collection of shells was designed so the empty shells would allow the identification of simple, fundamental effects associated with their finite nature, and the more complicated shells would allow some investigation into the issues of internal structures.

The experiments cover the so-called “mid-frequency” range, where the wavelengths in the water are roughly the size of the shell. This is quantified here to be the range $2 < ka < 12$, where k is the wavenumber in water and a is the radius of the shell. This frequency range corresponds to roughly 1/2 to 3 times the ring frequency of the shell.

To date, this project has produced one Ph.D. thesis at MIT that discusses the physical effects that dominate the scattering for a range of angles around broadside incidence [26]. Another Ph.D. thesis at MIT will discuss the physical effects that dominate the scattering for a range of angles around axial incidence.

1.3 This Thesis

This thesis, being just one part of the MIT/NRL project, is narrower in scope. In this thesis, I consider mathematical models of cylindrical shells that are infinitely long. The infinite length allows me to use Fourier integral transforms from space to wavenumber, which leads to separation of variables and a solution of the full 3D equations of elastodynamics. This satisfies a separate research agenda to develop a solution technique for cylindrically layered viscoelastic media, with future applications to multi-layered shells, geoacoustics, and ultrasonic non-destructive testing. But how does my study of infinitely long shells support the MIT/NRL program, which seeks to understand finite cylindrical shells? This question has several answers:

- I model the shell with the 3D equations of elastodynamics. Thus, my shell model serves as a “reference model” to check the accuracy of the more commonly used thin-shell equations. Then, if the thin-shell equations are judged to be physically realistic, then those thin-shell equations can be used with confidence in the formulation of other numerical methods for finite shells.
- The waves that propagate along an infinitely long cylindrical shell can be considered to be Platonic ideals of the waves that travel along a finite cylindrical shell. In this sense, the infinite length of a shell can be seen as a beneficial feature, because it allows us to identify the phase speed and radiation damping of the different types of waves that can be supported by the shell, and there will be no complicating effects from the ends of the shell. The software developed in this thesis allows us to study such waves in the spatial domain or in the wavenumber domain.
- In this thesis, I develop a new technique to model the attachment of a thin flat plate to my full 3D elastodynamic shell model. My technique involves an approximate theory for the plate, so the resulting model cannot be considered to be a reference model. However, my model can be used to verify the formulation

and implementation of similar models developed by other researchers who have used thin shell and thin plate theories exclusively.

- It is possible to use the modeling techniques developed here to compute coefficients for the reflection and transmission of various wave types at the welded joint between the shell and the flat plate. In such a study, the infinite length of the shell can be seen as a beneficial feature, because would allow us to study the interaction effects apart from interference with the ends of the shell.
- My numerical shell models are general enough to model any combination of solid, fluid, and vacuum layers, arranged in any order. Viscoelastic layers can be added to the model simply by adding such layers to an input data file. Thus, my models can be used to support research investigating the effectiveness of adding viscoelastic layers to finite shells.

Chapter 2

A Technique for Layered Shells

This chapter develops a technique for modeling the dynamics of cylindrical shells that can have multiple layers and external compliant coatings. The technique is based on the full 3D equations of elastodynamics. The shells will be excited by time-harmonic ring forces. Other excitations can easily be included in the future.

2.1 Previous Techniques

Scattering and radiation problems involving elastic shells are commonly modeled using “thin shell” equations [1] [27] [28] [29]. These equations are relatively simple because they represent the shell’s displacements, stresses, and moments as 2D fields observed at the average radius of the shell.

However, there are several motivations for modeling elastic shells with the full 3D equations of elastodynamics. The full 3D equations can model multi-layered shells that have multiple viscoelastic layers and external compliant coatings. The full 3D equations can represent thicker shells, and shells at higher frequencies. Also, the full 3D equations can more realistically represent the way that internal stiffeners interact with the shell and cause coupling between different wave types.

To model cylindrical shells with the full 3D equations, we need a numerical method that addresses two causes of numerical instability. The first problem is that flexural waves exist in the full elastodynamic theory as the interference of compression and shear waves that are evanescent across the thickness of the shell. Therefore, evanescence across the thickness must be represented accurately, and the numerical method must be stable when there is exponential growth and decay across the thickness. The second problem arises when the radial dependence of the problem is described with Bessel functions. By definition, Bessel functions will underflow and overflow when the circumferential order is large and the radial argument is small. Therefore, the method must involve Bessel functions computed with some normalization for large orders and small arguments.

Previously, the full elastodynamic equations have been used to model infinitely long cylindrical shells excited by acoustic plane waves at normal incidence [3] [4] [5] [6] [7] [8] [9] and oblique incidence [10] [11]. However, these papers offer no way to attach internal stiffeners, so they cannot investigate the issues of stiffener attachment and structural complexity, and the incident acoustic plane wave has no energy at the subsonic flexural wavenumbers of the shell.

Another approach is to discretize the shell in the radial direction using finite element or finite difference methods [30]. However, we know that flexural waves arise from the interference of compression and shear waves that decay exponentially across the thickness of the shell, and these exponentials are not represented elegantly by this approach.

Another approach is to use propagator matrices [31]. In geoacoustics, this has been known as the Thomson-Haskell approach [32] [33]. It has been used to model axisymmetric wave propagation in shells [34] [35] and circularly layered boreholes [36]. Also, solutions have been computed for circularly layered boreholes excited by non-axisymmetric sources [37] [38]. However, this approach requires special numerical effort to maintain numerical stability when there is evanescence across layers. Also, it is not clear how the matrices should be normalized for large circumferential orders.

Instead, we will here apply the Direct Global Matrix approach (DGM). This approach was developed for plane layered viscoelastic systems by Schmidt and Jensen [39], and recently applied to spherically layered systems by Schmidt [40]. The primary advantage of this approach is that it gives numerically stable solutions when there is evanescence across layers, and it does this without special numerical treatment. A secondary advantage is that the global matrix equations are assembled without the multiplication of propagator matrices. A more detailed comparison of DGM to propagator matrices is presented by Jensen et al [41].

This thesis takes the logical step of developing a global matrix method for cylindrically layered systems. The important new features are the choice of Bessel functions, the normalization of the Bessel functions, and the use of ring forces. The resulting method is numerically stable over a wide range of axial wavenumbers and circumferential orders. Thus, it allows for ring stiffeners to be modeled to study scattering and radiation problems. Also, other excitations can easily be incorporated into the method. The generality of the formulation will allow it to be applied to multi-layered shells, shells coated with rubber, and the borehole problem in geoacoustics.

2.2 Analytical Formulation

In this chapter, the media are cylindrically layered, as shown in Fig. 2-1. A cylindrical coordinate system $\{r, \theta, z\}$ is introduced, with the z -axis coincident with the axis of the cylindrical layers. The layers are numbered from $n = 1$ to $n = N$, where layer 1 includes $r = 0$ and layer N extends to infinity. We let R_n be the radius of the outer

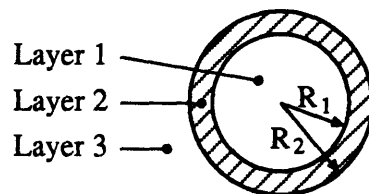


Figure 2-1: Cylindrically layered viscoelastic system.

interface of layer n . All layers are isotropic and homogeneous viscoelastic continua with Lamé constants λ_n and μ_n and density ρ_n . The subscript n refers to the layer number.

If layer n is a solid, then the displacement field \mathbf{u}_n is governed by the 3D equations of elastodynamics, as shown in several textbooks [42] [43] [44] [45] [46]:

$$(\lambda_n + 2\mu_n)\nabla\nabla \cdot \mathbf{u}_n - \mu_n\nabla \times \nabla \times \mathbf{u}_n + \mathbf{f}_n = \rho_n\ddot{\mathbf{u}}_n \quad (2.1)$$

where \mathbf{f}_n is the applied force per unit volume in layer n . This system of equations governs the propagation of compression and shear waves, with the wave speeds:

$$c_{cn} = \sqrt{(\lambda_n + 2\mu_n)/\rho_n} \quad c_{sn} = \sqrt{\mu_n/\rho_n}$$

respectively, so their wavenumbers are:

$$h_n = \omega/c_{cn} \quad k_n = \omega/c_{sn}$$

respectively. If layer n is a fluid, then we let $\mu_n = 0$ and $\mathbf{f}_n = 0$ in Eq. (2.1), and we ignore any terms involving c_{sn} and k_n in the equations that follow.

Using complex notation, I give the ring forces a time dependence of $e^{-i\omega t}$, and I let this factor be implied in the following. Of course, this is a common practice in acoustics, because it reduces the dimension of the partial differential equations involved, yet it gives no loss of generality, because the time dependence of other forcing functions can be synthesized from time-harmonic forces by using a Fourier integral over frequency.

Similarly, I give the ring forces an angular dependence of $e^{i\nu\theta}$, where ν is the order, and I let this factor be implied from here on. Again, this reduces the dimension of the partial differential equations, yet it gives no loss of generality, because the angular dependence of other forcing functions can be synthesized from angularly-harmonic forces by using a Fourier series or a Fourier integral. A synthesis that sums over

integer orders is a synthesis of modes, while an integral over complex orders is a synthesis of traveling waves [47] [48] [49] [50]. The formulation derived here is suitable for either approach.

Thus, I give all forces and solutions an implied common factor of $e^{i(\nu\theta - \omega t)}$, which has the form of a wave traveling in the θ -direction. Physically, such forces will excite helical waves on the shell. Viscoelastic attenuation can be represented by letting the Lamé constants be complex.

The global matrix method considers the displacement field in each layer as the superposition of homogeneous and particular solutions

$$\mathbf{u}_n = \mathbf{u}_n^H + \mathbf{u}_n^P$$

The particular solutions \mathbf{u}_n^P are the “free-space” waves that would emanate from the ring forces in layer n if layer n extended over $0 \leq r < \infty$. The homogeneous solutions \mathbf{u}_n^H are source-free waves that add to the free-space waves to satisfy the boundary conditions.

Therefore, the homogeneous field \mathbf{u}_n^H is governed by the equation:

$$(\lambda_n + 2\mu_n)\nabla\nabla \cdot \mathbf{u}_n^H - \mu_n\nabla \times \nabla \times \mathbf{u}_n^H + \rho_n\omega^2\mathbf{u}_n^H = 0$$

Using the Helmholtz vector decomposition theorem [51], this field can be separated into longitudinal and transverse components, and represented in terms of scalar displacement potentials as:

$$\mathbf{u}_n^H = \nabla\phi_n + \nabla \times (\mathbf{a}_z\psi_n) + k_n^{-1} \nabla \times \nabla \times (\mathbf{a}_z\chi_n) \quad (2.2)$$

where \mathbf{a}_z is the direction vector in the z -direction, and the potentials obey the Helmholtz equations:

$$(\nabla^2 + h_n^2)\phi_n = 0 \quad (2.3)$$

$$(\nabla^2 + k_n^2) \psi_n = 0 \quad (2.4)$$

$$(\nabla^2 + k_n^2) \chi_n = 0 \quad (2.5)$$

The factor of k_n^{-1} in Eq. (2.2) gives the three potentials the same units, which will help avoid numerical instability when solving for the potentials.

To further reduce the dimension of the Helmholtz equations (2.3-2.5), I introduce the axial Fourier transforms of all potentials, displacements, and stresses. The transforms have the form:

$$f(r, z) = \int_{-\infty}^{\infty} \hat{f}(r, s) e^{isz} ds \quad (2.6)$$

$$\hat{f}(r, s) = \frac{1}{2\pi} \int_{-\infty}^{\infty} f(r, z) e^{-isz} dz \quad (2.7)$$

where $f(r, z)$ is the field being transformed, s is the wavenumber measured in the axial direction, and the hat ($\hat{}$) denotes the wavenumber transform of a quantity. Applying the integral transform in Eq. (2.7) to the potentials in Eqs. (2.3-2.5) leads to the ordinary differential equations:

$$\frac{d^2 \hat{\phi}_n}{dr^2} + \frac{1}{r} \frac{d\hat{\phi}_n}{dr} + \left(h_{rn}^2 - \frac{\nu^2}{r^2} \right) \hat{\phi}_n = 0 \quad (2.8)$$

$$\frac{d^2 \hat{\psi}_n}{dr^2} + \frac{1}{r} \frac{d\hat{\psi}_n}{dr} + \left(k_{rn}^2 - \frac{\nu^2}{r^2} \right) \hat{\psi}_n = 0 \quad (2.9)$$

$$\frac{d^2 \hat{\chi}_n}{dr^2} + \frac{1}{r} \frac{d\hat{\chi}_n}{dr} + \left(k_{rn}^2 - \frac{\nu^2}{r^2} \right) \hat{\chi}_n = 0 \quad (2.10)$$

where:

$$h_{rn}^2 = h_n^2 - s^2 \quad (2.11)$$

$$k_{rn}^2 = k_n^2 - s^2 \quad (2.12)$$

Equations (2.8-2.10) are solved by Bessel functions [52]. In theory, we could choose any two of the functions J_ν , Y_ν , $H_\nu^{(1)}$, and $H_\nu^{(2)}$. However, in practice, it is essential

to the stability of our numerical method that we represent the potentials as:

$$\hat{\phi}_n = A_n H_\nu^{(1)}(h_{rn}r)/H_\nu^{(1)}(h_{rn}R_{n-1}) + B_n J_\nu(h_{rn}r)H_\nu^{(1)}(h_{rn}R_n) \quad (2.13)$$

$$\hat{\psi}_n = C_n H_\nu^{(1)}(k_{rn}r)/H_\nu^{(1)}(k_{rn}R_{n-1}) + D_n J_\nu(k_{rn}r)H_\nu^{(1)}(k_{rn}R_n) \quad (2.14)$$

$$\hat{\chi}_n = E_n H_\nu^{(1)}(k_{rn}r)/H_\nu^{(1)}(k_{rn}R_{n-1}) + F_n J_\nu(k_{rn}r)H_\nu^{(1)}(k_{rn}R_n) \quad (2.15)$$

where $A_n, B_n, C_n, D_n, E_n,$ and F_n are unknown amplitudes to be determined. Section 2.4 describes why this representation works numerically where others fail.

Incidentally, Eqs. (2.13-2.15) are also convenient for describing the innermost and outermost layers. For the innermost layer, we simply set $A_1 = C_1 = E_1 = 0$, because the potentials there must go as $J_\nu(h_{r1}r)$ and $J_\nu(k_{r1}r)$ to be finite at $r = 0$. For the outermost layer, we set $B_N = D_N = F_N = 0$, because the potentials there must go as $H_\nu^{(1)}(h_{rN}r)$ and $H_\nu^{(1)}(k_{rN}r)$ to satisfy the radiation conditions at infinity.

To solve for the unknown amplitudes, we need to state the boundary conditions, which involve the displacements and stresses at the interfaces. Using Eq. (2.2), I can write the transforms of the displacement components in layer n as:

$$\hat{u}_r^H|_n = \frac{d\hat{\phi}_n}{dr} + \frac{i\nu}{r}\hat{\psi}_n + \frac{is}{k_n} \frac{d\hat{\chi}_n}{dr} \quad (2.16)$$

$$\hat{u}_\theta^H|_n = \frac{i\nu}{r}\hat{\phi}_n - \frac{d\hat{\psi}_n}{dr} - \frac{\nu s}{k_n r}\hat{\chi}_n \quad (2.17)$$

$$\hat{u}_z^H|_n = is\hat{\phi}_n + \frac{k_{rn}^2}{k_n}\hat{\chi}_n \quad (2.18)$$

And, to know the stresses, we write Hooke's law in cylindrical coordinates [53]:

$$\begin{aligned} \sigma_{rr} &= \lambda \nabla \cdot \mathbf{u} + 2\mu \frac{\partial u_r}{\partial r} \\ \sigma_{r\theta} &= \mu \left(\frac{1}{r} \frac{\partial u_r}{\partial \theta} - \frac{u_\theta}{r} + \frac{\partial u_\theta}{\partial r} \right) \\ \sigma_{rz} &= \mu \left(\frac{\partial u_r}{\partial z} + \frac{\partial u_z}{\partial r} \right) \end{aligned}$$

Applying these expressions to the homogeneous field in layer n , the transforms of the

stresses follow as:

$$\hat{\sigma}_{rr}^H|_n = -\lambda_n h_n^2 \hat{\phi}_n + 2\mu_n \left(\frac{d^2 \hat{\phi}_n}{dr^2} - \frac{i\nu}{r^2} \hat{\psi}_n + \frac{i\nu}{r} \frac{d\hat{\psi}_n}{dr} + \frac{is}{k_n} \frac{d^2 \hat{\chi}_n}{dr^2} \right) \quad (2.19)$$

$$\hat{\sigma}_{r\theta}^H|_n = \mu_n \left[\frac{2i\nu}{r} \left(-\frac{\hat{\phi}_n}{r} + \frac{d\hat{\phi}_n}{dr} \right) - \frac{\nu^2}{r^2} \hat{\psi}_n + \frac{1}{r} \frac{d\hat{\psi}_n}{dr} - \frac{d^2 \hat{\psi}_n}{dr^2} + \frac{2\nu s}{k_n r} \left(\frac{\hat{\chi}_n}{r} - \frac{d\hat{\chi}_n}{dr} \right) \right] \quad (2.20)$$

$$\hat{\sigma}_{rz}^H|_n = \mu_n \left[2is \frac{d\hat{\phi}_n}{dr} - \frac{\nu s}{r} \hat{\psi}_n + \frac{k_{rn}^2 - s^2}{k_n} \frac{d\hat{\chi}_n}{dr} \right] \quad (2.21)$$

The particular solutions for ring forces are shown in Appendix A. The unknown amplitudes A_n through F_n can now be determined by involving them in the boundary conditions at the interfaces. This is done by inserting the potentials in Eqs. (2.13-2.15) into Eqs. (2.16-2.21), and organizing the boundary conditions into the global system of equations described in the next section.

2.3 The Direct Global Matrix

The global equations state the boundary conditions in the form

$$[G]\{A\} = \{V\}$$

The vector $\{V\}$ contains the known displacements and stresses associated with the particular solutions \mathbf{u}_n^P for the ring forces in the various layers. The left-hand side contains the unknown displacements and stresses associated with the homogeneous waves \mathbf{u}_n^H , written in terms of a vector $\{A\}$ of the unknown amplitudes and the global matrix $[G]$ composed of coefficients g_{ij} .

The general procedure of arranging the equations is shown by Schmidt and Jensen [39], and a specific example is given in this paragraph. To model a fluid-loaded shell, I let the number of layers N be three, where the inner layer number 1 is a vacuum, layer number 2 is an elastic solid, and the outer layer number 3 is a fluid. Considering

the excitations to be ring forces in layer number 2, the global system of equations is:

$$[G] \begin{pmatrix} A_2 \\ B_2 \\ C_2 \\ D_2 \\ E_2 \\ F_2 \\ A_3 \end{pmatrix} = \begin{pmatrix} \hat{\sigma}_{rr}^P(R_1)|_2 \\ \hat{\sigma}_{r\theta}^P(R_1)|_2 \\ \hat{\sigma}_{rz}^P(R_1)|_2 \\ -\hat{u}_r^P(R_2)|_2 \\ -\hat{\sigma}_{rr}^P(R_2)|_2 \\ -\hat{\sigma}_{r\theta}^P(R_2)|_2 \\ -\hat{\sigma}_{rz}^P(R_2)|_2 \end{pmatrix} \quad (2.22)$$

The coefficients g_{ij} can be deduced from Eqs. (2.13-2.21). For example, the fourth row of Eq. (2.22) describes the radial displacements at $r = R_2$ with the coefficients:

$$\begin{aligned} g_{41} &= \left[dH_\nu^{(1)}(h_{r2}r)/dr \right]_{R_2} / H_\nu^{(1)}(h_{r2}R_1) \\ g_{42} &= \left[dJ_\nu(h_{r2}r)/dr \right]_{R_2} H_\nu^{(1)}(h_{r2}R_2) \\ g_{43} &= (i\nu/R_2) H_\nu^{(1)}(k_{r2}R_2) / H_\nu^{(1)}(k_{r2}R_1) \\ g_{44} &= (i\nu/R_2) J_\nu(k_{r2}R_2) H_\nu^{(1)}(k_{r2}R_2) \\ g_{45} &= (is/k_2) \left[dH_\nu^{(1)}(k_{r2}r)/dr \right]_{R_2} / H_\nu^{(1)}(k_{r2}R_1) \\ g_{46} &= (is/k_2) \left[dJ_\nu(k_{r2}r)/dr \right]_{R_2} H_\nu^{(1)}(k_{r2}R_2) \\ g_{47} &= - \left[dH_\nu^{(1)}(h_{r3}r)/dr \right]_{R_2} / H_\nu^{(1)}(h_{r3}R_2) \end{aligned}$$

I solve the global system of equations numerically by using Gaussian elimination with partial pivoting (i.e., row exchanges when necessary) [54]. This works reliably if I scale the equations to make all of the coefficients dimensionless. I divide the displacement equations by the compression wavenumber of a layer h_n , and I divide the stress equations by $\lambda_n h_n^2$. The choice of the reference layer n is not critical.

2.4 Stability in Wavenumber

The method presented in this thesis is numerically stable over a wide range of frequencies, circumferential orders, and axial wavenumbers. This numerical stability is achieved by defining the global matrix to have the following three features:

The first feature is the way the global matrix handles evanescence across layers, as introduced by Schmidt and Jensen [39]. Physically, evanescence across a layer should decouple the global system into separate subsystems, so the solution values caused by sources on one side of an evanescent layer should have vanishing influence on the solution values caused by sources on the other side of the evanescent layer. Numerically, the global matrix forces this behavior to occur automatically when the system is solved by Gaussian elimination with partial pivoting (row exchanges).

This is shown clearly with a simple example. Consider a system of concentric fluid layers, with evanescence across a thick layer n (i.e., $s \gg h_n$). Fig. 2-2 shows the structure of the global equations. Due to the normalization of Eq. (2.13), the coefficients

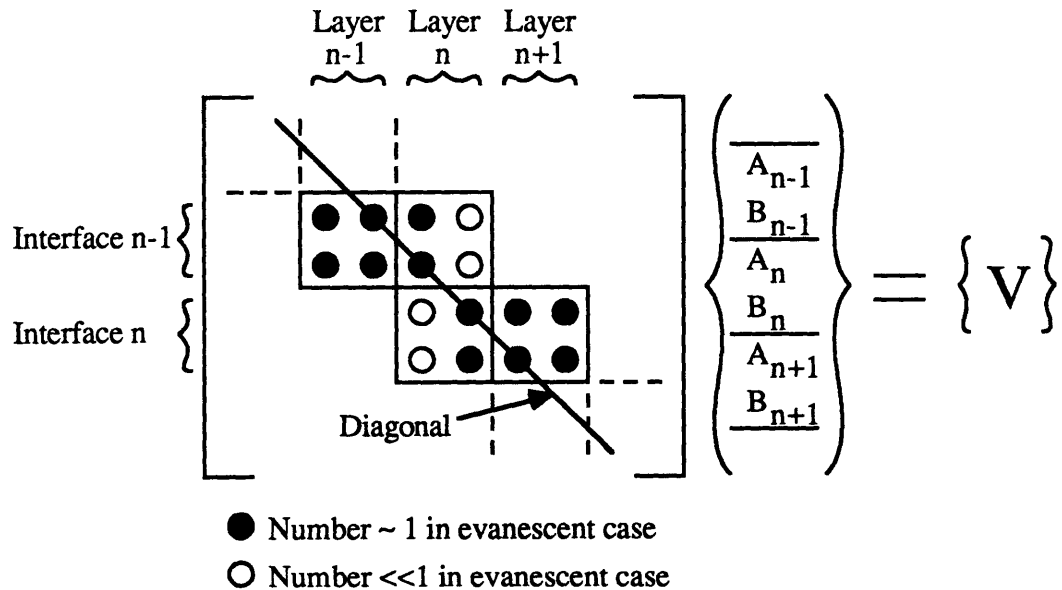


Figure 2-2: Structure of the global equations for the evanescent case.

for A_n vanish for $r = R_n$, while the coefficients for B_n vanish for $r = R_{n-1}$. Therefore, when the matrix is made triangular by Gaussian elimination, no row exchanges

will be performed between the rows for interface $n - 1$ and the rows for interface n . Effectively, the global matrix partitions itself, and the vanishing coefficients suppress the propagation of any numerical roundoff errors across the partitioning during back-substitution.

The second feature is the use of $H_\nu^{(1)}(x)$ and $J_\nu(x)$ in Eqs. (2.13-2.15). Consider that I need a pair of linearly independent wave functions to represent the unknown homogeneous solution across a layer. Mathematically, the linear independence prevents matrix singularity, and physically, the linear independence corresponds to the fact that both the amplitude and phase of the homogeneous waves are unknown. In theory, I could choose any pair of the functions $J_\nu(x)$, $Y_\nu(x)$, $H_\nu^{(1)}(x)$, and $H_\nu^{(2)}(x)$. However, for $\text{Im}\{x\} \gg 1$,

$$\begin{aligned} H_\nu^{(1)}(x) &\sim \sqrt{2/(\pi x)} e^{i(x-\nu\pi/2-\pi/4)} \\ H_\nu^{(2)}(x) &\sim 2J_\nu(x) \sim -2iY_\nu(x) \sim \sqrt{2/(\pi x)} e^{-i(x-\nu\pi/2-\pi/4)} \end{aligned}$$

Thus, for $\text{Im}\{x\} \gg 1$, the distinction between $H_\nu^{(2)}(x)$, $J_\nu(x)$, and $Y_\nu(x)$ is lost on a computer with finite precision. Also, for $|\nu| \gg |x|$,

$$\begin{aligned} J_\nu(x) &\sim (x/2)^\nu / \Gamma(\nu + 1) \\ Y_\nu(x) &\sim -iH_\nu^{(1)}(x) \sim iH_\nu^{(2)}(x) \sim -(1/\pi)\Gamma(\nu)(x/2)^{-\nu} \end{aligned}$$

for $\text{Re}\{\nu\} > 0$ with ν held fixed and $x \rightarrow 0$. Thus, for $|\nu| \gg |x|$, the distinction between $Y_\nu(x)$, $H_\nu^{(1)}(x)$, and $H_\nu^{(2)}(x)$ is lost on a computer with finite precision. To preserve linear independence numerically, the only pair of these four functions that can work for both $\text{Im}\{x\} \gg 1$ and $|\nu| \gg |x|$ is $H_\nu^{(1)}(x)$ and $J_\nu(x)$.

The third feature is the normalization of $H_\nu^{(1)}(x)$ and $J_\nu(x)$ in Eqs. (2.13-2.15) with Hankel functions of the first kind. These “normalizing” Hankel functions elegantly do two things:

1. For $|\nu| \gg |x|$, they cancel the overflow of $H_\nu^{(1)}(x)$ and the underflow of $J_\nu(x)$.

2. For $\text{Im}\{x\} \gg 1$, they implement the decoupling described above that maintains numerical stability when there is evanescence across layers.

Note that the normalizing Hankel functions are available at no computational expense, because they must be computed anyway to express the homogeneous waves at the interfaces. I have simply re-arranged the wave functions in a way that gives numerical stability.

Now, to compute the coefficients of the global matrix, I use a double precision software package for Bessel functions of complex arguments and non-negative real orders [55] [56]. The software package has an option for exponential scaling that avoids overflow and underflow for $\text{Im}\{x\} \gg 1$. I add our own code to compute $H_\nu^{(1)}(x)$ and $J_\nu(x)$ normalized to avoid overflow and underflow for $|\nu| \gg |x|$. To do this, I define the functions:

$$H_\nu^*(x) \equiv \frac{(x/2)^\nu}{\Gamma(\nu)} H_\nu^{(1)}(x) \quad J_\nu^*(x) \equiv \frac{\Gamma(\nu)}{(x/2)^\nu} J_\nu(x)$$

This normalization gives $H_\nu^*(x)$ an elegant formula for upward recurrence:

$$H_{\nu+1}^*(x) = H_\nu^*(x) - \frac{(x/2)^2}{\nu^2 - \nu} H_{\nu-1}^*(x)$$

Thus, to compute $H_\nu^*(x)$ for large orders, I compute $H_\nu^*(x)$ for low orders, then I use the upward recurrence relation. Upward recurrence is stable, because the $J_\nu(x)$ component of $H_\nu^*(x)$ underflows, while the $Y_\nu(x)$ component is stable. And, I compute $J_\nu^*(x)$ with a series:

$$J_\nu^*(x) = \sum_{j=0}^{\infty} q_j$$

where the terms are:

$$q_j = \begin{cases} 1/\nu & j = 0 \\ -\frac{x^2/4}{j(\nu+j)} q_{j-1} & 1 \leq j < \infty \end{cases}$$

To see how these functions are used, consider the coefficient g_{43} for the fluid-loaded

shell. I evaluate g_{43} using one of the following formulas:

$$g_{43} = \begin{cases} (i\nu/R_2) \left[\frac{H_\nu^{(1)}(k_{r2}R_2)}{e^{ik_{r2}R_2}} \right] \left(\frac{e^{ik_{r2}R_2}}{e^{ik_{r2}R_1}} \right) / \left[\frac{H_\nu^{(1)}(k_{r2}R_1)}{e^{ik_{r2}R_1}} \right] & |(k_{r2}R_1/2)^\nu/\Gamma(\nu)| \geq 0.01 \\ (i\nu/R_2) [H_\nu^*(k_{r2}R_2)] (R_1/R_2)^\nu / [H_\nu^*(k_{r2}R_1)] & |(k_{r2}R_1/2)^\nu/\Gamma(\nu)| < 0.01 \end{cases}$$

By default, I use the first formula using exponential normalization. I choose the other formula according to the criterion shown. This criterion estimates whether $J_\nu(x)$ is small relative to $H_\nu^{(1)}(x)$.

2.5 Transforming to Space

The procedures described above compute numerically stable solutions at discrete points in the axial wavenumber plane. To transform solutions to the spatial domain, I consider solutions at several points in the s -plane and compute a numerical approximation of the wavenumber integral in Eq. (2.6).

In this thesis, I integrate using the trapezoidal rule, which linearly interpolates the integrand $\hat{f}(r, s)e^{isz}$ between samples. The contour of integration used here is:

$$s = \ell\Delta s - i\epsilon(2/\pi) \tan^{-1}(\ell\Delta s/s_c) \quad (2.23)$$

where Δs is real, ℓ has integer values, ϵ is the contour offset for large values of $\ell\Delta s/s_c$, and s_c specifies how fast the contour approaches ϵ .

The interval of integration is truncated by choosing a real number s_L such that most of the content of the integrand is accounted for within $-s_L < s < s_L$. Then, I compute $\Delta s = s_L/M$, where L is a large positive integer, and I integrate over $-L < \ell < L$. I increase L to decrease Δs , and I observe the convergence of the solution. L is typically 500 or larger.

The contour offset must be non-zero because poles may appear on the real s -axis when the frequency is real, as shown in Fig. 3. This issue is best understood in terms

of spatial wrap-around. For ring forces at $z = 0$, spacing the samples by Δs on the real s -axis would give wrap-around from virtual ring forces spaced at multiples of $2\pi/\Delta s$ in z . Decreasing Δs would move the virtual ring forces farther apart, but the poles on the real axis correspond to trapped waves that travel without decay, so these waves would still cause wrap-around. It can be shown that contour offset suppresses wrap-around by re-formulating the transform into a synthesis of waves that decay exponentially from all the ring forces (actual and virtual), and the results of that synthesis are effectively multiplied by growing exponentials to give solutions that are accurate on the interval $-\pi/\Delta s < z < \pi/\Delta s$. Contour offset suppresses the wrapped-around waves by $20 \log_{10} e^{\epsilon\pi/\Delta s}$ dB relative to the correct solution at $z = \pm\pi/\Delta s$. Using this formula, I choose to get 60 dB of suppression at $z = \pm\pi/\Delta s$ by setting:

$$\epsilon = 2.2\Delta s \quad (2.24)$$

The relationship between wrap-around and contour offset is discussed further by Jensen et al [41] and considered in greater detail here in Appendix B.

But, while contour offset suppresses wrap-around, it can also make the transform unstable. This issue is best understood by examining Eq. (2.6) directly. The instability for positive z comes from the part of the contour where $\text{Im}\{s\} < 0$, which causes e^{isz} to grow with z . If the numerical integration were exact, these growing exponentials would interfere to give the exact solution, by Cauchy's integral theorem. But, because the interpolation of the integrand introduces errors, there may be noticeable growth if the contour offset is too large. In practice, Eq. (2.24) minimizes the contour offset so the numerical transform remains stable, in the sense that trapped waves do not grow with distance from the actual ring forces.

For future reference, our experience shows that computing the samples in the s -plane typically takes much more computing time than the integration. Therefore, numerical efficiency can be increased by using the samples in more effective ways. For example, the sample spacing can be varied adaptively to interpolate $\hat{f}(r, s)$ better where it varies faster, chiefly around its poles. Also, Filon integration can increase

accuracy without increasing computation time significantly, because it interpolates the kernel $\hat{f}(r, s)$ and accounts for e^{isz} exactly using integration by parts [38]. Filon integration is especially efficient when z is large, because it accurately accounts for e^{isz} oscillating rapidly with s . Seen in this light, the FFT implementation of Eq. (2.6) may be relatively inefficient (unless the solution is sought at many axial locations), because the FFT requires constant sample spacing, and it effectively substitutes constant rectangular functions for the integrand.

Finally, I discuss the symmetry of the fields involved, so I can efficiently include the contributions for $\text{Re}\{s\} > 0$ and $\text{Re}\{s\} < 0$. For radial and circumferential ring forcing, the quantities \hat{u}_r , \hat{u}_θ , $\hat{\sigma}_{rr}$, and $\hat{\sigma}_{r\theta}$ are symmetric with respect to $s = 0$, while \hat{u}_z and $\hat{\sigma}_{rz}$ are antisymmetric. For axial ring forcing, the quantities \hat{u}_z and $\hat{\sigma}_{rz}$ are symmetric, while \hat{u}_r , \hat{u}_θ , $\hat{\sigma}_{rr}$, and $\hat{\sigma}_{r\theta}$ are antisymmetric. These symmetry properties can be confirmed by examining the particular solutions shown in Appendix A.

2.6 Computing Input Power

This section shows how I compute the time-averaged power $\langle \Pi \rangle$ injected into a shell by a time-harmonic point force that pushes in the radial direction. Other directions can be considered by changing the subscripts from r to θ or z .

To begin, I define a radial point force located at $\{r, \theta, z\} = \{r', 0, 0\}$ to be:

$$\mathbf{f}(r, \theta, z, t) = \mathbf{a}_r F_o \frac{\delta(r - r')\delta(\theta)\delta(z)}{r'} e^{-i\omega t} \quad (2.25)$$

where F_o is the magnitude of the force. The angular dependence $\delta(\theta)$ can be considered as a sum of integer orders m or an integral of continuous orders ν :

$$\delta(\theta) = \frac{1}{2\pi} \sum_{m=-\infty}^{\infty} e^{im\theta} = \frac{1}{2\pi} \int_{-\infty}^{\infty} e^{i\nu\theta} d\nu \quad (2.26)$$

To decide which description is better, consider that the goal here is to form a synthesis

that converges well on the response of the shell, rather than converging on the function $\delta(\theta)$ itself. Therefore, our decision is guided by the physics of the shell, rather than anything we might see in Eq. (2.26) by itself. In the next chapter, I will show that the power injected into the shell by a radial point force is controlled by integer order flexural waves (assuming the frequency ω is real, and assuming the excitation is in the so-called mid-frequency range of perhaps one or two decades of frequency around the ring frequency of a thin shell with heavy fluid loading). Therefore, I substitute the integer order description of Eq. (2.26) into Eq. (2.25), which gives:

$$\mathbf{f}(r, \theta, z, t) = \frac{F_o}{2\pi r'} \sum_{m=-\infty}^{\infty} \mathbf{a}_r \delta(r - r') e^{im\theta} \delta(z) e^{-i\omega t} \quad (2.27)$$

Note that each term in Eq. (2.27) is a radial ring force of the form considered in Appendix A, with the order set equal to integer values m , and the amplitude F_r set equal to one Newton per meter. Noting this, I wrote computer code to compute $\hat{u}_r(r', 0, s)$, which is the radial displacement at the coordinates $r = r'$ and $\theta = 0$, observed in the wavenumber domain. I compute $\hat{u}_r(r', 0, s)$ by holding s constant and summing the response to ring forces over the integer orders m . This increases computational efficiency by taking advantage of the recurrence relations for Bessel functions.

Given this code for computing $\hat{u}_r(r', 0, s)$, I tried to compute the drive point displacement $u_r(r', 0, 0)$ by computing the Fourier integral:

$$u_r(r', 0, z) = \int_{-\infty}^{\infty} \hat{u}_r(r', 0, s) e^{isz} ds$$

with $z = 0$. However, I found that this integral did not converge. The reason is that the real part of the drive point displacement $\text{Re}\{u_r(r', 0, 0)\}$ goes to infinity whenever Dirac deltas are used to excite the 3D equations of elastodynamics with point forces, line forces, or ring forces. This artifact appears in the wavenumber domain as $\hat{u}_r(r', 0, s) \propto 1/s$ for large s . Thus, infinity is the correct answer! I discuss this artifact more in Chapter 3 and Appendix C.

However, the time-averaged input power $\langle \Pi \rangle$ is finite, and it is related to the imaginary part of the drive point displacement $\text{Im}\{u_r(r', 0, 0)\}$, which is also finite:

$$\langle \Pi \rangle = (1/2)F_o\omega\text{Im}\{u_r(r', 0, 0)\} \quad (2.28)$$

I compute the imaginary part of the drive point displacement $\text{Im}\{u_r(r', 0, 0)\}$ as:

$$\text{Im}\{u_r(r', 0, 0)\} = 2 \int_0^\infty [\text{Im}\{\hat{u}_r(r', 0, s)\} \cos \alpha - \text{Re}\{\hat{u}_r(r', 0, s)\} \sin \alpha] dS \quad (2.29)$$

where $S \equiv |s|$ is the variable of integration, and α is the angle of the path of integration below the real s -axis, shown in Fig. 2-3. Typically, I let α be 30 degrees. This large offset works for $z = 0$ because $e^{isz} = 1$, so the integral over wavenumber does not involve growing exponentials. This path of integration speeds up convergence, because it avoids passing close to the poles, so the integrand is smoother. I use Romberg integration [57], which is adaptive, so it automatically decreases the sample spacing until a convergence criterion is satisfied.

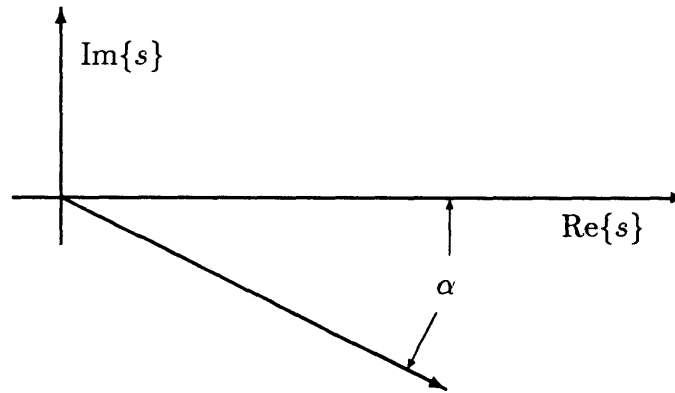


Figure 2-3: Path of integration for input power

This page is blank.

Chapter 3

Comparison to Thin Shell Models

In this chapter, I consider a thin elastic shell that is infinitely long with external fluid loading. The shell is modeled with the DGM shell model and a thin shell theory. In general, good agreement is found between the two models, and this verifies the DGM shell model. Some cases of disagreement are also found, and this illustrates the limitations of the thin shell theory.

The shell in this chapter is steel, with a mean radius of $R_s = 2.5$ m and a thickness of $T_s = 0.05$ m. The external fluid is water. To model this with the DGM shell model, I let the number of layers N be 3, where layer 1 is a vacuum, layer 2 is steel, and layer 3 is water. I let the outer radius of the vacuum be $R_1 = 2.475$ m, and the outer radius of the steel be $R_2 = 2.525$ m. For the steel, I let the density be $\rho_2 = 7800$ kg/m³, the speed of compression waves be $c_{c2} = 5900$ m/s, and the speed of shear waves be $c_{s2} = 3160$ m/s. For the water, I let the density be $\rho_3 = 1000$ kg/m³ and the speed of compression waves be $c_{c3} = 1465$ m/s. Given these parameters, the Lamé constants can be found from the wave speeds as $\mu_2 = \rho_2 c_{s2}^2 \doteq 77.9 \times 10^9$ kg/m/s² and $\lambda_2 = \rho_2 c_{c2}^2 - 2\mu_2 \doteq 116 \times 10^9$ kg/m/s² and $\lambda_3 = \rho_3 c_{c3}^2 \doteq 2.15 \times 10^9$ kg/m/s².

To describe the dynamics of the shell in some context, I compute some other parameters of interest:

- Let E_s and ν_s be Young's modulus and the Poisson ratio of the shell, respectively. These can be computed from the Lamé constants by using formulas presented by Kolsky [42]. Thus, I have $E_s = \mu_2(3\lambda_2 + 2\mu_2)/(\lambda_2 + \mu_2) \doteq 202 \times 10^9$ kg/m/s² and $\nu_s = \lambda_2/[2(\lambda_2 + \mu_2)] \doteq 0.299$.
- Let $c_{L_s} = \sqrt{E_s/[\rho_s(1 - \nu_s^2)]} \doteq 5337$ m/s. This parameter can be interpreted as the speed of longitudinal waves in an elastic plate made of the same material as the shell, in the limit that the waves are long compared to the thickness. The derivation of this formula can be found in the books by Junger and Feit [1] and Kolsky [42].
- Let f_r be the ring frequency of the shell. This is defined as the resonance frequency of the breathing mode of the shell in vacuum. This is commonly computed using the formula $f_r \equiv c_{L_s}/(2\pi R_s) \doteq 340$ Hz. This formula can be derived by setting $\partial/\partial\theta$ and $\partial/\partial z$ equal to zero in the Donnell thin shell equations, which are shown in the next section of this chapter. In radians per second, the ring frequency is $\omega_r \equiv c_{L_s}/R_s \doteq 2137$ rad/sec.
- Let f_c be the coincidence frequency, which is defined as the frequency where the speed of sound in the fluid equals the speed of flexural waves in the classical theory of bending of a flat plate in a vacuum. From Junger and Feit [1], this is given as $f_c = \sqrt{12} c^2/(2\pi T c_L)$, where c is the speed of sound in the fluid, T is the thickness of the plate, and c_L is the speed of longitudinal waves in the plate. Applying this formula to the fluid-loaded shell, we have $f_c = \sqrt{12} c_3^2/(2\pi T_s c_{L_s}) \doteq 4434$ Hz.

3.1 Thin Shell Theories

Thin shell theories are much simpler than the full 3D equations of elastodynamics, because they represent all displacements, forces, and moments as 2D fields observed on the middle surface of the shell. However, a suprisingly large number of thin shell theories have been derived for a cylindrical shell. Several different theories are presented and compared in books by Leissa [27] and Markuš [29]. Additional discussions of derivations are presented in books by Junger and Feit [1] and Cremer and Heckl [28]. Also, some new thin-shell theories have been recently introduced in papers by and Scott [58] and Borgiotti and Rosen [59].

As an introduction to the subject, I started with the Donnell equations, because the Donnell equations are perhaps the simplest thin shell equations to include both membrane waves and flexural waves. The terms accounting for the membrane effects are widely accepted, while the terms accounting for the flexural effects are written simply in terms of a biharmonic operator (as they are in the classical theory of flat plate bending). In this chapter, I present the Donnell equations for a thin cylindrical shell, as they are found in Junger and Feit [1]. Here I correct a sign error that appears in that book, I apply ring forces, and I set up the solution in terms of a wavenumber transform.

To write the Donnell equations here, we consider a shell with mean radius R_s , thickness T_s , Young's modulus E_s , Poisson's ratio ν_s , and density ρ_s . The fluid outside the shell has density ρ , wave speed c , and wavenumber $h = \omega/c$. The displacements of the shell's middle surface are $U_r(\theta, z)$, $U_\theta(\theta, z)$, and $U_z(\theta, z)$, measured in the radial, circumferential, and axial directions, respectively.

To write the equations neatly, let $\epsilon_s = T_s^2/(12R_s^2)$, and let $c_{Ls} = \sqrt{E_s/[\rho_s(1 - \nu_s^2)]}$, which can be interpreted as the speed of longitudinal waves in an elastic plate [1] [42]. Also, I define the biharmonic operator for the shell displacements to be:

$$\nabla_s^4 \equiv \frac{1}{R_s^4} \frac{\partial^4}{\partial \theta^4} + \frac{2}{R_s^2} \frac{\partial^4}{\partial \theta^2 \partial z^2} + \frac{\partial^4}{\partial z^4}$$

To excite this model, I let S_{rr} , $S_{r\theta}$, and S_{rz} be stress distributions applied to the surface of the shell. These stresses act on the shell in the r , θ , and z directions, respectively, and have units of force per area. I add these stresses into the thin-shell equations so they add correctly to the accelerations of an infinitesimal element, and the Donnell equations become:

$$\begin{aligned} -\frac{U_r}{R_s^2} - \epsilon_s R_s^2 \nabla_s^4 U_r - \frac{1}{R_s^2} \frac{\partial U_\theta}{\partial \theta} - \frac{\vartheta_s}{R_s} \frac{\partial U_z}{\partial z} + \frac{S_{rr} - p_{R_s}}{\rho_s c_{L_s}^2 T_s} &= \frac{\ddot{U}_r}{c_{L_s}^2} \\ + \frac{1}{R_s^2} \frac{\partial U_r}{\partial \theta} + \frac{1}{R_s^2} \frac{\partial^2 U_\theta}{\partial \theta^2} + \frac{1 - \vartheta_s}{2} \frac{\partial^2 U_\theta}{\partial z^2} + \frac{1 + \vartheta_s}{2 R_s} \frac{\partial^2 U_z}{\partial \theta \partial z} + \frac{S_{r\theta}}{\rho_s c_{L_s}^2 T_s} &= \frac{\ddot{U}_\theta}{c_{L_s}^2} \\ \frac{\vartheta_s}{R_s} \frac{\partial U_r}{\partial z} + \frac{1 + \vartheta_s}{2 R_s} \frac{\partial^2 U_\theta}{\partial \theta \partial z} + \frac{1 - \vartheta_s}{2 R_s^2} \frac{\partial^2 U_z}{\partial \theta^2} + \frac{\partial^2 U_z}{\partial z^2} + \frac{S_{rz}}{\rho_s c_{L_s}^2 T_s} &= \frac{\ddot{U}_z}{c_{L_s}^2} \end{aligned}$$

where p_{R_s} is the pressure of an external fluid, evaluated at the radius R_s .

To check this system of equations, multiply both sides of each equation above by $\rho_s c_{L_s}^2 T_s$ times an infinitesimal element of surface area, so the right-hand sides of the equations are the accelerations times the element's mass, and the left-hand sides involve the applied stresses times the element's area with the correct signs. This corrects the sign error on the fluid pressure found in Junger and Feit [1].

To introduce ring forces, I give all sources and fields a time dependence of $e^{-i\omega t}$, and an angular dependence of $e^{i\nu\theta}$. These factors will be implied from here on. To represent a ring force acting in the radial direction, let the stress distributions be $\{S_{rr}, S_{r\theta}, S_{rz}\} = \{F_r \delta(z), 0, 0\}$, where $\delta(z)$ is a Dirac delta, and F_r has units of force per length. Integrating this stress distribution over z , we see that this represents a ring force, where F_r is the force per length around the ring. Similarly, to represent a ring force acting in the circumferential direction, let the stress distributions be $\{S_{rr}, S_{r\theta}, S_{rz}\} = \{0, F_\theta \delta(z), 0\}$, where F_θ is the force per length around the ring. For $\nu = 0$, this produces a net torque about the axis of $2\pi R_s^2 F_\theta$. And, I represent an axial ring force as $\{S_{rr}, S_{r\theta}, S_{rz}\} = \{0, 0, F_z \delta(z)\}$, where F_z is again the force per length around the ring. For $\nu = 0$, this produces a net force in the axial direction of $2\pi R_s F_z$.

To set up solutions, I define the wavenumber transforms of the displacements and excitations with Fourier transform pairs of the form:

$$f(z) = \int_{-\infty}^{\infty} \hat{f}(s)e^{isz} ds \quad \hat{f}(s) = \frac{1}{2\pi} \int_{-\infty}^{\infty} f(z)e^{-isz} dz$$

where $f(z)$ is any field being transformed, and the hat ($\hat{\cdot}$) denotes the wavenumber transform of a quantity. Also, considering the implied angular dependence of $e^{i\nu\theta}$, the transform of the biharmonic operator is:

$$\hat{\nabla}_s^4 \equiv \frac{\nu^4}{R_s^4} + 2\frac{\nu^2 s^2}{R_s^2} + s^4$$

From this, the Donnell equations lead to:

$$\begin{bmatrix} \frac{1}{R_s^2} + \epsilon_s R_s^2 \hat{\nabla}_s^4 - \frac{\omega^2}{c_{L_s}^2} & i\nu/R_s^2 & is\vartheta_s/R_s & (\rho_s c_{L_s}^2 T_s)^{-1} \\ -i\nu/R_s^2 & \frac{\nu^2}{R_s^2} + \frac{1-\vartheta_s}{2}s^2 - \frac{\omega^2}{c_{L_s}^2} & \frac{1+\vartheta_s}{2R_s}\nu s & 0 \\ -is\vartheta_s/R_s & \frac{1+\vartheta_s}{2R_s}\nu s & \frac{1-\vartheta_s}{2R_s^2}\nu^2 + s^2 - \frac{\omega^2}{c_{L_s}^2} & 0 \\ -\rho\omega^2 & 0 & 0 & \frac{(dH_\nu^{(1)}(h_r r)/dr)_{r=R_s}}{H_\nu^{(1)}(h_r R_s)} \end{bmatrix} \begin{bmatrix} \hat{U}_r \\ \hat{U}_\theta \\ \hat{U}_z \\ \hat{p}_{R_s} \end{bmatrix} = \frac{1}{2\pi\rho_s c_{L_s}^2 T_s} \begin{bmatrix} F_r \\ F_\theta \\ F_z \\ 0 \end{bmatrix} \quad (3.1)$$

where \hat{p}_{R_s} is the transform of the fluid pressure at $r = R_s$, ρ is the density of the external fluid, and h_r is the radial wavenumber in the fluid, such that $h_r^2 = h^2 - s^2$. Note that the fourth equation in the above system states that the radial accelerations of the shell and fluid must be equal. This equation is derived from the momentum equation, considering that the transform of the fluid pressure has the form:

$$\hat{p}(r, \nu, s) = \hat{p}_{R_s}(\nu, s) \frac{H_\nu^{(1)}(h_r r)}{H_\nu^{(1)}(h_r R_s)}$$

3.2 Agreement

This section shows the general agreement between the DGM shell model and the Donnell thin shell model. This agreement verifies the DGM shell model.

3.2.1 Agreement in Wavenumber

This subsection shows the shell's response to different excitations in the wavenumber domain. The response is presented as contour plots of the magnitude of the response variable (e.g., pressure or displacement). I computed each contour plot in wavenumber by sampling the solution in a grid of 100 by 100 points in the wavenumber domain. These contour plots have been very useful, for several reasons:

- First, they clearly show the poles in the complex axial wavenumber domain, and these poles identify the various wave types for a given frequency and circumferential order. The wave types are typically flexural, membrane compression, and membrane shear.
- Second, they help us understand the subject of Riemann sheets and branch cuts. My programs offer the user a choice between EJP and Pekeris branch cuts. This subject is discussed more in Appendix D.
- Third, these contour plots have been very useful for debugging the computer code for the DGM shell model. If the code is correct, then the contour plots should show functions that are analytic everywhere except for the poles and the branch cuts. Furthermore, the only branch cuts that should appear are the branch cuts associated with the outermost layer radiating to infinity (as discussed more in Appendix D). Therefore, considering that all of the samples in the 100 by 100 grid are computed independently of each other, some types of programming errors will be immediately apparent in the contour plots, as the contour plots may not look analytic, or additional branch may cuts appear.

Figure 3-1 shows that the models agree when the shell is excited by a ring force pushing in the radial direction with $\omega = 5\omega_r$ and $\nu = 0$. The radius of the ring force is $r' = 2.5$ m, and its amplitude is 1 Newton per meter of length around the ring. The figure shows the fluid pressure at the shell's surface, plotted in dB in the wavenumber domain as $20 \log_{10}(|\hat{\sigma}_{rr}|/1\mu\text{Pa}/1\text{m})$. The notable features are: 1) The two poles on the real s -axis, which correspond to flexural waves that travel in the axial direction away from the ring force. These are “trapped waves” in the sense that they travel without losing energy to the fluid. 2) The poles near the imaginary s -axis, which correspond to flexural waves that decay exponentially in the axial direction away from the ring force. 3) The branch points and branch cuts associated with the outermost fluid layer. 4) Also, there are poles at $s \approx \pm 2.00 \text{ m}^{-1}$ that correspond to membrane compression waves in the shell. However, these poles do not appear clearly in this plot, because they are weakly excited compared to the flexural waves at this receiver radius. In this particular plot, the membrane compression poles barely appear as the kinks in the contour lines at $s \approx \pm 2.00 \text{ m}^{-1}$.

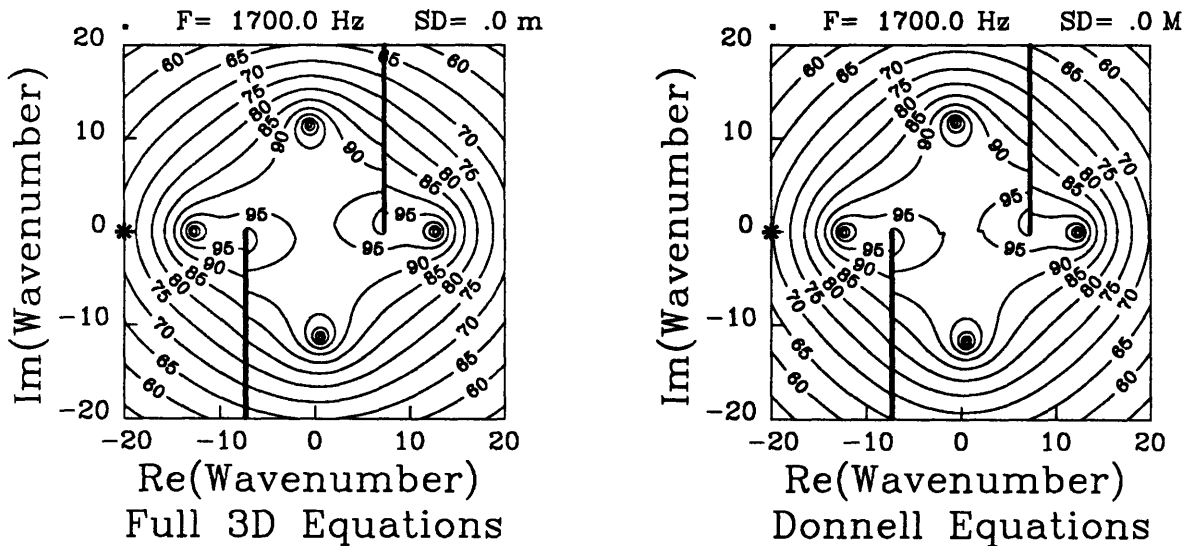


Figure 3-1: Fluid pressure at the shell surface for radial ring forcing with $\omega = 5\omega_r$ and $\nu = 0$, plotted as $20 \log_{10}(|\hat{\sigma}_{rr}|/1\mu\text{Pa}/1\text{m})$. Pekeris branch cuts are chosen. Wavenumber axes are shown in m^{-1} .

As a more complicated example, Fig. 3-2 shows that the models agree when the shell is excited by a ring force pushing in the circumferential direction with $\omega = 5\omega_r$ and $\nu = 5$. The radius of the ring force is $r' = 2.5$ m, its amplitude is 1 N/m, and the response is plotted as $20 \log_{10}(|\hat{\sigma}_{rr}|/1\mu\text{Pa}/1\text{m})$. Compared to Fig. 3-1, the notable features are: 1) A different scale has been used for the axes, so the poles for the membrane waves appear clearly. The branch cuts and the flexural poles lie outside of this figure. 2) The poles for the membrane compression waves appear at the center of the figure. The poles lie closer to the imaginary axis than the real axis, because as we hold frequency constant and increase the order, this mode is making a transition from being propagating to non-propagating. 3) The poles for the membrane shear waves appear at $s \approx \pm 2.7 \text{ m}^{-1}$. These poles appear because they are strongly excited by circumferential ring forcing, and the couple to the fluid for non-zero orders. 4) Zeros appear between the poles for the compression and shear waves. These are due to interference between all of the wave types.

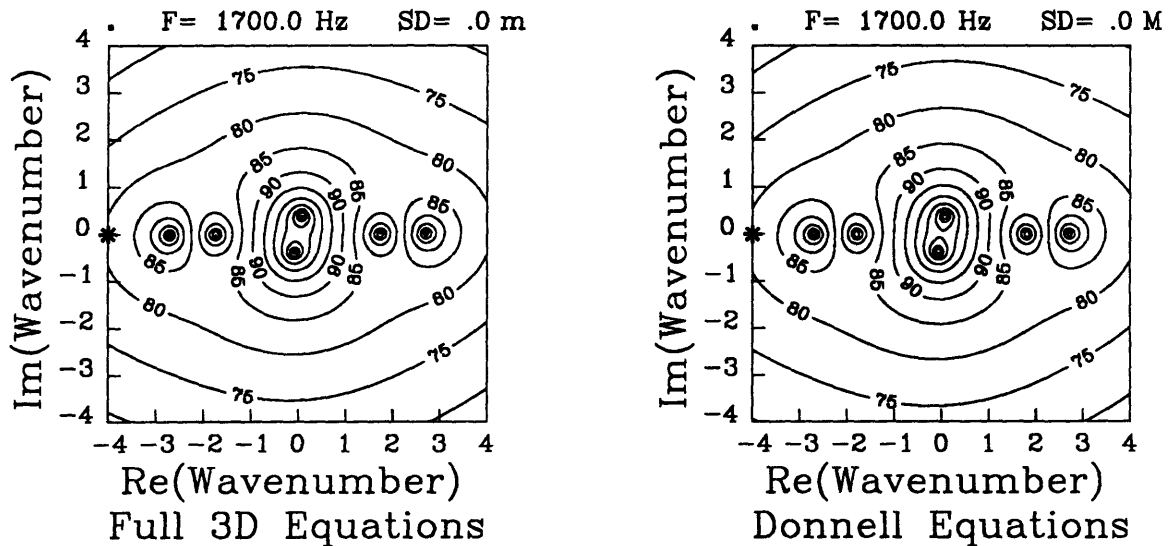


Figure 3-2: Fluid pressure at the shell surface for circumferential ring forcing with $\omega = 5\omega_r$ and $\nu = 5$, plotted as $20 \log_{10}(|\hat{\sigma}_{rr}|/1\mu\text{Pa}/1\text{m})$. Pekeris branch cuts are chosen. Wavenumber axes are shown in m^{-1} .

Figure 3-3 shows the response of the models to the same excitation as Fig. 3-2, except that the order here is $\nu = 5.5$. The models agree. This figure shows our ability to compute the response for non-integer orders, which have the physical significance described by Pierce [47] and Felsen [48] [49] [50]. We see that as we vary the order continuously, the poles move continuously. We expect this, because all the fields involved in the global matrix formulation are analytic functions of ν . Thus, we can classify poles by identifying their locations in the s -plane for $\nu = 0$ and then tracking them across the s -plane as ν increases.

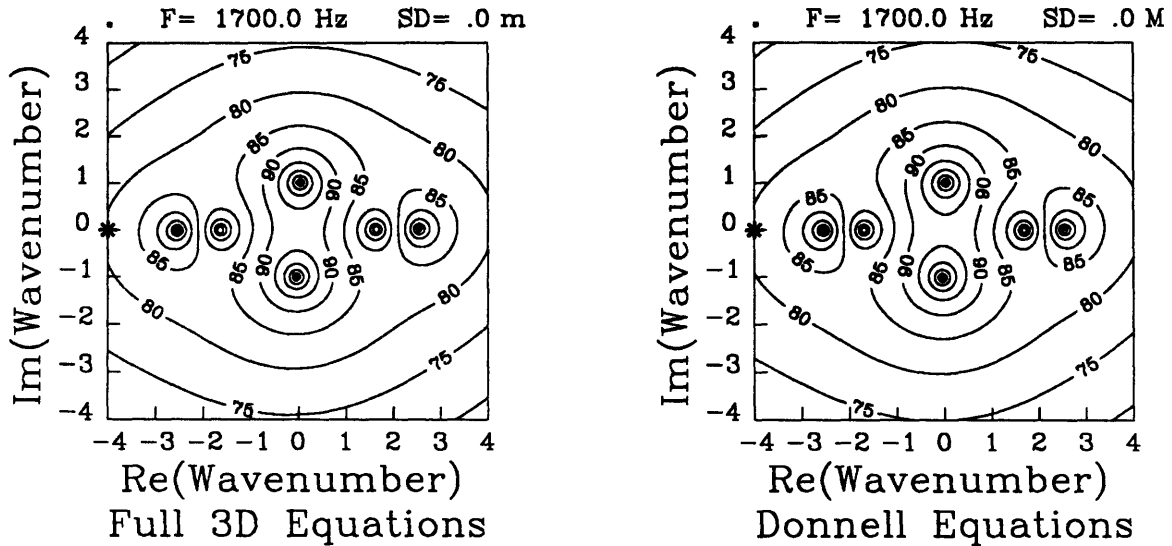


Figure 3-3: Fluid pressure at the shell surface for circumferential ring forcing with $\omega = 5\omega_r$ and $\nu = 5.5$, plotted as $20 \log_{10}(|\hat{\sigma}_{rr}|/1\mu\text{Pa}/1\text{m})$. Pekeris branch cuts are chosen. Wavenumber axes are shown in m^{-1} .

Figure 3-4 shows that the models agree when the shell is excited by a 1 N point force pushing in the radial direction with $\omega = 5\omega_r$. The force is located at $\{r, \theta, z\} = \{r', 0, 0\}$. The figure shows the radial displacement of the shell in the wavenumber domain, plotted as $20 \log_{10}(|\hat{u}_r(r', 0, s)|/1\text{m}^2)$, evaluated at $r' = 2.5$ m where the force is applied. This figure was computed by a summation over integer orders m . Thus, any poles for a given order m also appear in the plot for the summation over all orders.

This figure is dominated by the poles from the flexural waves. At this frequency, flexural waves can propagate along the length of the shell for $-32 \leq m \leq 32$. Flexural waves for $|m| > 32$ are cut off. The flexural poles for low orders are clustered together, creating the large teardrop shaped features around $s \approx \pm 13 \text{ m}^{-1}$. This figure was computed by including the orders $-200 \leq m \leq 200$, although the figure is essentially complete for $-50 \leq m \leq 50$, because the higher orders give poles that are off the figure near the imaginary axis.

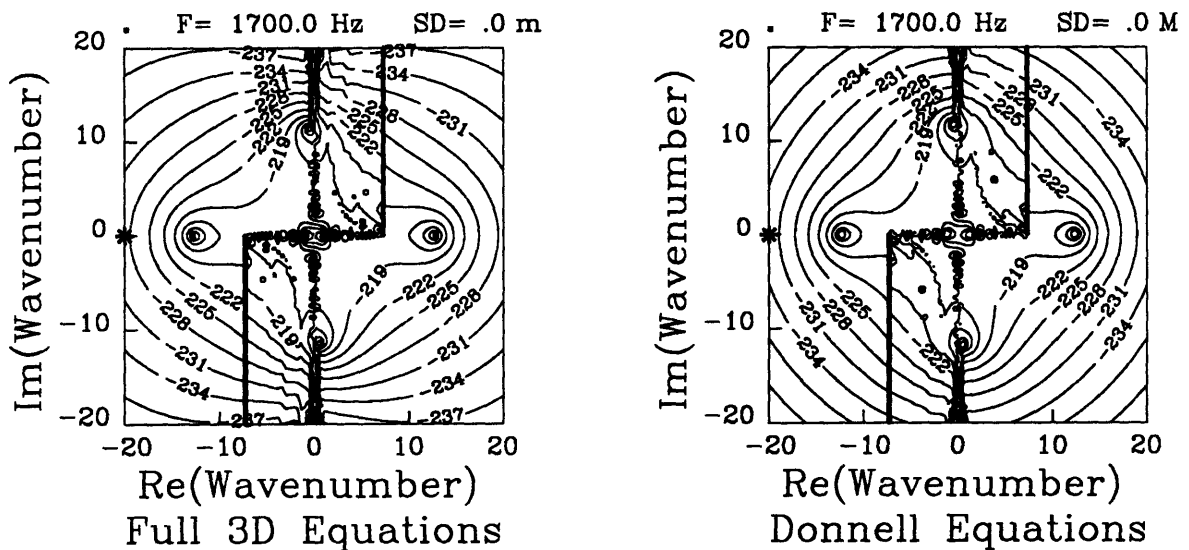


Figure 3-4: Radial displacement due to a point force pushing in the radial direction at $\{r, \theta, z\} = \{r', 0, 0\}$ with $\omega = 5\omega_r$, observed in the wavenumber domain. Pekeris branch cuts are chosen. Wavenumber axes are shown in m^{-1} .

As an incidental note, for future reference, I have considered that Fig. 3-4 could also have been generated by using an integral over continuous orders $-\infty < \nu < \infty$ and a summation over image sources in the extended angular domain $-\infty < \theta < \infty$. This would involve the concepts introduced by Pierce [47] and Felsen [48] [49] [50]. The poles in Fig. 3-4 would then arise as the summation over image sources would blow up for those axial wavenumbers s that cause oblique plane waves in the extended θ - z plane to interfere constructively.

However, Pierce and Felsen designed their method to involve integrals over axial wavenumbers s and circumferential orders ν first, to find the response to one source in an infinite θ - z plane, and this would be followed by a sum over image sources in the extended θ -domain. The contributions from the image sources would then be added together in a series that converges quickly when the solutions decay strongly in the circumferential direction. In contrast, Fig. 3-4 can be considered to be the result of a summation over image sources first, which is to be followed by an integral over wavenumber to give the response at some point in space.

As future work, a study could be made to demonstrate the advantages and disadvantages of these different approaches. I recommend such a study in Chapter 6.

3.2.2 Agreement in Space

Of course, when there is agreement in the wavenumber domain, there is agreement in the spatial domain. Figure 3-5 shows that the models agree when the shell is excited by a ring force pushing in the radial direction with $\omega = 5\omega_r$ and $\nu = 0$. The radius of the ring force is $r' = 2.5$ m, and its amplitude is 1 Newton per meter of length around the ring. Thus, this figure involves the same physical parameters as Fig. 3-1. Figure 3-5 shows the fluid pressure in the r - θ plane, plotted as $20 \log_{10} |p(r, 0, z)| / 1 \mu\text{Pa}$ for $2.5 \text{ m} \leq r \leq 20 \text{ m}$ and $0 \leq z \leq 15 \text{ m}$. Thus, the ring force is at the lower left hand corner of the figure, where $r = 2.5$ m and $z = 0$ m. The notable features are: 1) The large lobe radiating perpendicular to the axis of the shell; this is the “direct wave”

associated with the “near-field” flexural waves that decay exponentially with z away from the ring force. 2) The closely spaced contour lines running parallel to the shell’s surface; this is the evanescent acoustic field associated with the trapped flexural wave that travels along the shell without decay. 3) The “leaky wave” radiated from the membrane compression wave in the shell. It radiates at an angle of approximately $\cos^{-1}(c_{e3}/c_{Ls}) = \cos^{-1}(1465/5337) \doteq 74.1^\circ$ from the shell’s axis. This wave interferes with the trapped wave to form the sequence of zeros on the fringes of the evanescent field, and it interferes with the direct wave to give the wavy contour lines in the right side of the figure.

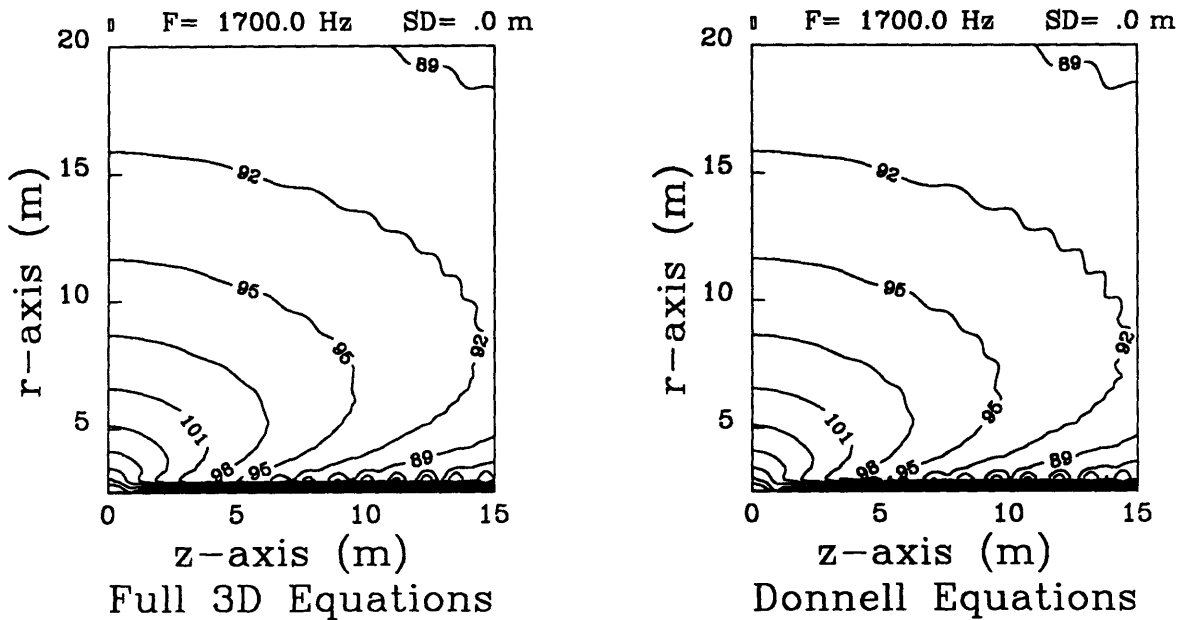


Figure 3-5: Fluid pressure due to a ring force pushing in the radial direction with $\omega = 5\omega_r$ and $\nu = 0$, observed in the spatial domain.

Figure 3-5 was computed using 40 receiver radii and 100 axial locations. Trapezoidal integration was used with constant sample spacing in wavenumber, as described in Chapter 2. Solutions were sampled at 5000 points in wavenumber over the interval $0 \leq \text{Re}\{s\} \leq 40 \text{ m}^{-1}$, and the negative wavenumbers were included by the symmetry properties described in Chapter 2. I used 5000 samples to guarantee an accurate figure for this thesis. This number is certainly larger than necessary.

3.2.3 Agreement in Power Input

Borgiotti and Rosen recently considered an infinitely long thin cylindrical shell in a vacuum, excited by a point force acting in the radial direction [59]. Their computations used a thin shell theory of their own derivation, with the algebra arranged in a state vector formulation. They computed the time-averaged power flowing down the length of the shell.

I reproduce their result below in Fig. 3-6. I can compare my results directly with theirs, because the shell I am studying in this chapter is defined to have the same dimensions and material properties as the shell they studied. Here I define $\langle \Pi \rangle$ to be the time-averaged power input, which is twice the power flow computed by Borgiotti and Rosen, because they computed the power flowing in one direction away from the force. Thus, my figure agrees perfectly with theirs, except that my power flow is exactly twice theirs. Also, I sampled the response at 1000 points along the frequency axis, so my figure makes smoother curves with sharper peaks than theirs. The results are shown for increasing the number of integer orders included in the series of ring forces. The agreement shown here confirms both their theory and mine (over the range of frequency and orders shown here).

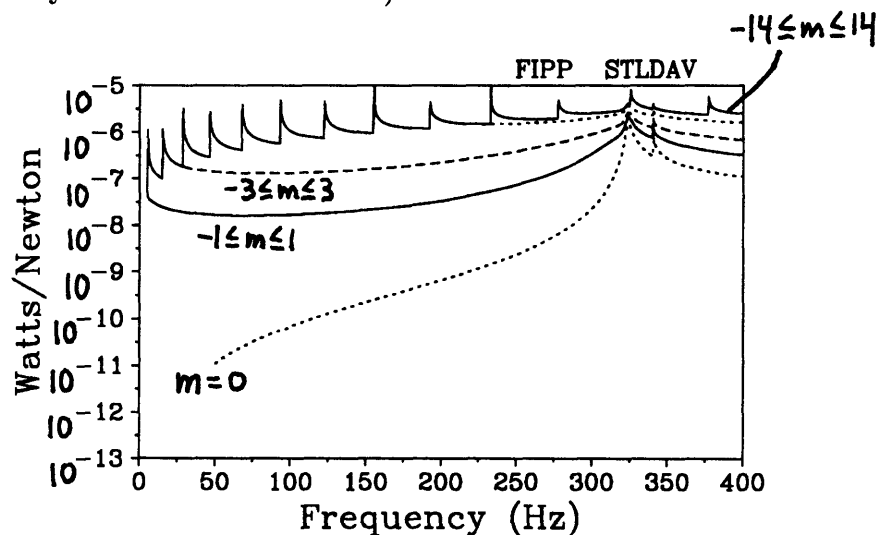


Figure 3-6: Time-averaged power input $\langle \Pi \rangle$ injected by a point force into the DGM shell model in vacuum. Note the convergence as more integer orders are included.

To interpret this figure, Borgiotti and Rosen correctly stated that the spikes in this plot occur at the cutoff frequencies where a flexural mode begins to propagate in the axial direction. This interpretation explains why higher frequencies require more orders, because higher frequencies allow more axially propagating flexural waves to carry power away from the input force. Borgiotti and Rosen also correctly interpreted these spikes as resonances.

I agree with their interpretations, and here I add two insights of my own. First, at the cutoff frequency for a given mode, a resonance of the type they mention is manifested in the wavenumber plane as a double pole exactly at the origin $s = 0$. This causes the response of the system to blow up everywhere in space, because the inverse wavenumber transform from wavenumber to space is not possible. Second, I note that all of the spikes in Fig. 3-6 for $|m| > 1$ are due to flexural modes. Knowing this, I can quantify the convergence shown in Fig. 3-6 by letting ν_c be the real order where cutoff occurs between propagating and non-propagating flexural waves at a given real frequency. For thin shells, this can be reasonably approximated by the formula $\nu_c^2 \approx (\omega/\omega_r)(\sqrt{12} R_s/T_s)$, as stated by Fahy [60]. Applying this formula to the highest frequency in Fig. 3-6, we have $\nu_c^2 \approx (400/340)(\sqrt{12} 2.5/0.05) \doteq 203.8$, so $\nu_c \approx \pm 14.3$. In fact, Fig. 3-6 shows that the power input converges when we include the integer orders $-14 \leq m \leq 14$.

For future reference, Fahy's formula cited above can be derived by considering the Donnell equations in vacuum and setting the axial wavenumber equal to zero. The homogeneous solutions of the resulting system correspond to the resonances of the cutoff frequencies. I show this procedure in detail below in section 3.3.5.

Figure 3-7 shows the power input by the point force when the shell is surrounded by water. This figure extends the results of Borgiotti and Rosen, because their thin-shell state vector formulation does not include fluid loading. The notable features are: 1) The resonance of the breathing mode at the ring frequency has become heavily damped, due to very heavy radiation damping. This mode radiates efficiently because the displacements of this mode form a monopole in the r - θ plane, so there is no cancellation around the circumference. In contrast, the $m = \pm 1$ modes form a dipole, etc., so there is some cancellation of their radiation around the circumference. 2) Fluid loading reduces the frequencies of the flexural resonances for $|m| > 1$. These resonances also have radiation damping, because when the frequency is increased above cutoff, these modes are initially supersonic. However, the radiation damping is light, because of the cancellation of radiation around the circumference. 3) Convergence of the series of integer orders is again determined by the number of flexural modes propagating, as it was for the shell in vacuum. In this case, the input power converges when we include the orders $-15 \leq m \leq 15$, because the fluid loading has decreased the resonance frequencies associated with the cutoff frequencies of the flexural waves.

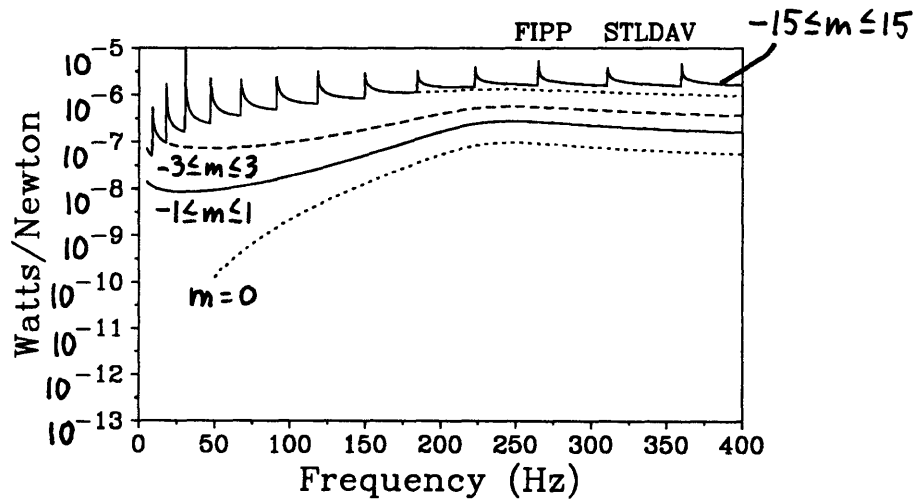


Figure 3-7: Time-averaged power input $\langle \Pi \rangle$ injected by a point force into the DGM shell model surrounded by water. Note the convergence as more orders are included.

3.3 Disagreement

This section shows some cases of disagreement between the DGM shell model and the Donnell thin shell model.

3.3.1 Disagreement for High Frequencies

At high frequencies, the Donnell equations overstate the speed of flexural waves. This happens for two reasons: 1) The Donnell equations neglect the rotatory inertia of the shell fibers. This fact is clear, because the density of the shell material appears in only three terms, which correspond to accelerations in the radial, circumferential, and axial directions. 2) The Donnell equations overstate the flexural stiffness, because their derivation involves the Kirchhoff hypothesis, which sets the transverse shear strains equal to zero. The error caused by this assumption becomes greater as the flexural wavelength decreases, and this occurs as frequency increases.

Both of these effects are well known in the case of the classical theory of flexure for a thin flat plate [1]. The onset of these effects is commonly identified in the case of a flat plate with heavy fluid loading in terms of the coincidence frequency, where the speed of sound in the fluid equals the speed of flexural waves in the classical theory in a vacuum. As the frequency approaches the coincidence frequency, the classical theory begins to overstate the flexural wavespeed.

Applying these concepts to the shell, a formula for the coincidence frequency was presented and applied to the shell at the beginning of this chapter. The result computed there was $f_c \doteq 4434$ Hz. To show what happens above the coincidence frequency, Fig. 3-8 shows the response of the shell for $f = 20f_c \doteq 6800$ Hz and $\nu = 0$.

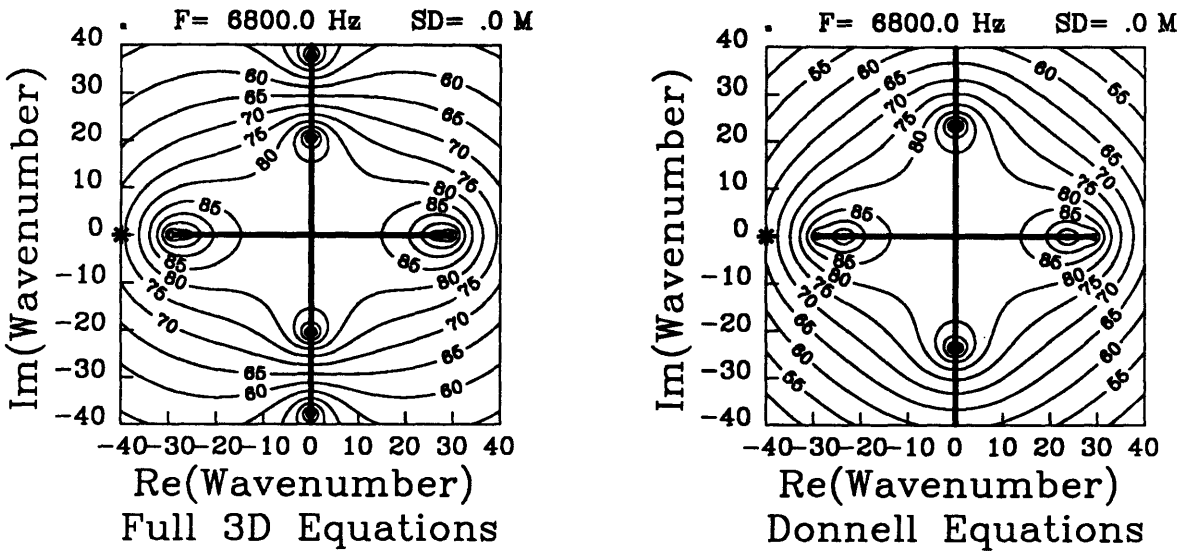


Figure 3-8: Disagreement above the coincidence frequency: Fluid pressure due to a ring force pushing in the radial direction for $\omega = 20\omega_r$, and $\nu = 0$. EJP branch cuts are chosen.

As expected, Fig. 3-8 shows that the Donnell equations overstate the speed of the flexural waves. In the wavenumber plane, this appears as the flexural poles for the Donnell equations are closer to the origin. This error is significant because of the proximity of the flexural poles to the branch points. This causes a significant difference in the launch angle of a leaky wave, as shown in the spatial domain in Fig. 3-9.

Incidentally, EJP branch cuts were chosen for Fig. 3-8 because the high frequency causes the solutions for the DGM model to become unstable in the region of the wavenumber plane between the EJP branch cuts and the Pekeris branch cuts. The solutions are stable elsewhere in the wavenumber plane, as shown by this figure. The cause of this instability is clear, as discussed in the last chapter. For now, note that this instability never arises along the axis of integration from wavenumber to space. Thus, we have no trouble computing the response in the spatial domain shown in Fig. 3-9.

Figure 3-9 shows the fluid pressure in the r - θ plane for $2.5 \text{ m} \leq r \leq 20 \text{ m}$ and $0 \leq z \leq 15 \text{ m}$, plotted in dB as $20 \log_{10} |p(r, 0, z)| / 1 \mu\text{Pa}$. The ring force is at the lower left hand corner of the figure, where $r = 2.5 \text{ m}$ and $z = 0 \text{ m}$. Thus, this figure has the same parameters as Fig. 3-5, except that the frequency is $20\omega_r$, rather than $5\omega_r$. A beam radiates from the source at the angle of coincidence between flexural waves and acoustic waves.

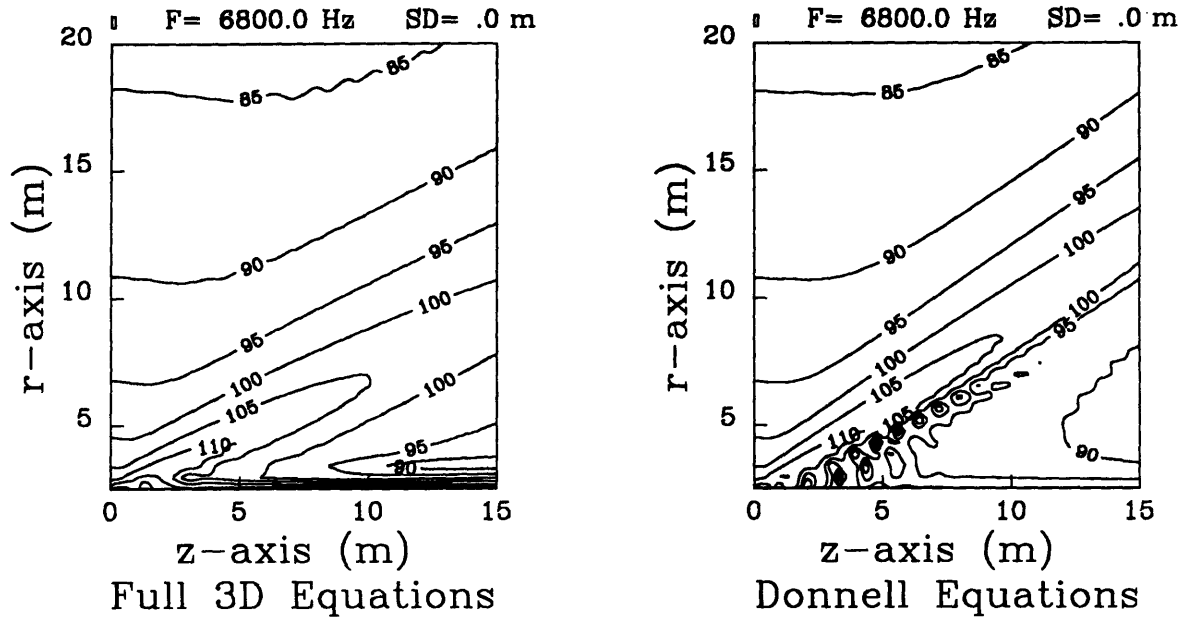


Figure 3-9: Disagreement above the coincidence frequency: Fluid pressure due to a ring force pushing in the radial direction for $\omega = 20\omega_r$, and $\nu = 0$.

3.3.2 Disagreement for Large Orders

Large circumferential orders impose short wavelengths on the shell in the circumferential direction, and this violates the assumptions of the Donnell thin shell theory. To quantify this, consider that the wavelength in the circumferential direction is $2\pi R_s/\nu$. For the Donnell theory to be valid, the flexural wavelengths must be larger than the shell thickness T_s by some factor. If we let that factor be 2π , then this requirement can be written as $(2\pi R_s/\nu)/T_s > 2\pi$. Re-arranging this, we have the requirement that $\nu < R_s/T_s$. Thus, for the shell being studied in this chapter, where $R_s = 2.5$ m and $T_s = 0.05$ m, we can only expect the Donnell equations to be valid for $\nu < 50$.

Figure 3-10 illustrates the onset of disagreement between the theories. A ring force is pushing in the radial direction with $\omega = 5\omega_r$ and $\nu = 50$. The pressure at the shell surface is plotted in dB in the wavenumber domain as $20 \log_{10}(|\hat{\sigma}_{rr}|/1\mu\text{Pa}/1\text{m})$. Both models predict similar pole locations for the waves involved. However, the Donnell equations predict lower amplitude levels of response, because that theory overstates the flexural stiffness for short wavelengths.

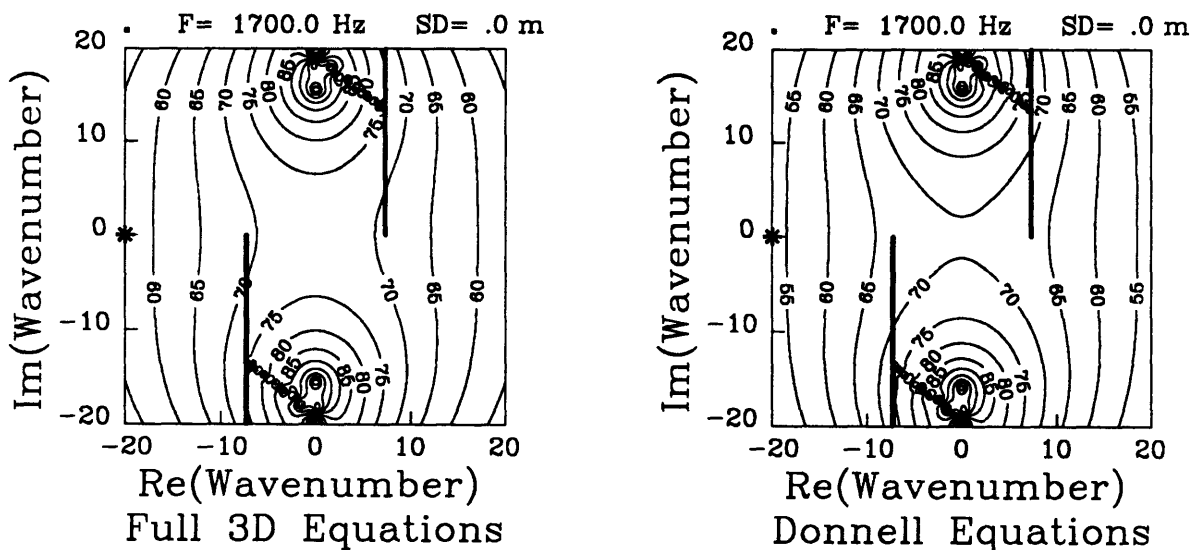


Figure 3-10: Disagreement for large order: Pressure at the shell surface due to a ring force pushing in the radial direction for $\omega = 5\omega_r$ and $\nu = 50$. Note lower response levels for the Donnell theory.

3.3.3 Disagreement for Drive Displacements

This chapter uses the DGM shell model as a reference model to check the accuracy of thin shell models. This makes sense, because the DGM model is based on the full 3D equations of elasticity, and the full 3D elastic results can be taken to be the “exact” answer to a problem.

However, the full 3D elastic equations lead to an artifact that I will discuss here. The displacement at the drive location goes to infinity whenever the full 3D equations are excited by forces concentrated with Dirac deltas to form point forces, line forces, or ring forces. Specifically, the *real* part of the displacement in the direction of the force goes to infinity, while the *imaginary* part of the displacement is finite.

This effect is well-known in certain intellectual communities. Awareness of this effect has its origins in the mid-19th century, when Lord Kelvin derived the solution of an elastic solid to a static point force. Later, in the beginning of the 20th century, Love published extensive documentation for the solutions of elastic solids to static point forces, point moments, line forces, and line moments [61]. And, considering dynamic excitations, many books on elastodynamics and boundary elements now document the response of an elastic solid to point forces and line forces that are time-harmonic [62], while some books document the response to point forces and line forces that are impulsive in the time domain [63].

To summarize this discussion of the history, note that in all of the cases cited above, the displacement in the direction of the applied force is always singular at the point where a force is applied, yet the singularity is always integrable. Indeed, the singularity must be integrable to make physical sense, considering that any physically realizable situation should involve finite displacements in response to forces applied over non-vanishing areas, and such situations can be formulated in terms of convolution integrals involving the response to point forces. Thus, the displacements in response to point forces must be integrable to allow the convolution integrals to converge and give finite displacements. Also, the fact that the singularity is integrable

has allowed the development of Boundary Element Methods (BEM), where the influence coefficients in a BEM model are defined in terms of the integration of the displacement over the area of a boundary element.

Now, having reviewed these well-known aspects concerning the singularity at the point of application, I will elaborate on how the singularity appears in the context of this thesis. This discussion will show us more about the properties of ring forces, wavenumber integrals, and the DGM method.

First, I'll discuss the real part of the drive displacement going to infinity. In effect, the applied force acts on a spring with a stiffness that goes to zero as the widths of the Dirac deltas go to zero. Physically, this means that an infinite amount of energy is alternately stored and released in a near-field elastic energy storage mechanism concentrated locally in a tiny volume around the point of application (considering a finite force acting through an infinite distance).

I can show how this happens mathematically in the wavenumber domain. Let the direction of a ring force be the vector \mathbf{a} , and let the displacement in the direction of the ring force be u_a . I can write this displacement in the wavenumber domain as the sum of homogeneous and particular solutions:

$$\hat{u}_a(r, \nu, s) = \hat{u}_a^H(r, \nu, s) + \hat{u}_a^P(r, \nu, s)$$

Examination of the particular solutions in Appendix A shows that the particular solutions go as $\hat{u}_a^P(r', \nu, s) \propto 1/s$ for large s . In contrast, the homogeneous solutions $\hat{u}_a^H(r', \nu, s)$ must decay exponentially with s for large s , assuming that there is some distance between the ring force radius r' and the interfaces where the boundary conditions must be satisfied. Therefore, if we try to integrate $\hat{u}_a(r', \nu, s)$ over wavenumber to get the displacement at the drive location $r = r'$ and $z = 0$, then the integral will diverge, because the integrand is dominated for large s by the “tail” of the integrand $\hat{u}_a^P(r', \nu, s) \propto 1/s$.

This effect can be seen graphically in Fig. 3-4. In that figure, there is general

agreement between the full 3D elastic results and the Donnell thin shell results over most of the wavenumbers shown. However, the results disagree in their amplitudes at the outer corners of the plots. At these wavenumbers, the full 3D elastic model shows more response, because the $1/s$ decay of $\hat{u}_r^P(r', \nu, s)$ is beginning to dominate the response here.

Now I'll discuss the imaginary part of the drive displacement being finite. This gives a finite time-averaged power $\langle \Pi \rangle$ injected into the system. The finite net power flow allows the full 3D elastic model to give physically meaningful results away from the ring force location, so the 3D elastic model can agree with the thin shell models considered above. Also, note that we are able to compute the time-averaged input power $\langle \Pi \rangle$ by integrating over wavenumber in Eq. (2.29). The integral in Eq. (2.29) converges because it defines an integrand that accounts only for the finite imaginary part of the drive displacement.

To confirm these observations about the drive displacements, Appendix C examines the drive point behavior of the full 3D equations excited by a time-harmonic point force in a solid medium of infinite extent. This problem has a relatively simple solution in terms of ∇ operations in the spatial domain. Thus, Appendix C confirms that the infinite drive displacement is not an artifact of wavenumber transform techniques or a flaw in our DGM implementation. The infinite drive displacement is inherent in the full 3D equations, and our DGM implementation is accurately reproducing this artifact.

As this artifact applies to the modeling of shells with the 3D elastodynamic theory, the reactions of ring stiffeners cannot be modeled by using concentrated ring forces, because the shell's impedance to this excitation is either undefined or zero. This artifact can be avoided by modeling the reactions of ring stiffeners by using stresses distributed over small but finite areas, rather than using stresses concentrated with Dirac deltas. The ring forces used in this thesis form a basis for modeling such distributed loads.

3.3.4 Disagreement for Moment Impedance

In 1960, Dyer showed that the classical theory of plate bending can overstate the impedance of a thin flat plate in response to a moment if the moment is applied to a small area [64]. Dyer showed that this can happen even when the plate thickness is small compared to the flexural wavelength, and the classical theory correctly states the flexural wavespeed and the impedance to a point force. The error arises because the small dimensions of the applied excitation cause local 3D shear deformations within the thickness of the plate. These deformations are not allowed in the classical flat plate theory, because the classical theory effectively sets these deformations equal to zero with the Kirchhoff hypothesis. Thus, the classical plate theory overstates the moment impedance because it does not allow this flexibility within the thickness of the plate.

To discuss Dyer's effect in the context of this thesis, I will call Dyer's excitation a "disk moment," because Dyer applied the moment by modeling a rigid disk embedded in the Mindlin flat plate theory. He rocked this disk back and forth to transmit a moment to the plate. Thus, I avoid calling his excitation a "point moment." A true "point moment" would be concentrated in space with Dirac deltas, and this would cause infinite drive point response in the full 3D elastic theory, as discussed in the previous subsection. That artifact is not the effect I am discussing here. In this subsection, I am discussing errors due to loads that are applied over small but non-vanishing areas.

Based on Dyer's result, I claim that the Donnell equations will also overstate the impedance of a thin shell in response to a disk moment, because the Donnell equations also involve the Kirchhoff hypothesis. The fact that the Donnell equations involve the Kirchhoff hypothesis can be easily seen by noting that flexural effects are accounted for in both theories by a biharmonic operator ∇^4 . In the classical plate theory, ∇^4 operates in the 2D middle surface of the plate; in the Donnell equations, ∇^4 operates in the 2D middle surface of the shell.

Here I will briefly discuss the effect demonstrated by Dyer in terms of the scales of length involved. Textbooks commonly state that thin plate and thin shell theories are valid when the *wavelengths* in the plates and shells are large compared to the *thicknesses* of the plates and shells. However, Dyer's paper introduced another scale of length. He applied the moment to the plate over a circle having some *radius*. Dyer demonstrated that errors arise when the radius of the moment application is on the order of the thickness.

A complementary interpretation of Dyer's effect is to consider it to be a case of "disagreement for large orders" (see subsection 3.3.2 above). This interpretation is another way of analyzing the fact that the error is associated with the small length scale of the applied moment. Small lengths in the circumferential direction correspond to large circumferential orders.

To judge the significance of Dyer's effect in structural applications, we should note that his excitation was small in two dimensions (being a small disk) and the excitation was antisymmetric (being a rocking motion). Thus, Dyer's effect may or may not be significant at joints between ribs and shells, because those joints are small in only one dimension (the thickness of the rib). Final judgement on this issue would require full 3D elastic reference modeling of interactions between plates and shells.

3.3.5 Disagreement for Very Low Frequencies

Below the ring frequency, the shell can behave globally in bending as a beam. When the frequency is *very* low compared to the ring frequency, the Donnell equations fail to predict this beam bending mode correctly.

To demonstrate this effect clearly, I consider the shell to have no fluid loading in this subsection. This allows clear comparisons with the classical theory of beam bending. Also, with the fluid loading removed, the Donnell equations in Eq. (3.1) reduce to a 3 by 3 system with 8 algebraic roots.

Figure 3-11 shows the beam bending mode clearly in both models. This figure shows the response to a radial ring force of order $\nu = 1$ at 0.01 times the ring frequency. The radial displacement is shown in the wavenumber domain as 20 $\log_{10}(|\hat{u}_r(r', s)|/1\text{m}^2)$. The significant thing to note in this figure is that the Donnell equations do support the beam bending mode in this case.

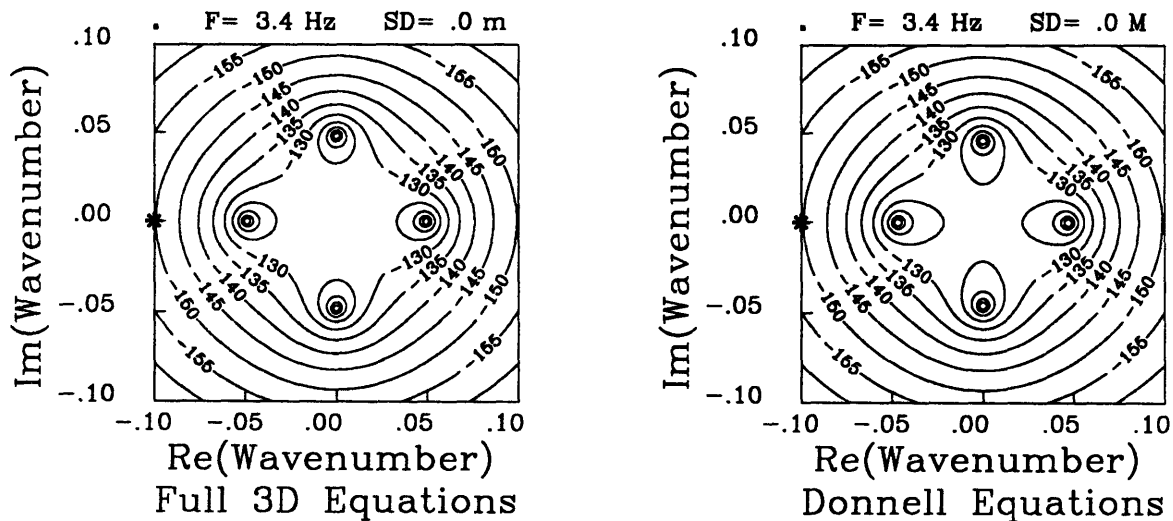


Figure 3-11: Beam bending mode at low frequency in vacuum. Radial displacement is shown in the wavenumber domain for radial ring forcing with $\nu = 1$ at 0.01 times the ring frequency.

Classical beam bending theory predicts the pole locations very well. Let ρ_b be the linear density of a beam. For the shell, $\rho_b \approx 2\pi R_s T_s \rho_s \doteq 6126 \text{ kg/m}$. Let I_b be the cross-sectional moment of inertia of a beam. For the shell, $I_b \approx 2\pi R_s^3 T_s / \sqrt{2} \doteq 3.47$

m^4 . Thus, the flexural rigidity of the shell in beam bending is $E_s I_b \doteq 701 \times 10^9 \text{ kg m}^3 \text{ s}^{-2}$. Let $U_b(z)$ be the transverse deflection of a beam in bending. In the classical theory of beam bending, the propagation of bending waves is governed by:

$$\partial^4 U_b(z) / \partial z^4 + k_b^4 U_b(z) = 0 \quad (3.2)$$

where k_b is the flexural wavenumber:

$$k_b^4 = [\rho_b / (E_s I_b)] \omega^2 \quad (3.3)$$

Thus, Eq. (3.2) predicts the 4 poles at $s \approx \pm k_b, \pm i k_b$. Letting the frequency be 0.01 times the ring frequency, the theory predicts $k_b \doteq 0.0447 \text{ m}^{-1}$, in good agreement with Fig. 3-11.

However, Fig. 3-12 shows that the Donnell equations do not support the beam bending mode at *very* low frequencies, while the full 3D elastic equations show that the beam bending mode should still exist. This figure was computed using a radial ring force of order $\nu = 1$ at 0.001 times the ring frequency. The radial displacement is shown in the wavenumber domain as $20 \log_{10}(|\hat{u}_r(r', s)| / 1 \text{m}^2)$. Equation (3.3) predicts $k_b \doteq 0.0141 \text{ m}^{-1}$, and this agrees well with the full 3D elastic solution. However, the Donnell equations predict that the waves decay exponentially and cannot carry power down the length of the shell.

To study the cutoff in the Donnell equations, Leissa's book on shell theory suggests that we should let the axial wavenumber go to zero and look for the homogeneous solutions [27]. In this limit, Eq. (3.1) approaches the form:

$$\begin{bmatrix} 1 + \epsilon_s \nu^4 - \omega^2 / \omega_r^2 & i\nu & 0 \\ -i\nu & \nu^2 - \omega^2 / \omega_r^2 & 0 \\ 0 & 0 & \nu^2(1 - \vartheta_s) / 2 - \omega^2 / \omega_r^2 \end{bmatrix} \begin{Bmatrix} \hat{U}_r \\ \hat{U}_\theta \\ \hat{U}_z \end{Bmatrix} = \begin{Bmatrix} 0 \\ 0 \\ 0 \end{Bmatrix}$$

The beam bending mode is associated with $\hat{U}_r, \hat{U}_\theta$, and the upper left submatrix of

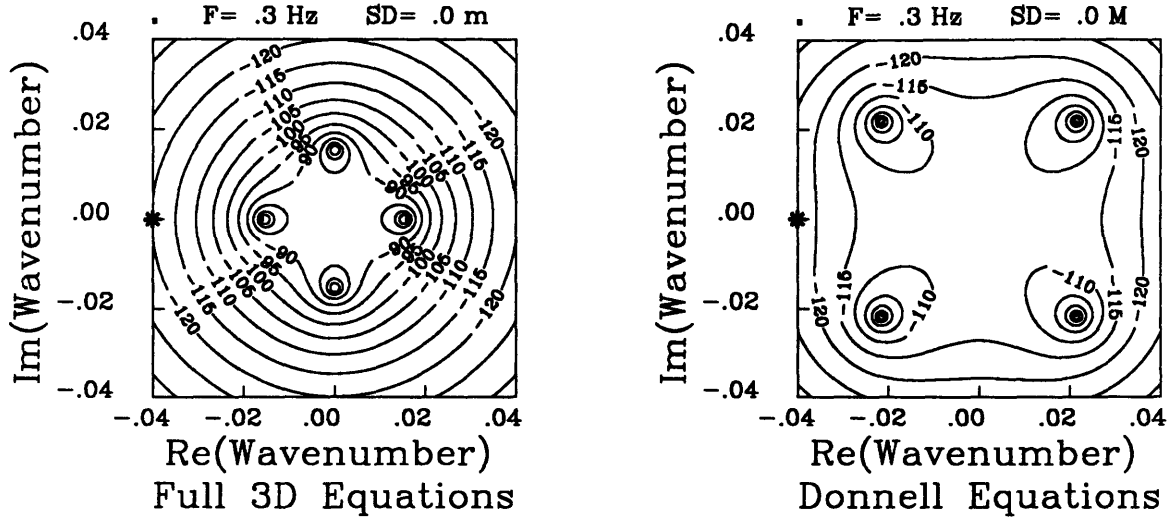


Figure 3-12: Disagreement at low frequencies. Radial displacement is shown in the wavenumber domain for radial ring forcing with $\nu = 1$ at 0.001 times the ring frequency.

this equation. Leissa specifies the determinant of this submatrix to be zero:

$$\omega^4/\omega_r^4 - (1 + \nu^2 + \epsilon_s \nu^4)\omega^2/\omega_r^2 + \epsilon_s \nu^6 = 0$$

and he uses the quadratic formula to identify the cutoff frequencies:

$$\frac{\omega^2}{\omega_r^2} = \frac{(1 + \nu^2 + \epsilon_s \nu^4) \pm \sqrt{(1 + \nu^2 + \epsilon_s \nu^4)^2 - 4\epsilon_s \nu^6}}{2}$$

Here, I let $\nu = \pm 1$ for the case of beam bending, and this simplifies to:

$$\frac{\omega^2}{\omega_r^2} = 1 + \epsilon_s/2 \pm \sqrt{1 + (\epsilon_s/2)^2}$$

Considering ϵ_s to be small in this last expression, the positive sign leads to $\omega^2/\omega_r^2 \approx 2$, which is not the low frequency root I seek. Thus, I use the negative sign, which leads to:

$$\frac{\omega^2}{\omega_r^2} \approx \frac{\epsilon_s}{2} = \frac{T_s^2}{24R_s^2}$$

Letting $T_s/R_s = 0.02$, we find the root for the cutoff frequency is $\omega/\omega_r = \pm 0.00408$. This value explains the difference between Figs. 3-11 and 3-12. Figure 3-11 shows

that the Donnell theory *does* allow the propagation of beam bending waves above this cutoff frequency, while Fig. 3-12 shows that the Donnell theory does *not* allow the propagation of beam bending waves below this cutoff frequency. The full 3D elastic reference model shows that this cutoff does not occur in the physically correct solution.

Beam bending is modeled accurately at very low frequencies by the thin shell equations derived in a paper by Scott [58]. Scott's equations are identical to the Donnell equations, except that where the Donnell equations account for flexural effects with the biharmonic operator ∇^4 , Scott's equations use an algebraic expression of his own derivation. Considering Scott's equations with no fluid loading, I made the following two observations:

- Analytically, I set the circumferential order equal to one, and I let the axial wavenumber be very small. In this limit, I considered how Scott's equations could give a determinant of zero in the matrix form in the wavenumber domain. I found that as I let the axial wavenumber go to zero, the frequency of a homogeneous solution must go to zero. Thus, the Scott equations continue to propagate beam bending waves as the frequency goes to zero.
- Numerically, I computed Fig. 3-13 below. This figure is identical to Fig. 3-12, except that the Scott equations are used in place of the Donnell equations. This figure shows that Scott's equations accurately model beam bending behavior at very low frequencies in both amplitude and wavelength.

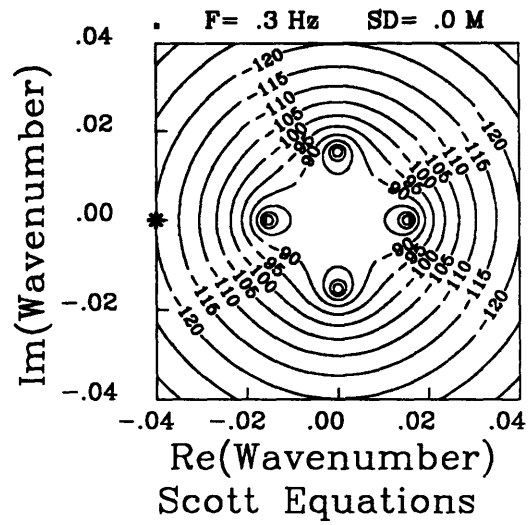
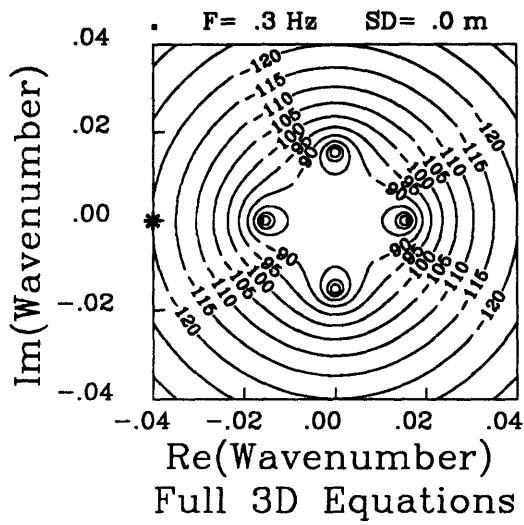


Figure 3-13: Beam bending modeled accurately by the Scott equations. Radial displacement is shown in the wavenumber domain for radial ring forcing with $\nu = 1$ at 0.001 times the ring frequency.

3.4 Accounting for Eccentric Forcing

So far, this thesis has considered ring forces applied to the middle surface of the shell. However, the stiffeners that might be attached inside a real shell can be considered to act on the inner surface of the shell. Therefore, this section considers what happens when ring forces are located away from the middle surface of the shell. I call this type of excitation “eccentric forcing.”

When the ring force is located away from the middle surface of the shell, and the ring force pushes in the circumferential direction \mathbf{a}_θ or the axial direction \mathbf{a}_z , then the offset of such a ring force from the middle surface effectively introduces a “ring couple” that should be added to a thin shell theory. This effect is known to some people who work with thin plate and thin shell theories, but I have not seen it discussed in any textbooks. The point of considering the effect here is that I can use the DGM shell model as a reference model, so I can demonstrate the effect clearly.

Defining the ring couple is a simple matter of vector mechanics. Let the radius $r = r_m$ locate the *middle* surface of the shell, and let the radius $r = r_a$ locate a surface *away* from the middle surface of the shell. A ring force that is located *away* from the middle surface of the shell can be interpreted as a ring force at the *middle* surface of the shell, plus a ring couple:

$$F_\theta \mathbf{a}_\theta \delta(r - r_a) e^{i\nu\theta} \delta(z) e^{-i\omega t} = F_\theta \mathbf{a}_\theta \delta(r - r_m) e^{i\nu\theta} \delta(z) e^{-i\omega t} + F_\theta [\mathbf{a}_\theta \delta(r - r_a) - \mathbf{a}_\theta \delta(r - r_m)] e^{i\nu\theta} \delta(z) e^{-i\omega t} \quad (3.4)$$

$$F_z \mathbf{a}_z \delta(r - r_a) e^{i\nu\theta} \delta(z) e^{-i\omega t} = F_z \mathbf{a}_z \delta(r - r_m) e^{i\nu\theta} \delta(z) e^{-i\omega t} + F_z [\mathbf{a}_z \delta(r - r_a) - \mathbf{a}_z \delta(r - r_m)] e^{i\nu\theta} \delta(z) e^{-i\omega t} \quad (3.5)$$

Note that substituting \mathbf{a}_r into the equations above would not create a couple, so there are only two ring couples that can arise by changing the radius of the ring forces.

Now I will show how these ideas arise in a specific example. To begin, Fig. 3-14 shows the response of the shell models to circumferential ring forcing with $\omega = 5\omega_r$ and $\nu = 5$. The ring forces are located at the middle surface of the shell. The pressure at the shell surface is shown in dB as $20 \log_{10}(|\hat{\sigma}_{rr}|/1\mu\text{Pa}/1\text{m})$. The notable features are: 1) The poles for the flexural waves. These poles are located at $s \approx \pm 13 \text{ m}^{-1}$. These poles are excited to the same amplitudes in both models. 2) The full 3D elastic model has some zeros in the corners of the plot that are not in the Donnell model. However, these zeros do not represent a significant difference between the models, because the response at those points is not significant in either model. 3) The poles for the membrane compression and shear waves are located in the center of the figure. A better view of these poles was shown in Fig. 3-2. That figure shows the response of the same shell to the same excitation, except that the range of wavenumbers shown there is $-4 \leq s \leq 4 \text{ m}^{-1}$. In that figure, we see that the poles for the membrane compression and shear waves are excited to the same amplitudes in both models. The significant point to note from Figs. 3-2 and 3-14 is that when both models are excited at the middle surface of the shell, both models respond with waves having the same amplitudes.

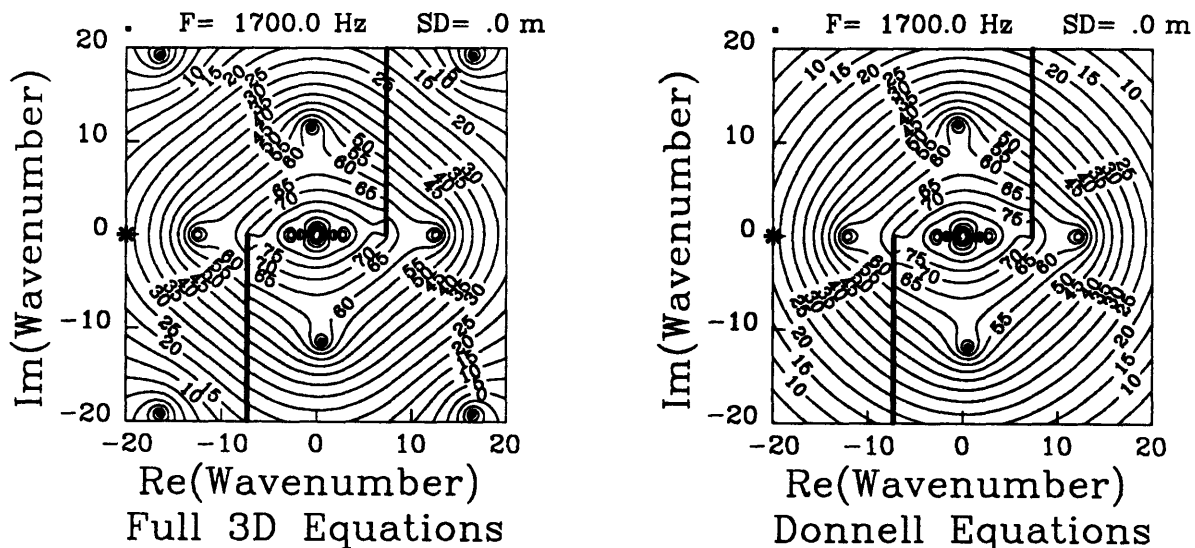


Figure 3-14: Fluid pressure at the shell surface for circumferential ring forcing with $\omega = 5\omega_r$ and $\nu = 5$, plotted as $20 \log_{10}(|\hat{\sigma}_{rr}|/1\mu\text{Pa}/1\text{m})$. Pekeris branch cuts are chosen. Wavenumber axes are shown in m^{-1} . The ring force is located at the middle surface. Note that flexural waves are excited to the same amplitude in both models.

Next, Fig. 3-15 shows how the full 3D elastic model responds when I change the radius of the ring force from $r' = 2.5$ m to $r' = 2.476$ m. I chose this radius to be very close to the inner surface of the shell ($R_1 = 2.475$ m), while not being exactly at the inner surface of the shell. This retains the physical meaning of having the force embedded in the solid while the zero-stress boundary conditions are applied at the inner surface of the shell. In the limit as the ring force approaches the inner surface of the shell, the theory remains valid and the software remains well-behaved. The significant point to note in this figure is that the flexural waves are more strongly excited by the eccentric forcing. This effect is clearly explained by Eq. (3.4), which shows that moving the ring force away from the middle surface introduces a ring couple. This ring couple causes the higher amplitudes of the flexural waves.

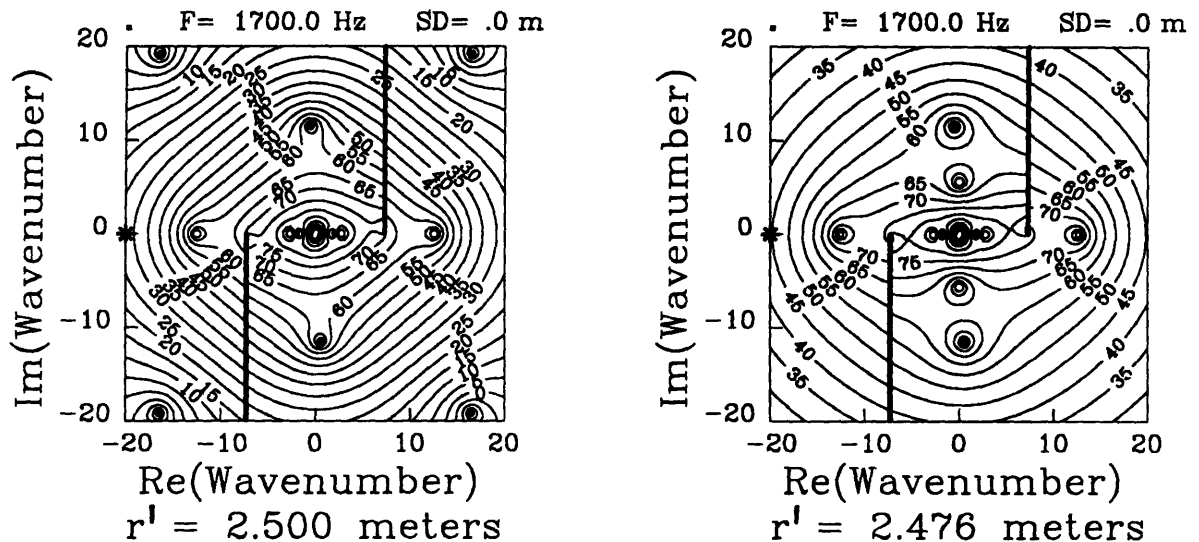


Figure 3-15: Fluid pressure at the shell surface for circumferential ring forcing with $\omega = 5\omega_r$ and $\nu = 5$, plotted as $20 \log_{10}(|\hat{\sigma}_{rr}|/1\mu\text{Pa}/1\text{m})$. Pekeris branch cuts are chosen. Wavenumber axes are shown in m^{-1} . Both plots are for the full 3D elastic model. Note that the eccentric forcing causes higher amplitudes for the flexural waves at $s \approx \pm 13 \text{ m}^{-1}$.

To see how the membrane waves are affected by the eccentric forcing, Fig. 3-16 shows us a better view of the center of Fig. 3-15. The significant point to note here is that the amplitude of the membrane waves is unchanged by relocating the ring force. This fact is also clearly explained by Eq. (3.4). Applying the ring force away from the middle surface is equivalent to applying the ring force at the middle surface (thus creating similar membrane waves) and applying a ring couple (which does not affect the membrane waves).

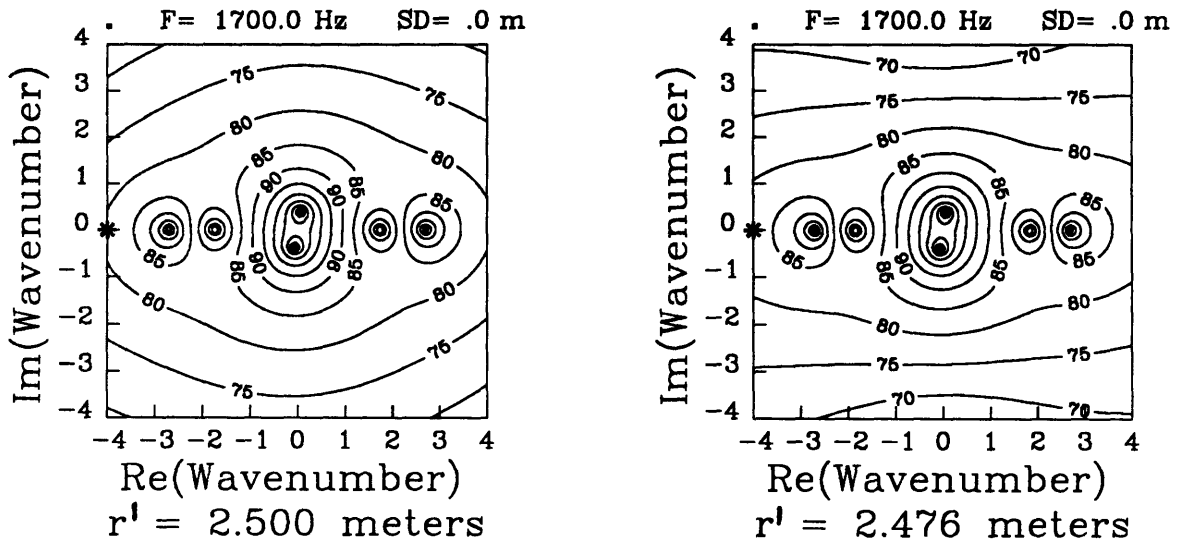


Figure 3-16: Fluid pressure at the shell surface for radial ring forcing with $\omega = 5\omega_r$ and $\nu = 5$, plotted as $20 \log_{10}(|\hat{\sigma}_{rr}|/1\mu\text{Pa}/1\text{m})$. Pekeris branch cuts are chosen. Wavenumber axes are shown in m^{-1} . Both plots are for the full 3D elastic model. Note that the eccentric forcing does not change the amplitude of the membrane shear waves (at $s \approx \pm 2.7 \text{ m}^{-1}$) and compression waves (at $s \approx \pm 0.7i \text{ m}^{-1}$).

The ring couples demonstrated here can also be applied to a thin shell model if desired. Recall that the couple of circumferential ring forces shown in Eq. (3.4) was:

$$F_\theta [\mathbf{a}_\theta \delta(r - r_a) - \mathbf{a}_\theta \delta(r - r_m)] e^{i\nu\theta} \delta(z) e^{-i\omega t}$$

This applies a twisting moment to the shell on the circle $z = 0$. The twisting moment acts about the z -axis, and it is distributed over the circumferential angle θ with the form:

$$F_\theta (r_a - r_m) e^{i\nu\theta} \delta(z) e^{-i\omega t}$$

Considering that the Donnell equations involve the Kirchhoff assumption, this twisting moment is properly applied to the shell in terms of Kirchhoff's supplemental force.

Also, recall that the couple of axial ring forces shown in Eq. (3.5) was:

$$F_z [\mathbf{a}_z \delta(r - r_a) - \mathbf{a}_z \delta(r - r_m)] e^{i\nu\theta} \delta(z) e^{-i\omega t}$$

This applies a bending moment to the shell on the circle $z = \text{constant}$. The bending moment acts about the θ -axis with the form

$$-F_z (r_a - r_m) e^{i\nu\theta} \delta(z) e^{-i\omega t}$$

This moment can be applied in terms of the derivative of a radial ring force with respect to z :

$$F_z (r_a - r_m) \mathbf{a}_r \delta'(z) e^{i\nu\theta} e^{-i\omega t}$$

Chapter 4

A Technique for Attaching a Plate

This chapter develops a technique for attaching a thin elastic plate inside the multi-layered DGM shell model. The plate is circular, and mounted normal to the axis of the shell, as shown in Fig. 4-1. In this chapter, the innermost layer of the DGM shell model is a vacuum, so the plate and the shell interact only through the shaded surfaces in Fig. 4-1. Aside from this restriction, the DGM shell model is free to have external fluid loading and any number of viscoelastic layers.

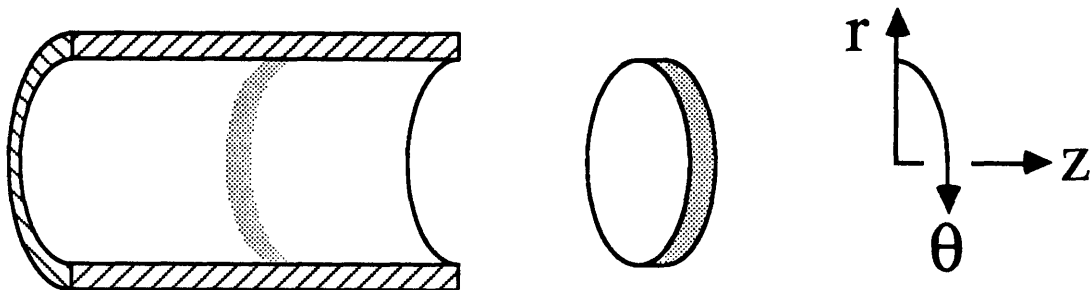


Figure 4-1: Attaching a thin plate inside the DGM shell model.

4.1 Possible Approaches

Ideally, the plate would be modeled with the full 3D equations of elastodynamics, just as the DGM shell model is. This approach would create a full 3D elastodynamic reference model of a welded joint between a plate and a fluid-loaded shell. This problem can be classified as a “contact problem” between two full 3D elastodynamic bodies. Solving such a contact problem is feasible in this case of a shell in contact with a plate, because this thesis establishes a numerically stable DGM description of a shell excited by ring forces, and the circular plate could also be described using separation of variables and solved using DGM techniques for plane layered media. However, even though this approach is feasible, it would involve some complications:

- One complication is the issue of the stress concentrations. For the canonical geometry of a plate meeting the shell at a 90° angle without a weld fillet, the full 3D elastodynamic solution would involve stress concentrations at the corners between the plate and the shell. The stresses would go to infinity here. To represent these stresses, we would need to choose some basis functions that converge on infinity at the edges at the welded joint, while the basis functions must also converge on finite solutions through the thickness of the welded joint. One possible approach used by other authors is to expand the unknown stresses in terms of orthogonal polynomials multiplied by a weighting function that reproduces the stress concentration [65].
- Another complication is that the unknown coefficients of the basis functions would have to be related in a well-conditioned way to allow a numerically stable solution. This issue is addressed by Schmidt and Krenk for a case where the contact involves only normal stress and normal displacement, as though the bodies are lubricated [65]. The case of welded contact may involve additional difficulties in stability and convergence.
- Another possible complication is the dimension of the computation required. Solving a scattering problem involves a computational loop over frequencies,

and inside that loop there will be a loop over circumferential orders. Inside these two loops, where the frequency and order can be taken to be fixed, we would need to compute the interaction stresses to some desired degree of accuracy. It appears that this computation would involve a loop to determine the amplitudes of the basis functions, and determining each amplitude would involve a loop over wavenumbers.

Therefore, to avoid these complications in this thesis, the plate will be modeled with a thin plate theory. This will allow me to describe the shell-plate interactions in terms of 3 resultant forces and 2 resultant moments, observed where the middle surface of the plate intersects the inner surface of the shell. Solving for these 5 unknowns will involve less computation than solving for the distribution of unknown stresses in the weld. Also, the issues of conditioning and infinite stress will be avoided.

But how can we join a thin plate theory to the DGM shell model? I consider the compatibility of the different theories in Fig. 4-2. Typically, thin plate theories for flexure assume that the extensional stresses vary linearly across the thickness of the plate. Also, they assume that the straight fibers across the thickness of the plate remain straight, so the deflections involve the simple rocking motion shown in Fig. 4-2. However, if we were to apply the same linear distribution of stress to the DGM shell model, would the DGM shell model respond with a simple rocking motion, where straight fibers on the inner surface of the shell remain straight? To first order, it would, but to higher order, it would not.

Thus, we see there is a slight incompatibility between the two theories. If we try to satisfy equilibrium at all points across the thickness of the welded joint, then we will violate structural continuity. Another way to see this incompatibility is to note that the DGM shell model can represent a stress concentration where the plate meets the shell, but the typical thin plate theory cannot represent a stress concentration.

Therefore, this thesis defines a way to connect the two theories in an integral sense. I satisfy Newton's third law in an integral sense by equating the resultant

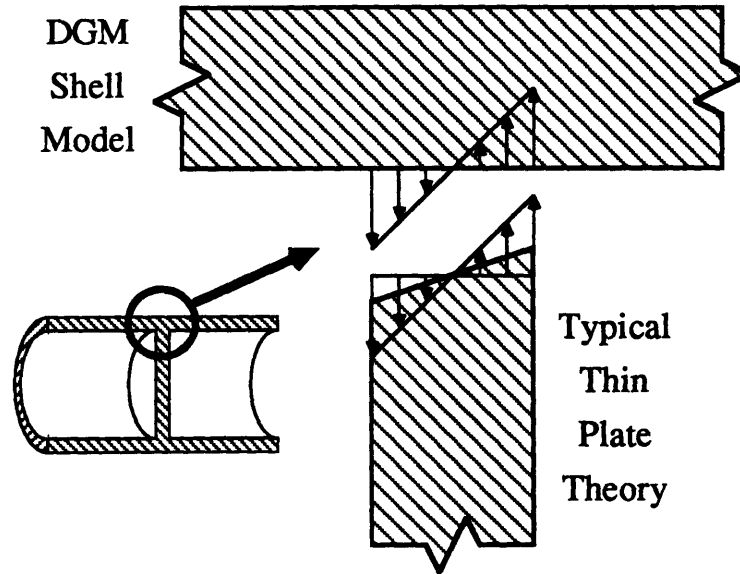


Figure 4-2: The DGM shell model and a typical thin plate theory.

forces and moments between the plate and the shell. Thus, every action has an equal and opposite reaction, in an integral sense. And, I satisfy structural continuity in an integral sense by defining equivalent velocities for the DGM shell model that satisfy conservation of energy. In other words, any power given up by the plate through the joint equals the power entering the shell through the joint.

4.2 Resultant Forces and Moments

This section reviews the fact that the stresses on the shaded surfaces in Fig. 4-3 can create 3 resultant forces and 2 resultant moments. This fact is well known, so it is reviewed here mainly to establish my nomenclature and sign conventions.

Consider a plate welded into a shell. Let the thickness of the plate be T_p . Let the inner surface of the shell be $r = R_1$. Let's cut the shell and the plate apart along this surface, and consider the stresses on the plate. The stresses here are $\sigma_{rr}(R_1, \theta, z)$, $\sigma_{r\theta}(R_1, \theta, z)$, and $\sigma_{rz}(R_1, \theta, z)$. The stresses create 3 resultant forces that are easy to

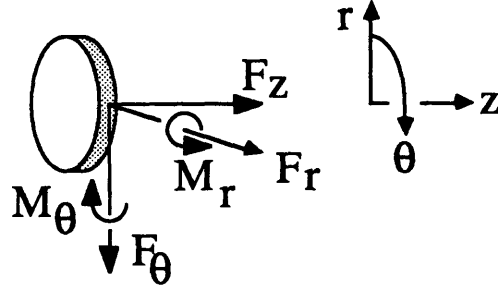


Figure 4-3: Resultant forces and moments.

understand:

$$F_r(R_1, \theta) = \int_{-T_p/2}^{T_p/2} \sigma_{rr}(R_1, \theta, z) dz \quad (4.1)$$

$$F_\theta(R_1, \theta) = \int_{-T_p/2}^{T_p/2} \sigma_{r\theta}(R_1, \theta, z) dz \quad (4.2)$$

$$F_z(R_1, \theta) = \int_{-T_p/2}^{T_p/2} \sigma_{rz}(R_1, \theta, z) dz \quad (4.3)$$

These resultant forces have units of force per length along the circumference, and they act on the outer edge of the plate in the positive r , θ , and z -directions, respectively. In addition, the stresses create 2 resultant moments that require more effort to understand:

$$M_r(R_1, \theta) = - \int_{-T_p/2}^{T_p/2} \sigma_{r\theta}(R_1, \theta, z) z dz \quad (4.4)$$

$$M_\theta(R_1, \theta) = \int_{-T_p/2}^{T_p/2} \sigma_{rr}(R_1, \theta, z) z dz \quad (4.5)$$

These resultant moments have units of moment per length along the circumference. $M_r(R_1, \theta)$ is the twisting moment on the outer edge of the plate due to inplane shear stress, and it is defined here to act on the plate about the positive r -axis. The sign of this definition agrees with Timoshenko [66] and Dyer [64], but the sign is opposite to that of Mindlin [67] and other authors. $M_\theta(R_1, \theta)$ is the bending moment on the outer edge of the plate, and it acts on the plate about the positive θ -axis.

But is this list of 5 resultants complete? This question can be asked and answered two different ways:

- Physically, in terms of resultants, why don't we define a 3rd moment, which would act about the z -axis? The answer is that such a moment is already accounted for by $F_r(R_1, \theta)$, which can vary with respect to θ , just as $\sigma_{rr}(R_1, \theta, z)$ can, which would presumably be the source of such a moment. In this context, we see that the role of the 2 moments $M_r(R_1, \theta)$ and $M_\theta(R_1, \theta)$ is to account for the moments that the 3 resultant forces cannot account for.
- Mathematically, in terms of integrals, why don't we define a 3rd integral, which would involve $\int_{-T_p/2}^{T_p/2} \sigma_{rz}(R_1, \theta, z) z dz$? The answer is that this integral creates no resultant force or moment in any direction. True, this integral will have some non-zero value in the full 3D elastodynamic solution of a welded stiffener attachment, because $\sigma_{rz}(R_1, \theta, z)$ will have an odd part with respect to $z = 0$. However, this integral does not have meaning in terms of a resultant, and any effects due to the odd part of σ_{rz} (like energy storage, or flexibility) must be left to future research.

In conclusion, note that I have defined the resultant forces and moments to be positive when they act on the plate in the positive coordinate directions. In the next section, I will also define the translational and rotational velocities to be positive in the positive coordinate directions. These conventions will simplify our thoughts about all the interactions between the plate and the shell.

4.3 Solution via Admittance Matrices

This section defines a method to solve for the response of the DGM shell model with a thin elastic plate welded inside. The system might be excited by a point source in the fluid, a point force on the shell, an incident structural wave in the shell, or an obliquely incident plane wave in the fluid.

First, I assume an angular dependence of $e^{i\nu\theta}$. Thus, the discussions that follow are valid for a given order ν that might be involved in a synthesis of orders that solve

a scattering problem. The factor $e^{i\nu\theta}$ is implied from here on in this chapter.

Second, I define \mathbf{F}_i to be a vector of resultant forces that acts on the plate due to interactions with the shell:

$$\mathbf{F}_i \equiv \{ F_r, F_\theta, F_z, M_r, M_\theta \}_i \quad (4.6)$$

where the subscript “i” denotes “interaction.” I define the entries to be positive when they act on the plate in the positive coordinate directions. This convention is shown above in Fig. 4-3 and quantified in Eqs. (4.1-4.5).

Third, I define \mathbf{V}_{pi} to be a vector of velocities observed at the outer edge of the circular plate, caused by \mathbf{F}_i :

$$\mathbf{V}_{pi} \equiv \left\{ \begin{array}{c} \dot{U}_r \\ \dot{U}_\theta \\ \dot{U}_z \\ \Omega_r \\ \Omega_\theta \end{array} \right\}_{pi} = \left[\begin{array}{ccccc} Y_{11} & Y_{12} & 0 & 0 & 0 \\ Y_{21} & Y_{22} & 0 & 0 & 0 \\ 0 & 0 & Y_{33} & Y_{34} & Y_{35} \\ 0 & 0 & Y_{43} & Y_{44} & Y_{45} \\ 0 & 0 & Y_{53} & Y_{54} & Y_{55} \end{array} \right]_p \left\{ \begin{array}{c} F_r \\ F_\theta \\ F_z \\ M_r \\ M_\theta \end{array} \right\}_i \quad (4.7)$$

I define the velocities to be positive in the positive coordinate directions, as shown in Fig. 4-4. The velocities \dot{U}_r , \dot{U}_θ , and \dot{U}_z are translational velocities, while Ω_r and Ω_θ are rotational velocities. The subscript “p” denotes “plate,” and the 5×5 matrix for the plate in Eq. (4.7) is defined in Appendix E. Equation (4.7) can be written in a more compact way as:

$$\mathbf{V}_{pi} \equiv [\mathbf{Y}]_p \mathbf{F}_i$$

Similarly, I define \mathbf{V}_{si} to be a vector of velocities observed in the DGM shell model, caused by $-\mathbf{F}_i$. The subscript “s” denotes “shell.” I write the minus sign in front of \mathbf{F}_i here because of Newton’s third law, which states that every action has an equal and opposite reaction. For example, if F_r has a positive sign, then the plate is being pulled in tension, as shown in Fig. 4-3, so the force we apply to the shell must

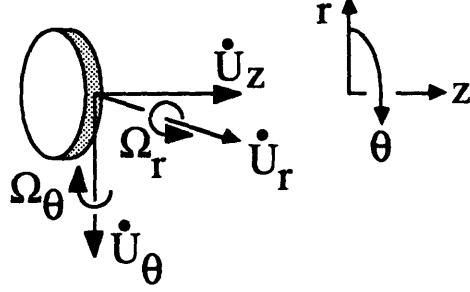


Figure 4-4: Translational and rotational velocities.

pull the shell inward, in the negative coordinate direction. Thus, I write \mathbf{V}_{si} as the velocity caused by $-\mathbf{F}_i$:

$$\mathbf{V}_{si} \equiv \begin{Bmatrix} \dot{U}_r \\ \dot{U}_\theta \\ \dot{U}_z \\ \Omega_r \\ \Omega_\theta \end{Bmatrix}_{si} = - \begin{bmatrix} Y_{11} & Y_{12} & 0 & 0 & 0 \\ Y_{21} & Y_{22} & 0 & 0 & 0 \\ 0 & 0 & Y_{33} & Y_{34} & Y_{35} \\ 0 & 0 & Y_{43} & Y_{44} & Y_{45} \\ 0 & 0 & Y_{53} & Y_{54} & Y_{55} \end{bmatrix}_s \begin{Bmatrix} F_r \\ F_\theta \\ F_z \\ M_r \\ M_\theta \end{Bmatrix}_i \quad (4.8)$$

The 5×5 matrix for the shell in Eq. (4.8) is defined in Appendix F. Equation (4.8) can be written in a more compact way as:

$$\mathbf{V}_{si} \equiv -[\mathbf{Y}]_s \mathbf{F}_i$$

Next, I define \mathbf{V}_{empty} to be a vector of velocities observed in the shell when the shell is “empty” (i.e., without the plate attached inside) and excited by some external excitation (e.g., an incident acoustic wave). To satisfy structural continuity, the linear superposition of \mathbf{V}_{empty} and \mathbf{V}_{si} must equal the velocities for the plate:

$$\mathbf{V}_{pi} = \mathbf{V}_{si} + \mathbf{V}_{empty} \quad (4.9)$$

Re-writing this equation in terms of the admittance matrices, we have:

$$[[\mathbf{Y}]_p + [\mathbf{Y}]_s] \mathbf{F}_i = \mathbf{V}_{empty} \quad (4.10)$$

This is the equation I solve to get the interaction forces \mathbf{F}_i .

At this point, I should say more about my definitions of the velocities. In Appendix E, I define an admittance matrix for the plate $[\mathbf{Y}]_p$ that gives the plate's velocities \mathbf{V}_{pi} in response to the interactions \mathbf{F}_i as $\mathbf{V}_{pi} = [\mathbf{Y}]_p \mathbf{F}_i$. These definitions are straightforward, because the thin plate theories used in this thesis assume that straight fibers across the thickness of the plate remain straight. Thus, the translational velocities in \mathbf{V}_{pi} are simply the translational velocities of the fibers (\dot{U}_r , \dot{U}_θ , and \dot{U}_z), and the rotational velocities in \mathbf{V}_{pi} are simply the rotational velocities of the fibers (Ω_r and Ω_θ).

However, the DGM shell model responds with more complicated displacement fields. Straight fibers on the inner surface of the shell do not remain perfectly straight. Clearly, this creates some ambiguity in defining the rotational velocities (Ω_r and Ω_θ), and it also creates ambiguity in defining the translational velocities (\dot{U}_r , \dot{U}_θ , and \dot{U}_z).

I solve this problem in Appendix F, where I define an admittance matrix for the shell $[\mathbf{Y}]_s$ that gives the shell's velocities \mathbf{V}_{si} in response to the interactions \mathbf{F}_i as $\mathbf{V}_{si} = [\mathbf{Y}]_s \mathbf{F}_i$. These definitions assume some forms for the distributed loads applied to the DGM shell model. Given these assumed forms, I compute the response of the shell to these loads, and I integrate over the thickness of the joint to characterize the instantaneous power transfer across the joint. Finally, I define the velocities \mathbf{V}_{si} to give the same instantaneous power transfer across the joint when used with the resultants \mathbf{F}_i .

Finally, I need to define the velocities of the “empty” shell $\mathbf{V}_{\text{empty}}$ in a way that is consistent with my definitions of \mathbf{V}_{pi} and \mathbf{V}_{si} . To define $\mathbf{V}_{\text{empty}}$, I take the complex conjugates of both sides of Eq. (4.9), and I multiply from the left by the transpose of \mathbf{F}_i , so I have:

$$\mathbf{F}_i^T \mathbf{V}_{pi}^* = \mathbf{F}_i^T \mathbf{V}_{si}^* + \mathbf{F}_i^T \mathbf{V}_{\text{empty}}^* \quad (4.11)$$

The left-hand side of this equation characterizes the power entering the plate through

the joint, while the right-hand side of this equation characterizes the power leaving the shell through the joint. From this equation, I see that I want $\mathbf{V}_{\text{empty}}$ to be defined the same way I define \mathbf{V}_{si} in Appendix F, where the distributed velocities of the shell are multiplied by the assumed forms for the distributed loads. I show how I compute this at the end of Appendix F.

Chapter 5

Acoustic Scattering

In this chapter, I show how I can compute the scattering of an obliquely incident acoustic plane wave from an infinitely long cylindrical shell. The shell may be empty, or it may contain a thin elastic plate. The shell may have any number of viscoelastic layers. Figure 5-1 shows the shell, the plate, and the incident wave. The shell is drawn cut away to show that the plate is located at $z = 0$.

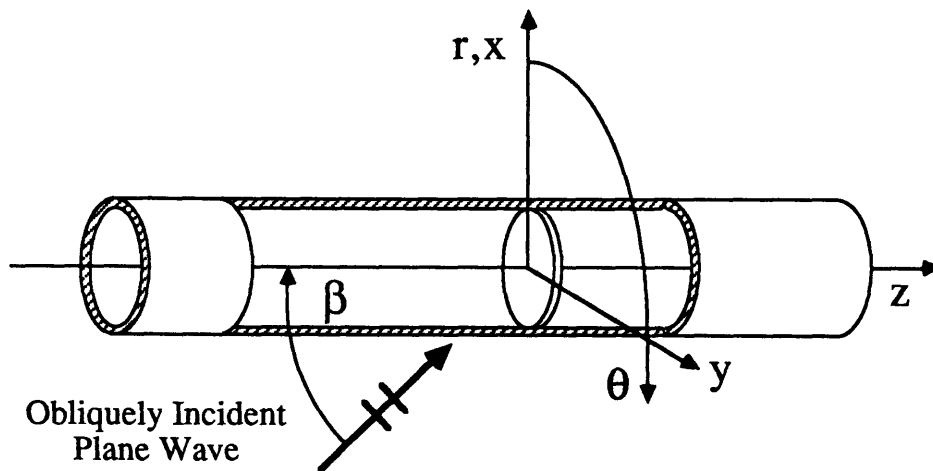


Figure 5-1: Geometry for the acoustic scattering problem.

5.1 Scattering from Empty Shells

In this section, I use the DGM shell model to solve for the scattering from empty shells. The shells can have any number of viscoelastic layers.

Using the arguments presented in Appendix G, I used Eq. (G.7) to compute the following figures for the form functions of empty shells. To observe backscattering, the angle θ equals π , so $e^{im\theta} = (-1)^m$. I truncated the summation over integer orders at a value of m equal to twice the highest value of $h_N R_{N-1}$ considered. The parameter $h_N R_{N-1}$ is labeled on the figures as ka , where k is the wavenumber in the surrounding fluid and a is the outer radius of the shell.

Figures 5-2 through 5-4 verify the DGM computations for normal incidence over a very wide range of frequencies. These figures show the form function for the backscattering at normal incidence from a single layered shell containing a vacuum and surrounded by water. These figures were computed with the shell parameters assumed by Veksler and Korsunskii [6]. The ratio of the inner radius to the outer radius is $R_1/R_2 = 63/64$. The shell material is iron, which is modeled with a density of 7700 kg/m³, a longitudinal wavespeed of 5960 m/s, and a shear wavespeed of 3240 m/s. The water is modeled with a density of 1000 kg/m³ and a wavespeed of 1493 m/s. The figures shown here agree very well with the figures published by Veksler and Korsunskii.

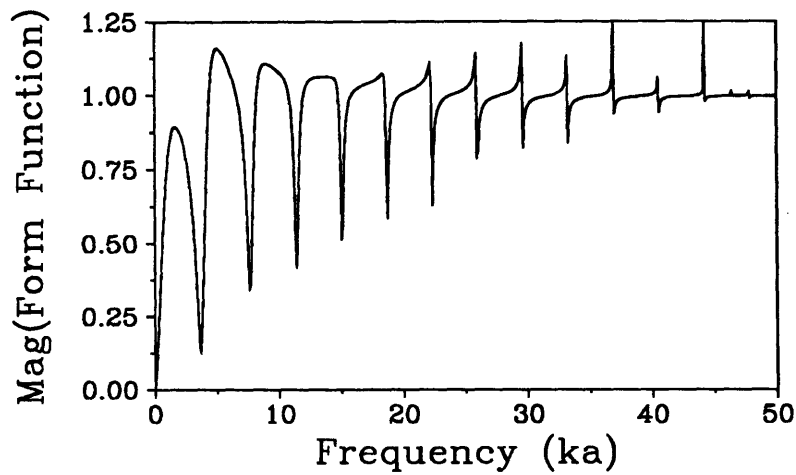


Figure 5-2: Magnitude of the form function for backscattering at normal incidence from a single-layered shell. Response is computed for $0 \leq ka \leq 50$ by including the integer orders $-100 \leq m \leq 100$.

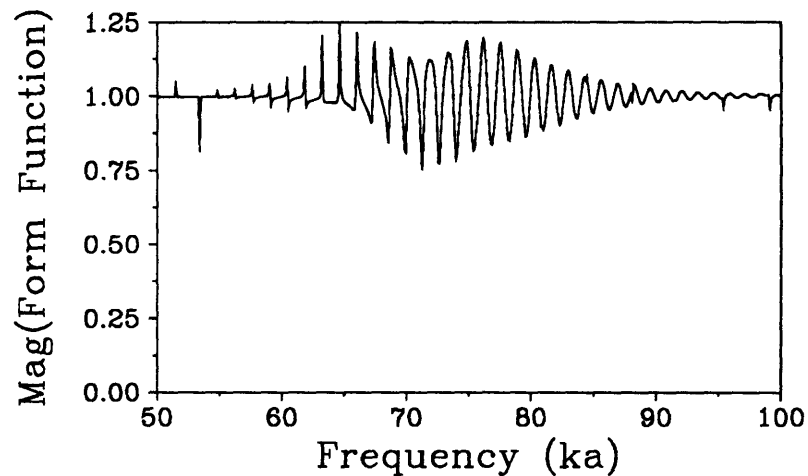


Figure 5-3: Magnitude of the form function for backscattering at normal incidence from a single-layered shell. Response is computed for $50 \leq ka \leq 100$ by including the integer orders $-200 \leq m \leq 200$.

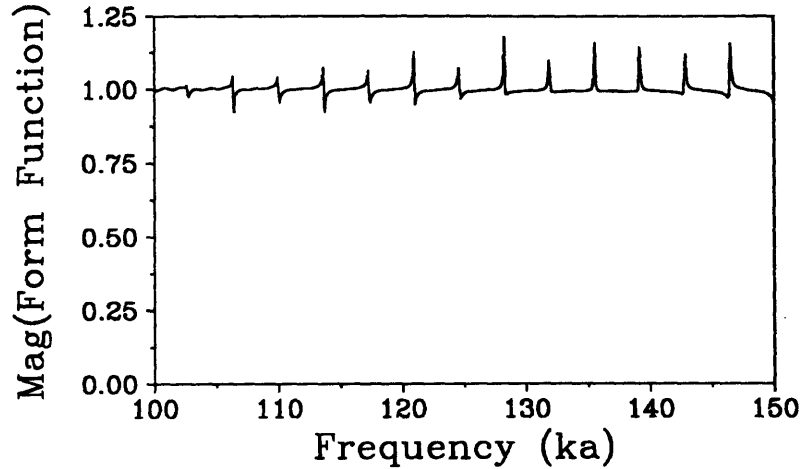


Figure 5-4: Magnitude of the form function for backscattering at normal incidence from a single-layered shell. Response is computed for $100 \leq ka \leq 150$ by including the integer orders $-300 \leq m \leq 300$.

Figure 5-5 verifies the DGM computations at oblique incidence. This figure shows the form function for the backscattering at oblique incidence in the specular direction from a single layered shell containing air and surrounded by water. These figures were computed with the shell parameters assumed by Léon *et al* [11]. The ratio of the inner radius to the outer radius is $R_1/R_2 = 0.84$. The shell material is aluminum, which is modeled with a density of 2790 kg/m^3 , a longitudinal wavespeed of 6380 m/s , and a shear wavespeed of 3100 m/s . The water is modeled with a density of 1000 kg/m^3 and a wavespeed of 1493 m/s . The air is modeled with a density of 1.2 kg/m^3 and a wavespeed of 330 m/s . Backscattering is computed ($\theta = \pi$), and the angle of incidence β is 81° from the axis of the shell. The figure shown here agrees very well with the figure published by Léon *et al*.

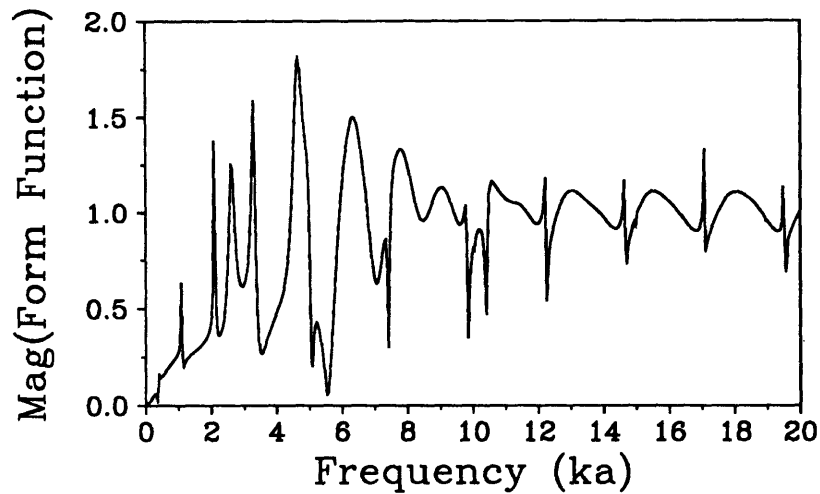


Figure 5-5: Magnitude of the form function for the backscattering at oblique incidence in the specular direction for a single-layered shell. Response is computed for $0 \leq ka \leq 20$ by including the integer orders $-40 \leq m \leq 40$.

Figure 5-6 demonstrates the DGM results for the scattering from a multi-layered shell at oblique incidence. The shell is similar to the shell in Fig. 5-5, but a layer of a viscoelastic damping material has been sandwiched between two layers of aluminum. The innermost layer is air, with an outer radius $R_1 = 0.68$ m. The next layer is aluminum, with an outer radius $R_2 = 0.76$ m. The next layer is a viscoelastic material, with an outer radius $R_3 = 0.84$ m. The next layer is aluminum, with an outer radius $R_4 = 1$ m. The outermost layer is water, which radiates to infinity. The air, aluminum, and water have the same properties used to compute Fig. 5-5.

The viscoelastic material has a density of 1200 kg/m^3 , a compression wavespeed of 2853 m/s , and a shear wavespeed of 1386 m/s . A loss factor of 1 was assumed for each frequency. I assumed this to provide an optimistic calculation of the damping effect possible at any given frequency. Real damping materials have loss factors that vary with frequency for physical reasons, and a frequency dependent loss factor is also necessary to give causal results in the time domain.

As in Fig. 5-5, backscattering is computed in the specular direction, and the angle of incidence β is 81° from the axis of the shell. The damping of resonances is evident.

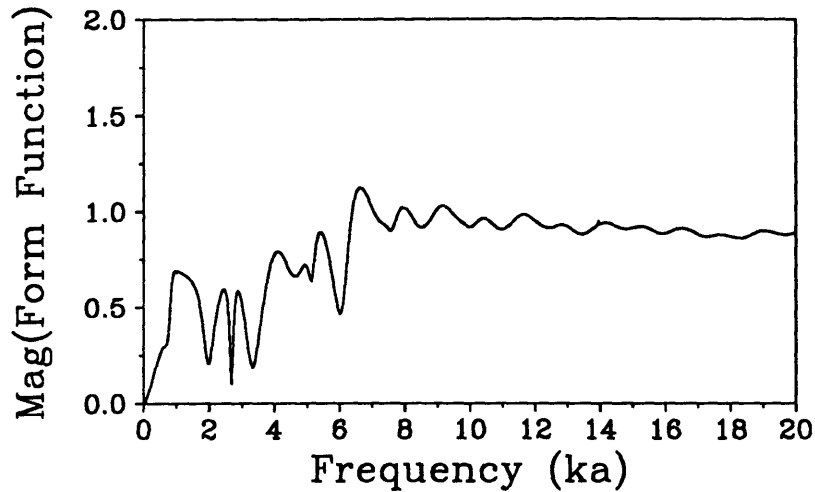


Figure 5-6: Magnitude of the form function for the backscattering at oblique incidence in the specular direction for a multi-layered shell. Response is computed for $0 \leq ka \leq 20$ by including the integer orders $-40 \leq m \leq 40$.

Figure 5-7 shows the response computed with the same parameters used to compute Fig. 5-6, except that the loss factor for the viscoelastic layer has been set equal to zero. The sharp resonances in this figure demonstrate that the loss factor was significant in reducing the scattering from the shell.

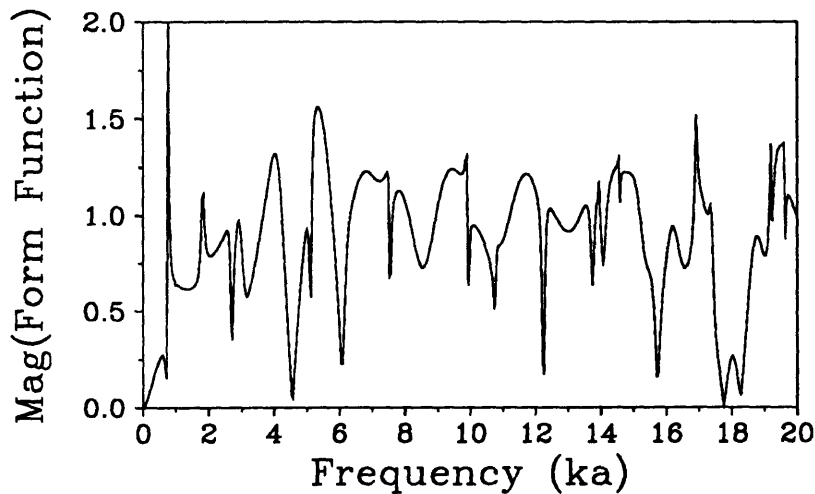


Figure 5-7: Magnitude of the form function for the backscattering at oblique incidence in the specular direction for a multi-layered shell. Response is computed for $0 \leq ka \leq 20$ by including the integer orders $-40 \leq m \leq 40$.

5.2 Scattering from Stiffened Shells

In this section, I show how I can use the DGM shell model to solve for the scattering from a multi-layered shell stiffened by an internally attached plate. The solution involves the following steps:

1. I can use the DGM method to solve for the response due to the incident plane wave acting on an unstiffened shell, as I demonstrated in the previous section. This problem is solved using the DGM techniques shown in Appendix G. This procedure was demonstrated and validated by comparison with previously published results in the section above.
2. Given the solution of the unstiffened shell problem, I can compute the shell velocities at the attachment location that will be compatible with the thin plate theory in an integral sense of conserving momentum and power. The formulas for doing this are shown at the end of Appendix F. I have checked these formulas by the arguments shown at the end of that Appendix. These formulas will give us the vector $\mathbf{V}_{\text{empty}}$.
3. I can compute an admittance matrix for the plate $[\mathbf{Y}]_p$ using the formulas in Appendix E. I have verified these formulas by coding them in Fortran and observing the checks described at the end of that Appendix.
4. I can compute an admittance matrix for the shell $[\mathbf{Y}]_s$ using the formulas in Appendix F.
5. I can solve for a vector of reactions \mathbf{F}_i by solving Eq. (4.10):

$$([\mathbf{Y}]_p + [\mathbf{Y}]_s) \mathbf{F}_i = \mathbf{V}_{\text{empty}}$$

6. I can apply the vector of reactions \mathbf{F}_i to the shell and compute the spherically spreading scattered field due to the plate. The details of this are shown at the end of Appendix G.

In conclusion, all of the steps of this procedure are in place, except for one problem. At this date of writing, the integrals for computing the admittance matrix for the shell $[\mathbf{Y}]_s$ are not yet converging. I understand why this is so. In the spatial domain, the plate is thin compared to the lengths of the waves that propagate in the shell. Thus, in the wavenumber domain, the poles corresponding to the propagating waves are clustered close to the origin compared to the scale of the decay of the windows which are used to apply the forces and moments to the shell. Therefore, the windows define the integrals to converge in theory, in the sense that the integral is defined to have a finite value as a result, but the windows do not yet help convergence numerically. I believe that these integrals over wavenumber can be made to converge accurately by separating the integrand into different parts that will account for these different wavenumber scales separately. I recommend this as future work in Chapter 6, and I present the technical issues in detail in Appendix F.

Chapter 6

Conclusions and Future Work

This chapter presents my conclusions and my suggestions for future work.

6.1 Structural Acoustics

This thesis established the following points in the field of structural acoustics:

- Chapter 2 developed a numerically stable solution technique for the full 3D equations of elastodynamics for cylindrically layered viscoelastic systems. The solution technique is based on the Direct Global Matrix (DGM). The DGM solutions formulated here are numerically stable over a wide range of frequencies ω , axial wavenumbers s , and circumferential orders ν . Using the DGM formulation defined in this thesis, the range of numerical stability is adequate for structural acoustics. The DGM models can include fluid loading, as well as viscoelastic layers for damping and decoupling.

The value of this numerical DGM technique for structural acoustics is that it provides a “reference model” for checking the behavior of theories about shells and fluid loading. The value of reference modeling was shown to some degree

in Fig. 3-12, where it was shown that the Donnell thin shell theory failed to predict the global beam bending mode at very low frequencies. Looking to the future, such reference modeling will become increasingly valuable in checking the behavior of shell theories for multi-layered shells, where we can expect more assumptions, more theories, and more controversy.

- Chapter 3 used a DGM shell model as a reference model to check the behavior of three relatively simple thin shell theories. Generally good agreement was seen, as expected. Disagreement was seen for high frequencies and large circumferential orders, as expected. In conclusion, the simple thin shell theories considered here are qualitatively valid for structural acoustics over a fairly wide range of frequencies ω , axial wavenumbers s , and circumferential orders ν . The exception to this conclusion is the failure of the Donnell thin shell theory to predict the global beam bending mode at very low frequencies, as shown in Fig. 3-12. The Scott equations correctly support this mode, as shown in Fig. 3-13.
- Chapter 4 developed a modeling technique for attaching a thin flat plate inside a DGM shell model. The plate was modeled with the Mindlin plate theory. Therefore, the modeling technique is approximate, rather than exact. This approach is valuable for two reasons: 1) It allows a full 3D elastic representation of a multi-layered shell to interact with some internally attached feature in a simple way, so the effectiveness of viscoelastic layers in the shell can be investigated without any of the assumptions that would be required to develop a thin-shell theory for multi-layered shells. 2) The numerical difficulties encountered in this approximate solution of the contact problem will be instructive for future work.
- Chapter 5 showed how we can compute the scattering from a multi-layered shell with an internally attached plate. We saw that the contact problem between the shell and the plate involves its own numerical difficulties of stability and convergence, even for the approximate solution of the contact problem formulated in Chapter 4. The documentation of the numerical difficulties presented here will be useful when the contact problem is attempted again with a full 3D

elastic shell welded to a full 3D elastic plate.

Beyond these points, some questions remain for future work:

- Considering that stiffeners are attached away from the middle surface of a shell, we know that this eccentricity induces some additional moments that could be accounted for. It remains an open question how significant these moments might be in the context of a complex structure. These effects could be investigated using thin shell and thin plate theories, with the moments being added explicitly.
- The effect of local flexibility in a welded joint was briefly considered in subsection 3.3.4. It remains an open question how significant this flexibility might be in the context of a complex structure. Recently, the subject of local effects on global structural behavior has been addressed by some researchers in a rather theoretical or abstract way [68]. The subject could be addressed in a more concrete way by making full 3D elastodynamic reference models of welded joints between shells and stiffeners. The DGM shell model developed in this thesis would be perfectly suitable for this work.
- The role of flexural waves in radiation and scattering could be understood better. It has often been said that because flexural waves are subsonic in a flat plate, then they do not radiate. However, the near-field flexural waves create the lobe of direct radiation shown in Fig. 3-5, and this lobe can contribute to some kind of radiation pattern for a complex structure. Also, the traveling flexural wave for $\nu = 0$ becomes supersonic at high frequencies, as shown in Fig. 3-8, and this causes the beam of radiation shown in Fig. 3-9. These issues can be investigated with thin shell theories.
- A study could be done to demonstrate the advantages and disadvantages of the different approaches for synthesizing solutions over circumferential orders. The use of complex orders has been advocated by Pierce [47] and Felsen [48] [49] [50]. A theoretical benefit of this approach is that as the frequency increases, the

solutions decay strongly in the circumferential direction, so the image sources in the extended angular domain $-\infty < \theta < \infty$ contribute less and less to the physical solution, and thus the physical solution becomes dominated by the real source only. In theory, the resulting solution can be evaluated using residue calculus in the complex order plane. This appears elegant in theory, but in practice, how expensive is it numerically to compute Bessel functions of complex orders and implement the residue calculus?

For comparison, a synthesis over integer orders has been used by Schmidt to describe the scattering of acoustic pulses from a spherical shell, with the frequency being complex [40]. The rationale behind Schmidt's approach is that integer orders allow the use of recurrence relations for the Bessel functions for greater computational efficiency, while the complex frequencies speed the convergence of the solutions over circumferential orders when the waves in the circumferential direction have very little attenuation. As another argument in favor of Schmidt's approach, note that complex frequencies involve no increase in computational difficulty, because the wavenumber synthesis already requires that the Bessel function generators be able to accept complex arguments. In contrast, the use of complex orders requires more sophisticated Bessel function generators that must be debugged over a larger parameter space of argument and order, because the order must be extended to be complex. However, as a question about Schmidt's approach, do complex frequencies speed the convergence of solutions that involve waves that decay very strongly in the circumferential direction?

To my knowledge, no single person has implemented these different approaches and presented a comparison of their advantages and disadvantages on a set of example problems.

- At this date of writing, my integrals that define the admittance matrix for the DGM shell are not yet converging. The reasons for this were presented briefly at the end of Chapter 5, and presented in more detail in Appendix F. To solve

this problem, the slowly decaying tails of the integrands should be subtracted out analytically and integrated separately. The integration could be numerical, as I suggest in Appendix F.

- If we implement such a full 3D elastodynamic model of a welded joint, we will encounter more numerical issues of convergence and stability of the numerical representation of the unknown displacements and stresses across the weld. For future reference, a successful approach to a slightly simpler contact problem is demonstrated in a paper by Schmidt and Krenk [65].
- The admittance matrices defined in this thesis have some interesting properties of symmetry and antisymmetry. Some examples were shown for the plate in Eqs. (E.9) and (E.10), and some examples were shown for the shell in Eqs. (F.35) and (F.36). Those examples were computed for the special case of low frequency and order $\nu = 1$. Furthermore, for the plate, I have observed that the patterns of symmetry and antisymmetry shown in those equations hold true for all frequencies and orders. This provides a good check on numerical calculations. However, I cannot yet make a similar observation about the matrix for the shell, because the integrals that define the matrix are not yet converging numerically. It would be interesting to see if these properties of symmetry and antisymmetry could be proven somehow. The antisymmetry within the matrices appears to arise because the admittance matrices for the plate and the shell were defined in terms of a traveling wave description in the circumferential direction, so a factor of $e^{i(\nu\theta - \omega t)}$ was always implied. I believe that some theorems of reciprocity could be derived to explain these properties. I would start with a dynamic theorem of reciprocity between point excitations and responses, and then involve them in an integral over $e^{i\nu\theta}$.
- Several questions remain about the dynamics of thin shells at very low frequencies. As I discussed in subsection 3.3.5, the Donnell equations do not support the beam bending mode at very low frequencies, while the Scott equations do properly support the beam bending mode. This raises several questions in terms

of physics, numerics, and mathematics:

1. Physically, what goes wrong in the Donnell theory? What assumptions are being violated, evidently by the wavelengths being *long* compared to the shell thickness and radius? The problem is manifested in the use of the biharmonic operator ∇^4 to account for flexural effects. Why does this go wrong, and what is different about Scott's accounting of the flexural effects? Scott's paper provides some energy arguments that could provide a framework for these physical questions in terms of energy. What is the role of flexural energy in this very low frequency beam bending mode? How does the Donnell theory model this energy wrong? Or, as another approach, the book by Markuš discusses how some thin shell theories differ in terms of how they approximate the kinematics of the shell displacements [29]. Kinematically, what goes wrong in the Donnell theory?
2. Physically, are Scott's equations valid for non-integer orders? Or do the physical arguments in Scott's derivation limit his theory to integer orders? I classify this as a physical question, because non-integer orders can have the physical interpretation of being the eigenvalues for shells that are cut open so they don't close onto themselves, or shells that have longitudinal inhomogeneities like longitudinal stiffeners or masses. If Scott's equations are valid for non-integer orders, and if we consider Scott's operator Q that accounts for flexural effects, does Q vary smoothly from non-zero orders down to order zero?
3. Numerically, when I evaluated the Scott equations to produce Fig. 3-13, I had to use double precision to get a smooth plot. I imagine that this means that some numbers were being added and subtracted that were of different orders of magnitude. If this is true, does this numerical situation reflect some physical truth about the roles of different physical effects, or was it just a case of an inappropriate numerical treatment? In either case, it would be interesting to examine the magnitudes of the numbers involved.

4. Mathematically, considering the full 3D elastic model as a reference model, and considering the circumferential order ν to be a continuous variable, is there something special about the order $\nu = 1$? Consider that Fig. 3-6 showed that the flexural waves in the full 3D elastic theory do have cutoff frequencies for $\nu = 2, 3, 4$, etcetera. Why does the flexural wave for $\nu = 1$ *not* have a cutoff frequency in the full 3D elastic theory? To pursue this question graphically, we could restrict ω and ν to be real to define the ω - ν plane, and then we could plot the locus of cutoff frequencies in the ω - ν plane. As $\omega \rightarrow 0$, does the locus approach some asymptotic value of ν that is non-zero? Does the locus of points cross $\nu = 1$ or not? Do these answers depend on the physical parameters of the shell?

6.2 The DGM Method Itself

In this section, I offer some observations about the DGM method itself and I offer some suggestions for its future development. My comments here address the three issues of importance for any numerical solution technique: numerical stability, numerical accuracy, and numerical efficiency.

6.2.1 Numerical Stability

The numerical stability of the DGM formulation developed in this thesis is more than adequate for structural acoustics. For example, Fig. 3-4 shows stable DGM results up through order $\nu = 200$, and Fig. 3-8 shows stable DGM results at 20 times the ring frequency. However, every model has its limitations, so I will note two cases of instability that I've found:

- I tried computing Fig. 3-8 with Pekeris branch cuts, and unstable solutions appeared in the areas of the wavenumber plane between the EJP branch cuts and

the Pekeris branch cuts. The reason for this is clear. When EJP branch cuts are used, the evanescence always satisfies the radiation condition, and the solutions are physical in that sense. And, in this thesis, we achieved numerical stability based on physical considerations of evanescence. Specifically, we represented the potentials with Eqs. (2.13-2.15), and this lead to the matrix structure shown in Fig. 2-2, where certain coefficients vanish exponentially by design. However, in the portion of the wavenumber plane uncovered by the Pekeris branch cuts, the solutions are non-physical, in the sense that they violate the radiation condition. In this case, Eqs. (2.13-2.15) cause exponential growth of the coefficients that were intended to vanish in Fig. 2-2. This leads to unstable solutions in that region of the wavenumber plane. High frequency exacerbates this problem, because it increases the arguments of the Bessel functions.

The significance of this instability is that it can prevent us from seeing the leaky poles in contour maps in the wavenumber domain. However, this instability will never arise along the axis of integration from wavenumber to space, so it does not affect solutions in the spatial domain.

- I tested the DGM code at ultrasonic frequencies to see how it could work for non-destructive testing (NDT). Considering a borehole with a 6 cm radius, lined with a steel casing, excited at 1 MegaHertz, I have noticed some regions of instability in the wavenumber plane when I computed solutions above order $\nu = 100$. This instability appears even when I use the EJP branch cuts. This instability should be investigated and removed so the DGM method can be used reliably for ultrasonic work. I suspect that these very large circumferential orders are causing evanescence across the layers, and the global matrix is not yet defined to behave well in this case.

To address this issue, the goal would be to implement the matrix partitioning shown in Fig. 2-2 over a wider range of frequencies ω , wavenumbers s , and orders ν . Thus, the key would be to re-consider the representation I chose for the displacement potentials in Eqs. (2.13-2.15). In particular, I would re-consider

my use of the “normalizing” Hankel functions $H_\nu^{(1)}(h_{rn}R_{n-1})$, $H_\nu^{(1)}(h_{rn}R_n)$, $H_\nu^{(1)}(k_{rn}R_{n-1})$, and $H_\nu^{(1)}(k_{rn}R_n)$. I chose these normalizing functions to satisfy two criteria:

1. To implement the matrix partitioning for large arguments, and
2. To prevent the matrix coefficients from overflowing or underflowing.

I believe that stability could be maintained over a wider range by defining a new set of normalizing functions to satisfy three criteria:

1. To implement the matrix partitioning for large arguments,
2. To implement the matrix partitioning for large orders, and
3. To prevent the matrix coefficients from overflowing or underflowing.

To learn from a solution to a similar problem, we can refer to the paper by Schmidt that documents his DGM solution for spherically layered systems [40]. In that paper, Schmidt implemented matrix partitioning for large orders by normalizing his spherical Bessel functions with the asymptotic forms of spherical Bessel functions. A similar approach would succeed for the cylindrically layered problem, as long we make sure that we also address matrix partitioning for large arguments at the same time.

6.2.2 Numerical Accuracy

Numerical accuracy is especially important if the DGM results are to be taken as “benchmark” or “reference” solutions. I have two reasons to believe that the accuracy is good:

- The DGM shell model and the thin shell models appear to agree well.
- I modeled a fluid-loaded shell by subdividing the shell into two and three layers of identical solid material. I drew contour maps of the response of the shell in

the wavenumber domain, using Pekeris branch cuts, and I saw no evidence of spurious branch cuts that might arise from the wavenumbers for the compression and shear waves in the solid. This means that the branch cuts computed for the solid layers are cancelling each other properly, so that in the final output of the program, we only get the branch cuts due to the fluid loading.

However, I have also observed some evidence of inaccuracy. I computed contour maps of the response of a 3-layered shell with external fluid loading, where the middle layer of the shell was a viscoelastic material. I drew contour maps of the response in the wavenumber domain, using Pekeris branch cuts, and I saw subtle discontinuities in the response that corresponded to branch cuts from the wavenumbers for the compression and shear waves in the solid. These discontinuities are incorrect, both physically and mathematically, because the solutions must be analytic functions of wavenumber, except for poles and the branch cuts due to the external fluid loading.

It is not clear whether this inaccuracy is confined to the region of the wavenumber domain around the Pekeris branch cuts (where the response is computed in terms of I_ν and K_ν), or whether the inaccuracy might also extend to the path of integration from wavenumber to space (where the response can be computed in terms of $H_\nu^{(1)}$ and J_ν). To explain this inaccuracy, I suspect the accuracy of the Bessel functions. To analyze what might be happening, I have considered the role of the Bessel functions in the DGM method:

- In the left-hand side of the DGM equations, the Bessel functions need only have relative accuracy. By this, I mean that the role of the Bessel functions in the global matrix is to provide a pair of linearly independent basis functions that behave as solutions of Bessel's equation. The basis functions can have incorrect magnitude and phase relative to the normalization that mathematicians have given them, as long as the basis functions travel across the layers as solutions to Bessel's equation.

- In the right-hand side of the DGM equations, the Bessel functions must have absolute accuracy. By this, I mean that if the Bessel functions are off by some magnitude and phase, then the solutions will be off by that magnitude and phase.

6.2.3 Numerical Efficiency

The DGM method used here is a relatively efficient implementation of the full 3D equations of elastodynamics. Compared to the use of propagator matrices [31] [32] [33], the DGM method has these advantages: 1) The DGM method handles evanescence across layers without special numerical treatment, 2) The DGM method does not require the multiplication of propagator matrices, and 3) The global matrix can be diagonalized once and then used to solve for the response to different excitations. A more detailed comparison of DGM to propagator matrices is presented by Jensen et al [41]. However, the numerical efficiency of my code could be improved. Here are some suggestions:

- When synthesizing over integer orders, the Bessel functions could be computed more efficiently by taking better advantage of their recurrence relations. Consider that $H_\nu^{(1)}$ is stable for upward recurrence, and J_ν is stable for downward recurrence. Presently, I take advantage of upward recurrence for $H_\nu^{(1)}$, but I don't take advantage of downward recurrence for J_ν . Also, I wonder whether the DGM coefficients themselves could have stable recurrence relations? If so, then the multiplications that define the matrix coefficients could be avoided. Schmidt showed that this was possible for spherically layered systems [40].
- The global matrix is presently stored in a square matrix in Fortran, and the Gaussian elimination is done by a LINPACK routine. This allowed me to get the program working quickly. However, the global matrix is composed of rectangular submatrices, so that many matrix entries are known to be zeros. A more elegant implementation would only need to store and operate on the rectangu-

lar submatricies within the global matrix. Henrik Schmidt's programs SAFARI and OASES address this issue by using banded matrix storage and a banded equation solver.

- Adaptive integration might use the wavenumber samples more effectively.
- The code could be run in parallel on separate computers, particularly for synthesizing over frequencies or wavenumbers.

6.3 Other Applications

One other significant application of the DGM method is the borehole problem in geoaoustics, where we seek to determine the wavespeeds of a rock formation [37] [38]. Elsewhere, I have shown that the DGM method is numerically stable for the physical parameters involved in such a problem. The next step is to add appropriate sources and receivers to the DGM method. Also, by using the DGM model as a Green's function generator, we could model the presence of the logging tool, the effects due to partial debonding of the casing, and the effects due to step changes in the formation properties at a given depth.

Another significant application of the DGM method is ultrasonic non-destructive testing (NDT). Elsewhere, I have shown that the DGM method works at these frequencies. The numerical stability of the method may have to be improved above order 100. The stability issues involved are understood and outlined above in Section 6.2.1.

Appendicies

This page is blank.

Appendix A

Particular Solutions for Time-Harmonic Ring Forces

This appendix derives the particular solutions for time-harmonic ring forces in an unbounded medium. For clarity, this appendix omits the subscript for the layer number.

To prepare for this derivation, I develop a compact notation for writing the transform of the Navier equations in the wavenumber domain. First, I define the axial wavenumber transform of the vector displacement field $\mathbf{u}(r, \theta, z, t)$:

$$\hat{\mathbf{u}}(r, \theta, s, t) \equiv \frac{1}{2\pi} \int_{-\infty}^{\infty} (\mathbf{a}_r u_r + \mathbf{a}_\theta u_\theta + \mathbf{a}_z u_z) e^{-isz} dz = \mathbf{a}_r \hat{u}_r + \mathbf{a}_\theta \hat{u}_\theta + \mathbf{a}_z \hat{u}_z$$

This quantity $\hat{\mathbf{u}}$ may seem abstract and strange, because \mathbf{a}_r , \mathbf{a}_θ , and \mathbf{a}_z are directions in the spatial domain, while \hat{u}_r , \hat{u}_θ , and \hat{u}_z are quantities in the wavenumber domain. So, I avoid interpreting $\hat{\mathbf{u}}$ physically, and I simply regard it as a compact notation for writing \hat{u}_r , \hat{u}_θ , and \hat{u}_z with one symbol.

Next, I define the operators $\hat{\nabla}$, $\hat{\nabla} \cdot$, and $\hat{\nabla} \times$ to be the same as ∇ , $\nabla \cdot$, and $\nabla \times$, except that the operation $\partial/\partial z$ is replaced by the factor is . Using this notation, I

can write the transform of $\nabla \cdot \mathbf{u}$ directly as:

$$\hat{\nabla} \cdot \hat{\mathbf{u}} = \frac{\hat{u}_r}{r} + \frac{\partial \hat{u}_r}{\partial r} + \frac{1}{r} \frac{\partial \hat{u}_\theta}{\partial \theta} + is\hat{u}_z$$

And, from this, I can write the transform of $\nabla(\nabla \cdot \mathbf{u})$ as:

$$\begin{aligned} \hat{\nabla}(\hat{\nabla} \cdot \hat{\mathbf{u}}) &= \mathbf{a}_r \frac{\partial}{\partial r} \left(\frac{\hat{u}_r}{r} + \frac{\partial \hat{u}_r}{\partial r} + \frac{1}{r} \frac{\partial \hat{u}_\theta}{\partial \theta} + is\hat{u}_z \right) \\ &+ \mathbf{a}_\theta \frac{1}{r} \frac{\partial}{\partial \theta} \left(\frac{\hat{u}_r}{r} + \frac{\partial \hat{u}_r}{\partial r} + \frac{1}{r} \frac{\partial \hat{u}_\theta}{\partial \theta} + is\hat{u}_z \right) \\ &+ \mathbf{a}_z is \left(\frac{\hat{u}_r}{r} + \frac{\partial \hat{u}_r}{\partial r} + \frac{1}{r} \frac{\partial \hat{u}_\theta}{\partial \theta} + is\hat{u}_z \right) \end{aligned}$$

Similarly, I can write the transform of $\nabla \times \mathbf{u}$ as:

$$\hat{\nabla} \times \hat{\mathbf{u}} = \mathbf{a}_r \left(\frac{1}{r} \frac{\partial \hat{u}_z}{\partial \theta} - is\hat{u}_\theta \right) + \mathbf{a}_\theta \left(is\hat{u}_r - \frac{\partial \hat{u}_z}{\partial r} \right) + \mathbf{a}_z \left(\frac{\hat{u}_\theta}{r} + \frac{\partial \hat{u}_\theta}{\partial r} - \frac{1}{r} \frac{\partial \hat{u}_r}{\partial \theta} \right)$$

and from this, I can write the transform of $\nabla \times \nabla \times \mathbf{u}$ as:

$$\begin{aligned} \hat{\nabla} \times \hat{\nabla} \times \hat{\mathbf{u}} &= \mathbf{a}_r \left[\frac{1}{r} \frac{\partial}{\partial \theta} \left(\frac{\hat{u}_\theta}{r} + \frac{\partial \hat{u}_\theta}{\partial r} - \frac{1}{r} \frac{\partial \hat{u}_r}{\partial \theta} \right) - is \left(is\hat{u}_r - \frac{\partial \hat{u}_z}{\partial r} \right) \right] \\ &+ \mathbf{a}_\theta \left[is \left(\frac{1}{r} \frac{\partial \hat{u}_z}{\partial \theta} - is\hat{u}_\theta \right) - \frac{\partial}{\partial r} \left(\frac{\hat{u}_\theta}{r} + \frac{\partial \hat{u}_\theta}{\partial r} - \frac{1}{r} \frac{\partial \hat{u}_r}{\partial \theta} \right) \right] \\ &+ \mathbf{a}_z \left[\frac{1}{r} \left(is\hat{u}_r - \frac{\partial \hat{u}_z}{\partial r} \right) + \frac{\partial}{\partial r} \left(is\hat{u}_r - \frac{\partial \hat{u}_z}{\partial r} \right) - \frac{1}{r} \frac{\partial}{\partial \theta} \left(\frac{1}{r} \frac{\partial \hat{u}_z}{\partial \theta} - is\hat{u}_\theta \right) \right] \end{aligned}$$

My derivations will also use displacement potentials to describe the solution away from the ring sources. In such a source-free region, we can always describe a time-harmonic solution \mathbf{u} in terms of displacement potentials that satisfy the homogeneous Helmholtz equations:

$$\mathbf{u} = \nabla\phi + \nabla \times (\mathbf{a}_z\psi) + k^{-1} \nabla \times \nabla \times (\mathbf{a}_z\chi) \quad r \neq r'$$

where r' is the radius of a ring force. The factor k^{-1} is not necessary, but we use it here so the expressions here will be similar to the expressions for the homogeneous

waves associated with the global matrix. Expanding this expression and considering its wavenumber transform, we have:

$$\hat{\mathbf{u}} = \mathbf{a}_r \left(\frac{\partial \hat{\phi}}{\partial r} + \frac{1}{r} \frac{\partial \hat{\psi}}{\partial \theta} + \frac{is}{k} \frac{\partial \hat{\chi}}{\partial r} \right) + \mathbf{a}_\theta \left(\frac{1}{r} \frac{\partial \hat{\phi}}{\partial \theta} - \frac{\partial \hat{\psi}}{\partial r} + \frac{is}{kr} \frac{\partial \hat{\chi}}{\partial \theta} \right) + \mathbf{a}_z \left(is \hat{\phi} + \frac{k_r^2}{k} \hat{\chi} \right) \quad r \neq r'$$

A.1 Radial Ring Forcing

We define a time-harmonic ring force pushing in the radial direction to be:

$$\mathbf{f}(r, \theta, z, t) = F_r \mathbf{a}_r \delta(r - r') e^{i\nu\theta} \delta(z) e^{-i\omega t} \quad (\text{A.1})$$

where F_r is the force per length around the ring, r' is the radius of the ring, and ν is the circumferential order. Applying this force to the Navier equations, we can write:

$$\rho c_p^2 \nabla (\nabla \cdot \mathbf{u}) - \rho c_s^2 \nabla \times \nabla \times \mathbf{u} + \rho \omega^2 \mathbf{u} = -F_r \mathbf{a}_r \delta(r - r') e^{i\nu\theta} \delta(z) e^{-i\omega t}$$

Next, we let the factors $e^{i\nu\theta}$ and $e^{-i\omega t}$ be implied (to simplify the notation that follows), and we apply the wavenumber transform (to allow the solution). Thus, the resulting governing equation is:

$$\rho c_p^2 \hat{\nabla} (\hat{\nabla} \cdot \hat{\mathbf{u}}) - \rho c_s^2 \hat{\nabla} \times \hat{\nabla} \times \hat{\mathbf{u}} + \rho \omega^2 \hat{\mathbf{u}} = -\frac{F_r}{2\pi} \mathbf{a}_r \delta(r - r') \quad (\text{A.2})$$

We solve this system by assuming six unknown potentials:

$$\begin{aligned} \hat{\mathbf{u}} &= \hat{\nabla} \hat{\phi}_I + \hat{\nabla} \times (\mathbf{a}_z \hat{\psi}_I) + k^{-1} \hat{\nabla} \times \hat{\nabla} \times (\mathbf{a}_z \hat{\chi}_I) & 0 \leq r < r' \\ &= \hat{\nabla} \hat{\phi}_E + \hat{\nabla} \times (\mathbf{a}_z \hat{\psi}_E) + k^{-1} \hat{\nabla} \times \hat{\nabla} \times (\mathbf{a}_z \hat{\chi}_E) & r' < r < \infty \end{aligned}$$

where the subscripts I and E denote the interior and exterior regions. In the wavenumber domain, the interior potentials depend on r as Bessel functions of the first kind (to be finite at $r = 0$), and the exterior potentials depend on r as Hankel functions of the first kind (to satisfy radiation conditions). We need six equations

to constrain how these potentials fit together at $r = r'$. Assuming continuity of the displacement field gives us three equations:

$$\lim_{\varepsilon \rightarrow 0} [\hat{u}_r]_{r'+\varepsilon} = \lim_{\varepsilon \rightarrow 0} [\hat{u}_r]_{r'-\varepsilon} \quad \lim_{\varepsilon \rightarrow 0} [\hat{u}_\theta]_{r'+\varepsilon} = \lim_{\varepsilon \rightarrow 0} [\hat{u}_\theta]_{r'-\varepsilon} \quad \lim_{\varepsilon \rightarrow 0} [\hat{u}_z]_{r'+\varepsilon} = \lim_{\varepsilon \rightarrow 0} [\hat{u}_z]_{r'-\varepsilon}$$

Equation (A.2) gives us the other three equations, as we integrate each of that system's three vector components over a vanishingly small interval of r across $r = r'$. This involves integrating the expressions for $\hat{\nabla}(\hat{\nabla} \cdot \hat{\mathbf{u}})$ and $\hat{\nabla} \times \hat{\nabla} \times \hat{\mathbf{u}}$ derived at the beginning of this appendix. Integrating the \mathbf{a}_θ and \mathbf{a}_z components of Eq. (A.2), we find:

$$\lim_{\varepsilon \rightarrow 0} [\partial \hat{u}_\theta / \partial r]_{r'+\varepsilon} = \lim_{\varepsilon \rightarrow 0} [\partial \hat{u}_\theta / \partial r]_{r'-\varepsilon} \quad \lim_{\varepsilon \rightarrow 0} [\partial \hat{u}_z / \partial r]_{r'+\varepsilon} = \lim_{\varepsilon \rightarrow 0} [\partial \hat{u}_z / \partial r]_{r'-\varepsilon}$$

Integrating the \mathbf{a}_r component, we find:

$$\lim_{\varepsilon \rightarrow 0} [\partial \hat{u}_r / \partial r]_{r'+\varepsilon} - \lim_{\varepsilon \rightarrow 0} [\partial \hat{u}_r / \partial r]_{r'-\varepsilon} = -\frac{F_r}{2\pi\rho c_p^2}$$

Expanding these six equations in terms of the assumed potentials creates much algebra, but much of it is in the form of Wronskians, which simplify. Eventually, we get:

$$\begin{aligned} \hat{\phi}_I &= ir' \frac{F_r}{4\rho\omega^2} \left[\frac{dH_\nu^{(1)}(h_r r)}{dr} \right]_{r'} J_\nu(h_r r) \\ \hat{\phi}_E &= ir' \frac{F_r}{4\rho\omega^2} \left[\frac{dJ_\nu(h_r r)}{dr} \right]_{r'} H_\nu^{(1)}(h_r r) \\ \hat{\psi}_I &= \frac{\nu k^2}{k_r^2} \frac{F_r}{4\rho\omega^2} H_\nu^{(1)}(k_r r') J_\nu(k_r r) \\ \hat{\psi}_E &= \frac{\nu k^2}{k_r^2} \frac{F_r}{4\rho\omega^2} J_\nu(k_r r') H_\nu^{(1)}(k_r r) \\ \hat{\chi}_I &= \frac{skr'}{k_r^2} \frac{F_r}{4\rho\omega^2} \left[\frac{dH_\nu^{(1)}(k_r r)}{dr} \right]_{r'} J_\nu(k_r r) \\ \hat{\chi}_E &= \frac{skr'}{k_r^2} \frac{F_r}{4\rho\omega^2} \left[\frac{dJ_\nu(k_r r)}{dr} \right]_{r'} H_\nu^{(1)}(k_r r) \end{aligned}$$

A.2 Circumferential Ring Forcing

We define a time-harmonic ring force pushing in the circumferential direction to be:

$$\mathbf{f}(r, \theta, z, t) = F_\theta \mathbf{a}_\theta \delta(r - r') e^{i\nu\theta} \delta(z) e^{-i\omega t} \quad (\text{A.3})$$

where F_θ is the force per length around the ring. Applying this force to the Navier equations, we can write:

$$\rho c_p^2 \nabla(\nabla \cdot \mathbf{u}) - \rho c_s^2 \nabla \times \nabla \times \mathbf{u} + \rho \omega^2 \mathbf{u} = -F_\theta \mathbf{a}_\theta \delta(r - r') e^{i\nu\theta} \delta(z) e^{-i\omega t}$$

Next, letting $e^{i\nu\theta}$ and $e^{-i\omega t}$ be implied, and applying the wavenumber transform, we have the governing equation:

$$\rho c_p^2 \hat{\nabla}(\hat{\nabla} \cdot \hat{\mathbf{u}}) - \rho c_s^2 \hat{\nabla} \times \hat{\nabla} \times \hat{\mathbf{u}} + \rho \omega^2 \hat{\mathbf{u}} = -\frac{F_\theta}{2\pi} \mathbf{a}_\theta \delta(r - r') \quad (\text{A.4})$$

As before, we assume that $\hat{\mathbf{u}}$ can be represented with six unknown potentials that depend on r as Bessel functions and Hankel functions. We need six equations to constrain how these potentials must fit together at $r = r'$. The continuity of the displacement field gives us three, and the other three come from integrating Eq. (A.4) over a vanishingly small interval of r across $r = r'$. Integrating the \mathbf{a}_r and \mathbf{a}_z components across $r = r'$, we find:

$$\lim_{\epsilon \rightarrow 0} [\partial \hat{u}_r / \partial r]_{r'+\epsilon} = \lim_{\epsilon \rightarrow 0} [\partial \hat{u}_r / \partial r]_{r'-\epsilon} \quad \lim_{\epsilon \rightarrow 0} [\partial \hat{u}_z / \partial r]_{r'+\epsilon} = \lim_{\epsilon \rightarrow 0} [\partial \hat{u}_z / \partial r]_{r'-\epsilon}$$

Integrating the \mathbf{a}_θ component, we find:

$$\lim_{\epsilon \rightarrow 0} [\partial \hat{u}_\theta / \partial r]_{r'+\epsilon} - \lim_{\epsilon \rightarrow 0} [\partial \hat{u}_\theta / \partial r]_{r'-\epsilon} = -\frac{F_\theta}{2\pi \rho c_s^2}$$

Expanding these equations in terms of the assumed potentials, we get:

$$\hat{\phi}_I = \nu \frac{F_\theta}{4\rho\omega^2} H_\nu^{(1)}(h_r r') J_\nu(h_r r)$$

$$\begin{aligned}
\hat{\phi}_E &= \nu \frac{F_\theta}{4\rho\omega^2} J_\nu(h_r r') H_\nu^{(1)}(h_r r) \\
\hat{\psi}_I &= -\frac{i r' k^2}{k_r^2} \frac{F_\theta}{4\rho\omega^2} \left[\frac{dH_\nu^{(1)}(k_r r)}{dr} \right]_{r'} J_\nu(k_r r) \\
\hat{\psi}_E &= -\frac{i r' k^2}{k_r^2} \frac{F_\theta}{4\rho\omega^2} \left[\frac{dJ_\nu(k_r r)}{dr} \right]_{r'} H_\nu^{(1)}(k_r r) \\
\hat{\chi}_I &= -\frac{i\nu s k}{k_r^2} \frac{F_\theta}{4\rho\omega^2} H_\nu^{(1)}(k_r r') J_\nu(k_r r) \\
\hat{\chi}_E &= -\frac{i\nu s k}{k_r^2} \frac{F_\theta}{4\rho\omega^2} J_\nu(k_r r') H_\nu^{(1)}(k_r r)
\end{aligned}$$

A.3 Axial Ring Forcing

We define a time-harmonic ring force pushing in the axial direction to be:

$$\mathbf{f}(r, \theta, z, t) = F_z \mathbf{a}_z \delta(r - r') e^{i\nu\theta} \delta(z) e^{-i\omega t} \quad (\text{A.5})$$

where F_z is the force per length around the ring. Applying this force to the Navier equations, we have:

$$\rho c_p^2 \nabla(\nabla \cdot \mathbf{u}) - \rho c_s^2 \nabla \times \nabla \times \mathbf{u} + \rho \omega^2 \mathbf{u} = -F_z \mathbf{a}_z \delta(r - r') e^{i\nu\theta} \delta(z) e^{-i\omega t}$$

Letting $e^{i\nu\theta}$ and $e^{-i\omega t}$ be implied, and applying the wavenumber transform, the governing equation is:

$$\rho c_p^2 \hat{\nabla}(\hat{\nabla} \cdot \hat{\mathbf{u}}) - \rho c_s^2 \hat{\nabla} \times \hat{\nabla} \times \hat{\mathbf{u}} + \rho \omega^2 \hat{\mathbf{u}} = -\frac{F_z}{2\pi} \mathbf{a}_z \delta(r - r') \quad (\text{A.6})$$

As before, we assume that $\hat{\mathbf{u}}$ can be represented with six potentials, and we need six equations to constrain how the potentials fit together at $r = r'$. The continuity of the displacement field gives us three, the other three come from integrating Eq. (A.6). Integrating the \mathbf{a}_r and \mathbf{a}_θ components across $r = r'$, we find:

$$\lim_{\varepsilon \rightarrow 0} [\partial \hat{u}_r / \partial r]_{r'+\varepsilon} = \lim_{\varepsilon \rightarrow 0} [\partial \hat{u}_r / \partial r]_{r'-\varepsilon} \quad \lim_{\varepsilon \rightarrow 0} [\partial \hat{u}_\theta / \partial r]_{r'+\varepsilon} = \lim_{\varepsilon \rightarrow 0} [\partial \hat{u}_\theta / \partial r]_{r'-\varepsilon}$$

Integrating the \mathbf{a}_z component, we find:

$$\lim_{\varepsilon \rightarrow 0} [\partial \hat{u}_z / \partial r]_{r'+\varepsilon} - \lim_{\varepsilon \rightarrow 0} [\partial \hat{u}_z / \partial r]_{r'-\varepsilon} = -\frac{F_z}{2\pi \rho c_s^2}$$

Expanding these equations in terms of the potentials, we get $\hat{\psi}_I = \hat{\psi}_E = 0$ and:

$$\begin{aligned}\hat{\phi}_I &= sr' \frac{F_z}{4\rho\omega^2} H_\nu^{(1)}(h_r r') J_\nu(h_r r) \\ \hat{\phi}_E &= sr' \frac{F_z}{4\rho\omega^2} J_\nu(h_r r') H_\nu^{(1)}(h_r r) \\ \hat{\chi}_I &= ikr' \frac{F_z}{4\rho\omega^2} H_\nu^{(1)}(k_r r') J_\nu(k_r r) \\ \hat{\chi}_E &= ikr' \frac{F_z}{4\rho\omega^2} J_\nu(k_r r') H_\nu^{(1)}(k_r r)\end{aligned}$$

A.4 Wronskians

This section presents the Wronskians that were essential in simplifying the algebra of the derivations above. Using the properties of the Wronskian of two Hankel functions, I derived the following formulas:

$$\begin{aligned}\left(\frac{dH_\nu^{(1)}(h_r r)}{dr}\right) J_\nu(h_r r) - \left(\frac{dJ_\nu(h_r r)}{dr}\right) H_\nu^{(1)}(h_r r) &= \frac{2i}{\pi r} \\ \left(\frac{dH_\nu^{(1)}(k_r r)}{dr}\right) J_\nu(k_r r) - \left(\frac{dJ_\nu(k_r r)}{dr}\right) H_\nu^{(1)}(k_r r) &= \frac{2i}{\pi r} \\ \left(\frac{d^2 H_\nu^{(1)}(h_r r)}{dr^2}\right) \left(\frac{dJ_\nu(h_r r)}{dr}\right) - \left(\frac{d^2 J_\nu(h_r r)}{dr^2}\right) \left(\frac{dH_\nu^{(1)}(h_r r)}{dr}\right) &= \frac{2i}{\pi r} \left(h_r^2 - \frac{\nu^2}{r^2}\right) \\ \left(\frac{d^2 H_\nu^{(1)}(k_r r)}{dr^2}\right) \left(\frac{dJ_\nu(k_r r)}{dr}\right) - \left(\frac{d^2 J_\nu(k_r r)}{dr^2}\right) \left(\frac{dH_\nu^{(1)}(k_r r)}{dr}\right) &= \frac{2i}{\pi r} \left(k_r^2 - \frac{\nu^2}{r^2}\right)\end{aligned}$$

These formulas are presented here for future reference. They may be important hints if someone wants to derive the particular solutions for the time-harmonic force excitation of a solid in some other coordinate system.

This page is blank.

Appendix B

Suppressing Wrap-Around

This appendix shows how contour offset in the complex wavenumber plane suppresses wrap-around in the spatial domain. The arguments developed here can also be applied to the use of complex frequencies, where contour offset in the complex frequency plane suppresses wrap-around in the time domain.

B.1 Definitions of Transforms

In the body of my thesis, I use axial wavenumber transform pairs of the form:

$$f(z) = \int_{-\infty}^{\infty} \hat{f}(s)e^{isz} ds \iff \hat{f}(s) = \frac{1}{2\pi} \int_{-\infty}^{\infty} f(z)e^{-isz} dz \quad (\text{B.1})$$

where z is the axial coordinate, and s is the axial wavenumber, which can be complex by Cauchy's integral theorem. However, in this appendix, it is also useful to define transform pairs of the form:

$$f(z) = \int_{-\infty}^{\infty} \hat{f}(s_r)e^{is_r z} ds_r \iff \hat{f}(s_r) = \frac{1}{2\pi} \int_{-\infty}^{\infty} f(z)e^{-is_r z} dz \quad (\text{B.2})$$

where s_r is restricted to be real. This allows the use of Dirac deltas in space $\delta(z)$ and wavenumber $\delta(s_r)$, where z and s_r are real.

Equations (B.1) and (B.2) appear identical, but they differ in how their integrals are defined. For example, they differ in how they handle integrands that don't decay at infinity. Consider a travelling wave e^{ikz} , where k is real, and the wave goes from $z = 0$ to infinity. To evaluate the transform $\int_0^\infty e^{ikz} e^{-isz} dz$ with Eq. (B.1), we could let s be complex to make the integral converge, and then we could let s approach the real axis. To evaluate the transform $\int_0^\infty e^{ikz} e^{-is_r z} dz$ with Eq. (B.2), we could convolve $\delta(s_r - k)$ with the transform of the unit step function, where the unit step function is the integral of a Dirac delta. Both approaches give the same result, but their logic is different. These distinctions are discussed more by Champeney [69], who points out that there is no single Fourier theorem; instead, the subject involves many variations on a common theme.

This discussion may appear arcane, but it properly introduces the practical result that a train of Dirac deltas spaced apart by Δ_s in real wavenumber s_r transforms to a train of Dirac deltas spaced apart by $2\pi/\Delta_s$ in space:

$$\frac{2\pi}{\Delta_s} \sum_{m=-\infty}^{\infty} \delta(z - 2\pi m/\Delta_s) \iff \sum_{n=-\infty}^{\infty} \delta(s_r - n\Delta_s) \quad (\text{B.3})$$

where m and n are integers. This relationship is a useful tool for demonstrating the effect that sampling in one domain leads to periodicity in the other domain.

B.2 Wrap-Around

Suppose we have a function of complex wavenumber $\hat{f}(s)$, and we want to compute values of the corresponding function in space, $f(z)$. To do this, suppose we evaluate the wavenumber integral in Eq. (B.1) numerically by sampling $\hat{f}(s)$ along the real s -axis and interpolating it with constant rectangular functions having a width Δ_s .

To study the result of this, let's define a function $\hat{f}_s(s_r)$:

$$\hat{f}_s(s_r) = \hat{f}(s_r)\Delta_s \sum_{n=-\infty}^{\infty} \delta(s_r - n\Delta_s)$$

By substituting $\hat{f}_s(s_r)$ into the integral over wavenumber in Eq. (B.2), $\hat{f}_s(s_r)$ will act like values of $\hat{f}(n\Delta_s)$ held constant over each interval of width Δ_s . Considering Eq. (B.3), $\hat{f}_s(s_r)$ transforms to be:

$$f_s(z) = \sum_{m=-\infty}^{\infty} f(z - 2\pi m/\Delta_s)$$

This equation demonstrates the problem of wrap-around. The trouble is most severe if the physically correct solution $f(z)$ contains waves that travel in the z -direction with no attenuation. Looking at the trouble in the spatial domain, waves from virtual sources at $z = 2\pi m/\Delta_s$ wrap around without attenuation into any interval of z where we try to observe the solution. If we try to make the numerical integration more accurate by decreasing the sample spacing Δ_s , then the virtual sources will move farther apart, but the wrapped-around waves will still enter any interval of z because they travel without attenuation. Or, looking at the trouble in the complex wavenumber domain, the poles corresponding to these waves lie exactly on the real axis, and no matter how small we make Δ_s , the numerical summation will never converge on the correct analytical integral (because the correct analytical integral for Eq. (B.1) avoids passing directly “through” the pole).

The section below will show how contour offset will solve this problem by reformulating the numerical solution to involve transforms of better-behaved functions.

B.3 Contour Offset

We can integrate from wavenumber to space using Eq. (B.1) with contour offset in the complex s -plane. This is allowed by Cauchy's integral theorem. For purposes of

demonstration in this appendix, I use the contours C_1 , C_2 , and C_3 , shown below in Fig. B-1. Offsetting the contour in the direction shown is appropriate for use with my implied time factor of $e^{-i\omega t}$. To write the integrals over these contours, let ϵ be the offset from the real s axis, and let s_r be real, and we can write:

$$I_1(z) = \int_{C_1} \hat{f}(s)e^{isz} ds = \int_{-\infty}^0 \hat{f}(s_r + i\epsilon)e^{i(s_r+i\epsilon)z} ds_r \quad (\text{B.4})$$

$$I_2(z) = \int_{C_2} \hat{f}(s)e^{isz} ds = \int_{i\epsilon}^{-i\epsilon} \hat{f}(s)e^{isz} ds \quad (\text{B.5})$$

$$I_3(z) = \int_{C_3} \hat{f}(s)e^{isz} ds = \int_0^{\infty} \hat{f}(s_r - i\epsilon)e^{i(s_r-i\epsilon)z} ds_r \quad (\text{B.6})$$

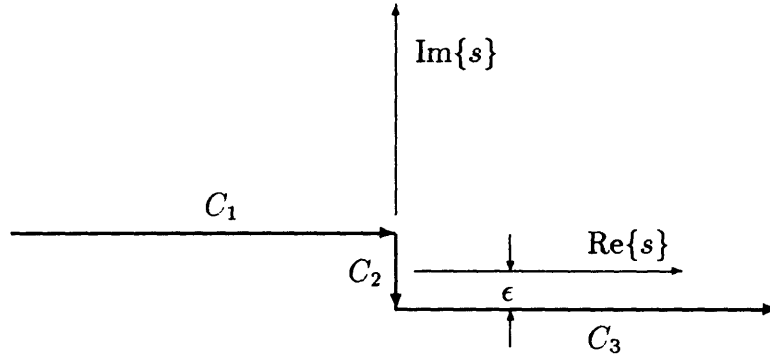


Figure B-1: Contour offset in the wavenumber plane.

Suppose that ϵ can be chosen small enough so that $f(z) \approx I_1(z) + I_3(z)$ for any given value of z of interest. Let's write $I_1(z) + I_3(z)$ in terms of one real variable of integration. First, we re-write Eqs. (B.4) and (B.6) as:

$$\begin{aligned} I_1(z) &= e^{-\epsilon z} \int_0^{\infty} \hat{f}(-s_r + i\epsilon)[\cos(s_r z) - i \sin(s_r z)] ds_r \\ I_3(z) &= e^{\epsilon z} \int_0^{\infty} \hat{f}(s_r - i\epsilon)[\cos(s_r z) + i \sin(s_r z)] ds_r \end{aligned}$$

Next, to show what follows, it will be helpful to define an even function $\hat{g}_e(s_r)$ and an odd function $\hat{g}_o(s_r)$ which are assigned the values $\hat{g}_e(s_r) = \hat{g}_o(s_r) = \hat{f}(s_r - i\epsilon)$ for $s_r > 0$, and $\hat{g}_e(s_r) = \hat{g}_e(-s_r)$ and $\hat{g}_o(s_r) = -\hat{g}_o(-s_r)$. Note that $\hat{g}_e(s_r)$ and $\hat{g}_o(s_r)$ are both non-zero for $s_r < 0$ whether $\hat{f}(s)$ is symmetric about $s = 0$ or not.

Now, if $\hat{f}(s)$ is symmetric about $s = 0$, then $\hat{f}(-s_r + i\epsilon) = \hat{f}(s_r - i\epsilon)$, and:

$$\begin{aligned}
I_1 + I_3 &= (e^{\epsilon z} + e^{-\epsilon z}) \int_0^\infty \hat{f}(s_r - i\epsilon) \cos(s_r z) ds_r + (e^{\epsilon z} - e^{-\epsilon z}) \int_0^\infty \hat{f}(s_r - i\epsilon) i \sin(s_r z) ds_r \\
&= \cosh(\epsilon z) \int_{-\infty}^\infty \hat{g}_e(s_r) \cos(s_r z) ds_r + \sinh(\epsilon z) \int_{-\infty}^\infty \hat{g}_o(s_r) i \sin(s_r z) ds_r \\
&= \cosh(\epsilon z) \int_{-\infty}^\infty \hat{g}_e(s_r) e^{i s_r z} ds_r + \sinh(\epsilon z) \int_{-\infty}^\infty \hat{g}_o(s_r) e^{i s_r z} ds_r \\
&= \cosh(\epsilon z) g_e(z) + \sinh(\epsilon z) g_o(z)
\end{aligned} \tag{B.7}$$

Or, if $\hat{f}(s)$ is antisymmetric about $s = 0$, then $\hat{f}(-s_r + i\epsilon) = -\hat{f}(s_r - i\epsilon)$, and:

$$\begin{aligned}
I_1 + I_3 &= (e^{\epsilon z} - e^{-\epsilon z}) \int_0^\infty \hat{f}(s_r - i\epsilon) \cos(s_r z) ds_r + (e^{\epsilon z} + e^{-\epsilon z}) \int_0^\infty \hat{f}(s_r - i\epsilon) i \sin(s_r z) ds_r \\
&= \sinh(\epsilon z) \int_{-\infty}^\infty \hat{g}_e(s_r) \cos(s_r z) ds_r + \cosh(\epsilon z) \int_{-\infty}^\infty \hat{g}_o(s_r) i \sin(s_r z) ds_r \\
&= \sinh(\epsilon z) \int_{-\infty}^\infty \hat{g}_e(s_r) e^{i s_r z} ds_r + \cosh(\epsilon z) \int_{-\infty}^\infty \hat{g}_o(s_r) e^{i s_r z} ds_r \\
&= \sinh(\epsilon z) g_e(z) + \cosh(\epsilon z) g_o(z)
\end{aligned} \tag{B.8}$$

Equations (B.7) and (B.8) show how contour offset reduces aliasing. We have reformulated the transformation in terms of Fourier transform pairs that are better behaved. Looking in the wavenumber domain, $\hat{g}_e(s_r)$ and $\hat{g}_o(s_r)$ do not have singularities on their axes of wavenumber integration. Or, looking in the spatial domain, the exponential growth of $\cosh(\epsilon z)$ and $\sinh(\epsilon z)$ for large $\pm z$ means that the integrals in Eqs. (B.7) and (B.8) decay at least as fast as exponentials for large $\pm z$ (because $\sinh(\epsilon z)$ and $\cosh(\epsilon z)$ grow with z , while the function $f(z)$ we are computing at most stays constant in magnitude for a trapped wave). Thus, if we evaluate the integrals in Eqs. (B.7) and (B.8) numerically, then the resulting functions of z will have wrap-around, of course, but the exponential decay makes the amplitude of the wrap-around small. In this thesis, I specify 60 dB of attenuation at the folding points $z = \pm\pi/\Delta_s$, by considering $20 \log_{10}(e^{\epsilon\pi/\Delta_s}) = 60$, so $e^{\epsilon\pi/\Delta_s} = 1000$, so:

$$\epsilon = \frac{\ln(1000)}{\pi} \Delta_s \approx 2.20 \Delta_s \tag{B.9}$$

To see all of this graphically, suppose that a source at $z = 0$ is causing waves to travel away from $z = 0$. Let's consider the worst case that the physically correct solution $f(z)$ does not decay, as shown below in Fig. B-2:

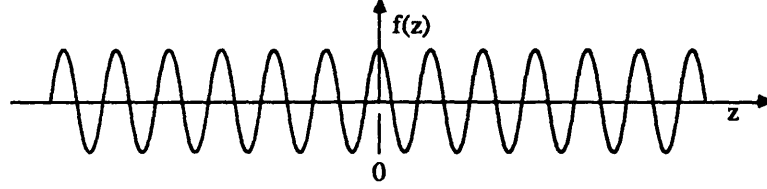


Figure B-2: Physically correct solution $f(z)$ caused by a source at $z = 0$.

Next, suppose we compute the functions $g_e(z)$ and $g_o(z)$ by numerical integration of Eqs. (B.7) and (B.8), using a sample spacing of Δ_s in wavenumber. The computed solutions for $g_e(z)$ and $g_o(z)$ will have wrap-around in space, with a period $2\pi/\Delta_s$, as shown in Fig. B-3. However, these functions will decay exponentially:

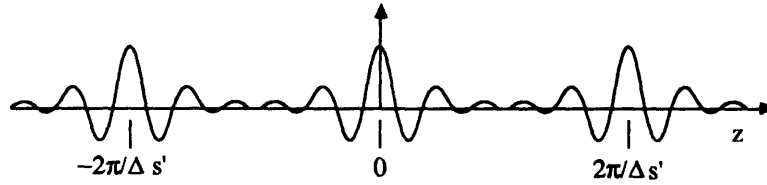


Figure B-3: Computed solution for $g_e(z)$.

Finally, when we apply the factors of $\sinh(\epsilon z)$ and $\cosh(\epsilon z)$ to complete our calculation of $I_1(z) + I_3(z)$, we get a solution that is accurate over the interval $-\pi/\Delta_s < z < \pi/\Delta_s$, as shown in Fig. B-4. The computed solution grows exponentially for $|z| > \pi/\Delta_s$.

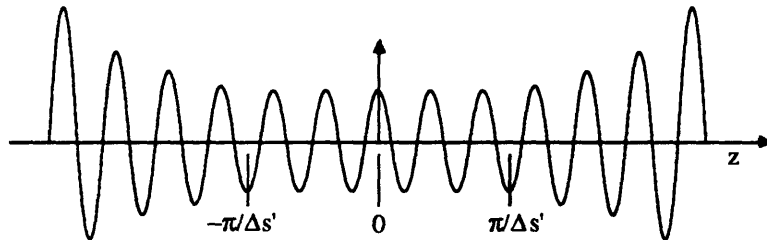


Figure B-4: Computed solution for $f(z)$.

Appendix C

Elastodynamic Response to a Time-Harmonic Point Force

This appendix considers an elastic solid filling all of space, and the elastic solid is excited by a time-harmonic point force. The response is derived here directly in the spatial domain, using del operator notation (∇). This derivation gives us a check against the numerical results of the DGM model, which synthesizes the response to a point force by integrating over axial wavenumbers and summing over circumferential orders. This appendix confirms that the real part of the drive point displacement is infinite, while the imaginary part is finite.

The notation in this appendix is slightly different than the notation in the body of the thesis, because we have no need for the layer number n , and we will use spherical coordinates. Let the solid have a compressional wavespeed c_c with a wavenumber $h = \omega/c_c$, and a shear wavespeed c_s with a wavenumber $k = \omega/c_s$. The density of the solid is ρ . To excite the solid with a time-harmonic point force, we can write the 3D equations of elastodynamics as:

$$\rho c_c^2 \nabla(\nabla \cdot \mathbf{u}) - \rho c_s^2 \nabla \times \nabla \times \mathbf{u} + \rho \omega^2 \mathbf{u} = -F_o \mathbf{a} \delta(\mathbf{r}) \quad (\text{C.1})$$

where F_o is the magnitude of the force, \mathbf{a} is the direction of the force, $\delta(\mathbf{r})$ is a 3D Dirac delta, and a factor of $e^{-i\omega t}$ is implied.

This equation is solved elegantly in the the book *Seismic Waves and Sources* by Ben-Menahem and Singh [45]. They write their solution in the form:

$$\mathbf{u} = F_o [\nabla\nabla \cdot (\mathbf{a}S_c) - \nabla \times \nabla \times (\mathbf{a}S_s)] \quad (\text{C.2})$$

where S_c and S_s involve compression and shear waves:

$$S_c = \frac{1}{4\pi\rho\omega^2} \left(\frac{1 - e^{\pm ik|\mathbf{r}|}}{|\mathbf{r}|} \right) \quad S_s = \frac{1}{4\pi\rho\omega^2} \left(\frac{1 - e^{\pm ik|\mathbf{r}|}}{|\mathbf{r}|} \right) \quad (\text{C.3})$$

and $|\mathbf{r}|$ is the distance from the point force. To satisfy the radiation conditions with our time factor of $e^{-i\omega t}$, we choose the positive signs for the exponentials.

A subtle point that must be noted here is that the vector field \mathbf{a} in Eqs. (C.2) and (C.3) is a Cartesian vector field. In other words, the vectors in the field \mathbf{a} are parallel to each other everywhere in space. This fact is not stated explicitly by Ben-Menahem and Singh, but it does enter into their solution in the form of a vector identity they use. As this fact affects this appendix, note that the functions $\nabla \cdot (\mathbf{a}S_c)$ and $\nabla \times (\mathbf{a}S_s)$ would become different functions if we were to mistakenly change \mathbf{a} from a Cartesian direction vector field to, say, the radial direction vector field in spherical coordinates.

Knowing this, we are now ready to expand Eq. (C.2) correctly. To be most elegant, let's introduce a polar coordinate system centered at the location of the point force. Let the north pole of the system point in the direction of the force. Let r be the radius, let ϑ be the angle down from the pole, and let φ be the angle around the equator. These are the spherical coordinates used by Morse and Feshbach in their table of del operations [51]. Using these terms, we can write the Cartesian direction vector \mathbf{a} correctly in terms of spherical coordinates:

$$\mathbf{a} = \mathbf{a}_r \cos \vartheta - \mathbf{a}_\vartheta \sin \vartheta$$

From this, we can begin to expand Eq. (C.2):

$$\begin{aligned}\mathbf{a}S_c &= \mathbf{a}_r \cos \vartheta S_c - \mathbf{a}_\vartheta \sin \vartheta S_c \\ \mathbf{a}S_s &= \mathbf{a}_r \cos \vartheta S_s - \mathbf{a}_\vartheta \sin \vartheta S_s\end{aligned}$$

Next, note that $\nabla \cdot (\mathbf{a}S_c)$ acts as a displacement potential for compression waves, and $\nabla \times (\mathbf{a}S_s)$ acts as a displacement potential for shear waves. These expressions evaluate to be rather simple, due to the spherical symmetry of S_c and S_s :

$$\nabla \cdot (\mathbf{a}S_c) = \cos \vartheta \frac{\partial S_c}{\partial r} \quad \nabla \times (\mathbf{a}S_s) = -\mathbf{a}_\varphi \sin \vartheta \frac{\partial S_s}{\partial r}$$

From this, the displacements are:

$$\begin{aligned}\frac{u_r(r, \vartheta, \varphi)}{F_o} &= \cos \vartheta \left(\frac{\partial^2 S_c}{\partial r^2} + \frac{2}{r} \frac{\partial S_s}{\partial r} \right) \\ \frac{u_\vartheta(r, \vartheta, \varphi)}{F_o} &= -\sin \vartheta \left(\frac{1}{r} \frac{\partial S_c}{\partial r} + \frac{1}{r} \frac{\partial S_s}{\partial r} + \frac{\partial^2 S_s}{\partial r^2} \right) \\ \frac{u_\varphi(r, \vartheta, \varphi)}{F_o} &= 0\end{aligned}$$

These results make sense, considering the axisymmetry of the excitation. The displacements do not depend on the angle around the equator, φ . The displacement in the circumferential direction u_φ is zero everywhere. And, if $\vartheta \rightarrow 0$, then $u_\vartheta \rightarrow 0$ because of the factor of $\sin \vartheta$.

Finally, to find the displacement in the direction of the force, we can evaluate the radial displacement u_r along the polar axis of the coordinate system by setting $\vartheta = 0$:

$$\frac{u_r(r, 0, \varphi)}{F_o} = \frac{1}{4\pi\rho\omega^2} \left[\frac{(h^2 r^2 + 2ihr - 2)e^{ihr} + (-2ikr + 2)e^{ikr}}{r^3} \right] \quad (\text{C.4})$$

Let's study the real and imaginary parts of Eq. (C.4) separately. Expanding $e^{ihr} = \cos hr + i \sin hr$ and $e^{ikr} = \cos kr + i \sin kr$, and assuming h and k to be real,

we find the imaginary part is:

$$\text{Im} \left\{ \frac{u_r(r, 0, \varphi)}{F_o} \right\} = \frac{1}{4\pi\rho\omega^2} \left[\frac{(h^2r^2 - 2) \sin hr + 2hr \cos hr - 2kr \cos kr + 2 \sin kr}{r^3} \right]$$

As $r \rightarrow 0$, the numerator and denominator of this expression both go to zero as r^3 .

Applying L'Hôpital's rule to this expression three times, we get a finite value:

$$\lim_{r \rightarrow 0} \text{Im} \left\{ \frac{u_r(r, 0, \varphi)}{F_o} \right\} = \frac{h^3 + 2k^3}{12\pi\rho\omega^2}$$

To interpret this result, let F_o be real to provide a phase reference, and we can compute the time-averaged input power $\langle \Pi \rangle$ as 1/2 times the peak force F_o times the velocity in phase with the force:

$$\langle \Pi \rangle = \frac{F_o}{2} \omega \lim_{r \rightarrow 0} \text{Im} \{u_r(r, 0, \varphi)\} = \frac{F_o^2(h^3 + 2k^3)}{24\pi\rho\omega} = \frac{F_o^2\omega^2(c_c^{-3} + 2c_s^{-3})}{24\pi\rho}$$

Thus, the time-averaged power flow injected into the system is finite and positive. This is good, because finite and positive power flow is essential to be consistent with radiation away from the point force.

However, the real part of Eq. (C.4) is not as well-behaved:

$$\text{Re} \left\{ \frac{u_r(r, 0, \varphi)}{F_o} \right\} = \frac{1}{4\pi\rho\omega^2} \left[\frac{(h^2r^2 - 2) \cos hr - 2hr \sin hr + 2 \cos kr + 2kr \sin kr}{r^3} \right]$$

As $r \rightarrow 0$, the numerator of this expression goes to zero as r^2 while the denominator goes to zero as r^3 . Thus, as $r \rightarrow 0$, this expression goes to infinity. Physically, this means an infinite amount of energy is stored and released every cycle in a near-field energy storage mechanism concentrated locally in a tiny volume around the point of application (considering a finite force acting through an infinite displacement). Also, this makes the drive point impedance zero or undefined (considering a finite force divided by an infinite displacement). These artifacts can be avoided by applying forces with some small distribution of stress, rather than a Dirac delta.

Appendix D

Branch Cut Implementation

Our computer programs allow the user the option of choosing either EJP or Pekeris branch cuts in the s -plane, as shown in Figs. D-1 and D-2. This appendix presents the mathematics and computer programming involved.

Physically, the branch cuts arise because a solution at a point in the s -plane assumes an axial dependence of e^{isz} , and this axial dependence can be associated with waves in the outermost layer that travel out to $r = \infty$ or travel in from $r = \infty$. Mathematically, this ambiguity arises in Eqs. (2.8-2.12), which define h_{rn}^2 and k_{rn}^2 without defining h_{rn} and k_{rn} explicitly. The radial wavenumbers h_{rn} and k_{rn} are defined as the square roots of h_{rn}^2 and k_{rn}^2 respectively, and the square root is a double-valued function. Therefore, all quantities considered in the wavenumber domain after Eqs. (2.8-2.12) might be considered to be double-valued functions as well.

This ambiguity must be removed. This is done by thinking of each double-valued function as two single-valued functions lying on top of each other. The single-valued functions are known as Riemann sheets. For example, see the stereoscopic drawings of Riemann sheets shown by Morse and Feshbach [51]. We will remove the ambiguity by cutting these two Riemann sheets apart and throwing one away. But which values will we keep, and where will we do the cutting?

These questions can be answered mathematically and physically. Mathematically, to make the integral transform from wavenumber to space converge, the solutions must be chosen to allow convergence along the path of integration ($-\infty < s < \infty$) in Eq. (2.6). For any response variable (e.g., displacement or stress), one Riemann sheet contains values that decay exponentially for large s , and the other Riemann sheet contains values that grow exponentially. The essential point is to keep the values that decay along the path of integration ($-\infty < s < \infty$). As long as we do that, then we can cut the sheets apart anywhere we like. Physically, choosing the solutions that decay with large s corresponds to satisfying a radiation condition for large r . Thus, the convergent integral corresponds to a synthesis of waves that radiate and decay away from the shell.

D.1 EJP Branch Cuts

One approach is to apply the radiation condition everywhere in the s -plane. This is done simply by defining the radial wavenumbers to satisfy $\text{Im}\{h_{rn}\} \geq 0$ and $\text{Im}\{k_{rn}\} \geq 0$. This gives the EJP branch cuts [70], shown in Fig. D-1.

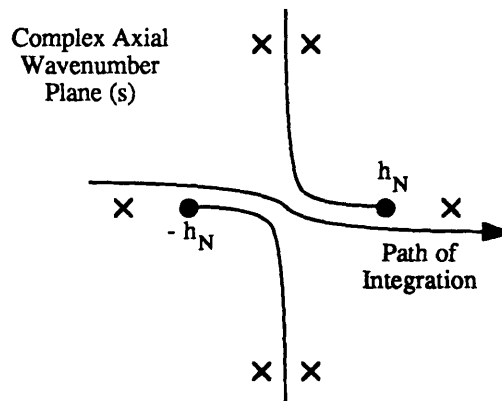


Figure D-1: The EJP branch cuts are hyperbolas that pass through the branch points $s = \pm h_N$. The branch points can be moved off the real s -axis by adding damping to layer N or by making the frequency ω complex. Some typical poles are marked here with an “x.”

EJP branch cuts are very simple to implement. Consider the Fortran intrinsic function `SQRT(X)` that computes the square root of any complex number X . Our Fortran compilers return values that satisfy $\text{Re}\{\text{SQRT}(X)\} \geq 0$. Knowing this, we compute the radial wavenumbers as:

$$h_{rn} = i \text{SQRT}(s^2 - h_n^2) \quad (\text{D.1})$$

$$k_{rn} = i \text{SQRT}(s^2 - k_n^2) \quad (\text{D.2})$$

Clearly, the factor of i in these expressions gives us $\text{Im}\{h_{rn}\} \geq 0$ and $\text{Im}\{k_{rn}\} \geq 0$. And, squaring both sides of Eqs. (D.1) and (D.2), we recover $h_{rn}^2 = h_n^2 - s^2$ and $k_{rn}^2 = k_n^2 - s^2$, which is correct per Eqs. (2.11) and (2.12). Thus, the EJP branch cuts are implemented simply by implementing Eqs. (D.1) and (D.2).

D.2 Pekeris Branch Cuts

The EJP branch cuts in Fig. D-1 do not show the poles for the leaky modes, and the leaky modes can be associated with observable waves. Therefore, we also implement Pekeris branch cuts, as shown in Fig. D-2.

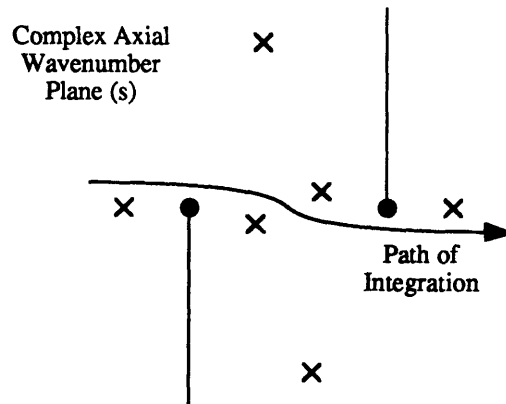


Figure D-2: The Pekeris branch cuts are straight lines up and down in the s -plane from the the branch points $s = \pm h_N$. Note that the integral along the path shown is unchanged.

Pekeris branch cuts are more complicated to implement. First, we implement:

$$h_{rn} = \text{SQRT}(h_n^2 - s^2) \quad |\text{Re}\{s\}| \leq \text{Re}\{k_n\} \quad (\text{D.3})$$

$$= i \text{SQRT}(s^2 - h_n^2) \quad |\text{Re}\{s\}| > \text{Re}\{k_n\} \quad (\text{D.4})$$

with similar expressions for k_{rn} , where $\text{Re}\{\text{SQRT}(X)\} \geq 0$ by definition. These expressions define h_{rn} and k_{rn} to be analytic everywhere in the s -plane except for the Pekeris branch cuts.

Next, we might consider substituting $x = h_{rn}r$ and $x = k_{rn}r$ into $H_\nu^{(1)}(x)$ and $J_\nu(x)$, but this generates values of x that cross the negative real x -axis, where the branch cuts for $H_\nu^{(1)}(x)$ and $J_\nu(x)$ are, and this would cause unwanted discontinuities to appear in the solutions in the s -plane. To avoid this problem, note that:

$$H_\nu^{(1)}(x) = -(2i/\pi)e^{-i\nu\pi/2}K_\nu(-ix) \quad (\text{D.5})$$

$$J_\nu(x) = e^{i\nu\pi/2}I_\nu(-ix) \quad (\text{D.6})$$

for $-\pi/2 < \arg x \leq \pi$, where I_ν and K_ν are modified Bessel functions [52]. The expressions on the right-hand sides of Eqs. (D.5) and (D.6) act like $H_\nu^{(1)}(x)$ and $J_\nu(x)$, but their branch cuts are rotated to run down the negative imaginary x -axis. Thus, these expressions are analytic for all values of $h_{rn}r$ and $k_{rn}r$ generated by Eqs. (D.3) and (D.4). We substitute the expressions of Eqs. (D.5) and (D.6) wherever $H_\nu^{(1)}(x)$ and $J_\nu(x)$ were used in the implementation of the global matrix method. Computed this way, all solutions are analytic everywhere in the s -plane except for the poles and the Pekeris branch cuts.

Appendix E

Admittance Matrix for a Thin Elastic Plate

This appendix organizes some well-known arguments about the mechanics of plates so I can define and compute a 5×5 admittance matrix for a thin circular plate excited by resultant forces and moments along its outer edge. The plate is shown in Fig. E-1.

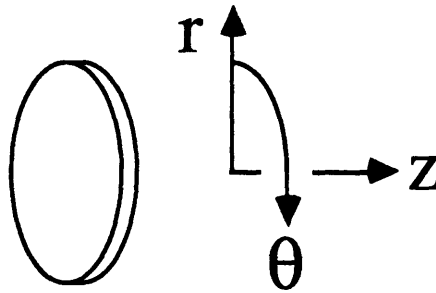


Figure E-1: A thin circular plate.

To define the plate, let the plate be attached to the shell at $z = 0$. Let the outer radius of the plate be R_p , which is the inner radius of the DGM shell model. Let the thickness of the plate be T_p , let the density be ρ_p , let the Young's modulus be E_p , let the Poisson ratio be ν_p , and let the shear modulus be $G_p = E_p/[2(1 - \nu_p)]$.

Also, I let the displacements of the plate be U_{rp} , $U_{\theta p}$, and U_{zp} . I use the upper case letter U for the displacements in thin plate theories to distinguish them from “exact” elastodynamic displacements u .

E.1 Symmetric Inplane Motions

The resultants F_r and F_θ excite inplane motions in the plate that are symmetric with respect to $z = 0$. In this case, $U_{rp} = U_{rp}(r, \theta)$, $U_{\theta p} = U_{\theta p}(r, \theta)$, and $U_{zp} = 0$.

To derive appropriate equations of motion, I review the equations of elasticity in cylindrical coordinates for 2D stress-strain fields in the r - θ plane. Derivations of these equations can be found in textbooks by Nash [71] and Wang [72]. Here I add inertial forces to their free-body diagrams so the equations model dynamics, rather than statics.

Considering an infinitesimal element of the plate with no externally applied forces, the shear stresses $\sigma_{r\theta}$ and $\sigma_{\theta r}$ must be equal, and Newton’s second law of motion appears as:

$$\frac{\partial \sigma_{rr}}{\partial r} + \frac{1}{r} \frac{\partial \sigma_{r\theta}}{\partial \theta} + \frac{\sigma_{rr} - \sigma_{\theta\theta}}{r} = \rho_p \ddot{U}_{rp} \quad \frac{1}{r} \frac{\partial \sigma_{\theta\theta}}{\partial \theta} + \frac{\partial \sigma_{r\theta}}{\partial r} + \frac{2\sigma_{r\theta}}{r} = \rho_p \ddot{U}_{\theta p}$$

The strains are related to the displacements by:

$$\epsilon_r = \frac{\partial U_{rp}}{\partial r} \quad \epsilon_\theta = \frac{U_{rp}}{r} + \frac{1}{r} \frac{\partial U_{\theta p}}{\partial \theta} \quad \gamma_{r\theta} = \frac{1}{r} \frac{\partial U_{rp}}{\partial \theta} + \frac{\partial U_{\theta p}}{\partial r} - \frac{U_{\theta p}}{r}$$

and, assuming $\sigma_{zz} = 0$, the stress-strain relationships are:

$$\begin{Bmatrix} \epsilon_r \\ \epsilon_\theta \end{Bmatrix} = \frac{1}{E_p} \begin{bmatrix} 1 & -\nu_p \\ -\nu_p & 1 \end{bmatrix} \begin{Bmatrix} \sigma_{rr} \\ \sigma_{\theta\theta} \end{Bmatrix} \quad \gamma_{r\theta} = \mu_p^{-1} \sigma_{r\theta}$$

Now, to combine these equations for our purposes, I invert the stress-strain relationships to give us the stresses:

$$\begin{Bmatrix} \sigma_{rr} \\ \sigma_{\theta\theta} \end{Bmatrix} = \frac{E_p}{1 - \nu_p^2} \begin{bmatrix} 1 & \nu_p \\ \nu_p & 1 \end{bmatrix} \begin{Bmatrix} \epsilon_r \\ \epsilon_\theta \end{Bmatrix} \quad \sigma_{r\theta} = \mu_p \gamma_{r\theta}$$

and I substitute these expressions for the stresses into the result of Newton's second law shown above. After much algebra (more easily derived in Cartesian coordinates), I can write the 2D equations of motion as:

$$c_{Lp}^2 \nabla \nabla \cdot \mathbf{U}_p(r, \theta) - c_{Sp}^2 \nabla \times \nabla \times \mathbf{U}_p(r, \theta) = \ddot{\mathbf{U}}_p(r, \theta) \quad (\text{E.1})$$

in terms of a 2D displacement vector in the plane of the plate:

$$\mathbf{U}_p(r, \theta) \equiv \mathbf{a}_r U_{rp}(r, \theta) + \mathbf{a}_\theta U_{\theta p}(r, \theta)$$

and these wavespeeds:

$$c_{Lp} \equiv \sqrt{E_p / [\rho_p (1 - \nu_p^2)]} \quad c_{Sp} \equiv \sqrt{\mu_p / \rho_p}$$

where c_{Lp} is the speed of longitudinal waves in the plane of the plate, and c_{Sp} is the speed of shear waves in the plane of the plate. Note how Eq. (E.1) is similar to the full 3D equations of elastodynamics, but the speed of compression waves is different because the stress-strain relations used here implicitly assume $\sigma_{zz}(r, \theta, z) = 0$.

Incidentally, this explains why the speed of compression waves in a plate involves a factor of one minus Poisson's ratio squared. It appears in the derivation above where the stress-strain relations are inverted.

To find the solutions of Eq. (E.1), I recall the vector decomposition techniques used in Chapter 2 for the full elastodynamic equations. I decompose $\mathbf{U}_p(r, \theta)$ into

longitudinal and transverse parts as:

$$\mathbf{U}_p(r, \theta) = \nabla \phi_p(r, \theta) + \nabla \times (\mathbf{a}_z \psi_p(r, \theta)) \quad (\text{E.2})$$

where $\phi_p(r, \theta)$ and $\psi_p(r, \theta)$ are 2D displacement potentials. Next, I assume an implied time factor of $e^{-i\omega t}$. Then, by applying $\nabla \cdot$ to both sides of Eq. (E.2), I find $\nabla^2 \phi_p + h_p^2 \phi_p = 0$, where $h_p \equiv \omega/c_{Lp}$ is the wavenumber for inplane compression waves in the plate. Similarly, by applying $\nabla \times$ to both sides of Eq. (E.2), I find $\nabla^2 \psi_p + k_p^2 \psi_p = 0$, where $k_p \equiv \omega/c_{Sp}$ is the wavenumber for inplane shear waves in the plate. Next, assuming an angular dependence of $e^{i\nu\theta}$, I can expand these Helmholtz equations as:

$$\frac{d^2 \phi_p}{dr^2} + \frac{1}{r} \frac{d\phi_p}{dr} + \left(h_p^2 - \frac{\nu^2}{r^2} \right) \phi_p = 0 \quad \frac{d^2 \psi_p}{dr^2} + \frac{1}{r} \frac{d\psi_p}{dr} + \left(k_p^2 - \frac{\nu^2}{r^2} \right) \psi_p = 0$$

The equation for ϕ_p is solved by any linear combination of $J_\nu(h_p r)$ and $Y_\nu(h_p r)$, and the equation for ψ_p is solved by any linear combination of $J_\nu(k_p r)$ and $Y_\nu(k_p r)$. I discard $Y_\nu(h_p r)$ and $Y_\nu(k_p r)$ because they go to infinity as $r \rightarrow 0$, so finally I have:

$$\phi_p \propto J_\nu(h_p r) \quad \psi_p \propto J_\nu(k_p r)$$

Now, to find the response of the plate to inplane ring forces, I consider:

$$U_{rp} = \frac{d\phi_p}{dr} + \frac{i\nu}{r} \psi_p \quad U_{\theta p} = \frac{i\nu}{r} \phi_p - \frac{d\psi_p}{dr} \quad (\text{E.3})$$

and I expand σ_{rr} and $\sigma_{r\theta}$ in terms of these expressions, until I have:

$$\begin{bmatrix} \nu^2 - h_p^2 r^2 / (1 - \nu_p) & -1 & -i\nu & i\nu \\ -2i\nu & 2i\nu & k_p^2 r^2 - 2\nu^2 & 2 \\ r dJ_\nu(h_p r)/dr & -J_\nu(h_p r) & 0 & 0 \\ 0 & 0 & r dJ_\nu(k_p r)/dr & -J_\nu(k_p r) \end{bmatrix} \begin{Bmatrix} r^{-2} \phi_p \\ r^{-1} d\phi_p/dr \\ r^{-2} \psi_p \\ r^{-1} d\psi_p/dr \end{Bmatrix}$$

$$= \begin{Bmatrix} [(1 + \nu_p)/E_p] \sigma_{rr} \\ (1/\mu_p) \sigma_{r\theta} \\ 0 \\ 0 \end{Bmatrix} \quad (\text{E.4})$$

Eqs. (E.3) and (E.4) give us the drive response of a circular plate to a radial ring force at its outer edge if I substitute $r = R_p$, $\sigma_{rr}(R_p, \theta) = (F_r/T_p)e^{i(\nu\theta - \omega t)}$, and $\sigma_{r\theta}(R_p, \theta) = 0$, where F_r is the magnitude of the ring force in the positive r -direction, having units of force per length around the circumference of the ring. I solve Eq. (E.4) by Gaussian elimination, and I compute the drive displacements $U_{rp}(R_p, \theta)$ and $U_{\theta p}(R_p, \theta)$ in terms of the solution vector. Similarly, Eqs. (E.3) and (E.4) give us the drive response of the plate to a circumferential ring force if I substitute $r = R_p$, $\sigma_{rr}(R_p, \theta) = 0$, and $\sigma_{r\theta}(R_p, \theta) = (F_\theta/T_p)e^{i(\nu\theta - \omega t)}$, where F_θ is the magnitude of the ring force in the positive θ -direction. Again, I solve Eq. (E.4) by Gaussian elimination, and I compute the drive displacements $U_{rp}(R_p, \theta)$ and $U_{\theta p}(R_p, \theta)$ in terms of the solution vector. By default, I normalize the Bessel functions $J_\nu(x)$ in Eq. (E.4) exponentially with respect to their arguments as $J_\nu(x)e^{ix}$. I normalize them as $[\Gamma(\nu)/(x/2)^\nu] J_\nu(x)$ if $|(x/2)^\nu/\Gamma(\nu)| < 0.01$.

E.2 Flexural Motions

The resultants F_z , M_r , and M_θ excite flexural motions. In this thesis, I model these motions with the Mindlin plate theory [67] [64]. I have two motivations for using the Mindlin plate theory rather than the classical plate theory. One motivation is that the Mindlin theory is more accurate, because it accounts for the transverse shear deformations that are effectively set equal to zero in the classical plate theory. The other motivation is my curiosity. I want to look at the 3 resultants in the plate separately (i.e., F_z , M_r , and M_θ). The Mindlin theory accounts for these 3 resultants as 3 distinctly separate effects. In contrast, in the classical theory, the 3 resultants cannot be studied separately. (This fact is illustrated by the fact that a stress-free

edge of a plate is modeled in the classical theory by applying the Kirchhoff edge condition, which relates the twisting moment to the transverse shear force.)

To paraphrase Mindlin's assumptions, a thin flat plate is modeled by approximating the plate's "exact" full 3D elastic displacement field $\mathbf{u} = \{u_r, u_\theta, u_z\}$ with an "approximate" displacement field $\mathbf{U}_p = \{U_{rp}, U_{\theta p}, U_{zp}\}$. The transverse normal stress σ_{zz} is modeled as being zero everywhere, and the transverse displacement $U_{zp}(r, \theta)$ is defined to be independent of z . Assuming that straight fibers across the plate remain straight, the displacements $U_{rp}(r, \theta, z)$ and $U_{\theta p}(r, \theta, z)$ are defined to vary linearly with z , and the extensional strains and stresses are modeled as being proportional to z as well. The bending and twisting moments are modeled as integrals of these linearly varying stresses. However, to calculate the transverse shear forces, Mindlin introduces a factor κ to account for the fact that \mathbf{U}_p only approximates \mathbf{u} . For example, in this thesis, where I use the symbol $F_z(r, \theta)$ to represent the transverse shear force along an arc of constant r , we have:

$$F_z(r, \theta) = G_p \int_{-T_p/2}^{T_p/2} \left(\frac{\partial U_{rp}}{\partial z} + \frac{\partial U_{zp}}{\partial r} \right) dz = \kappa^2 G_p \int_{-T_p/2}^{T_p/2} \left(\frac{\partial U_{rp}}{\partial z} + \frac{\partial U_{zp}}{\partial r} \right) dz$$

Mindlin summarized his results elegantly for time-harmonic vibration in vacuo (i.e., no transverse loading) [67] [64]. In this case, the 3 wave types are governed by:

$$(\nabla^2 + k_1^2)w_1(r, \theta) = 0 \quad (\nabla^2 + k_2^2)w_2(r, \theta) = 0 \quad (\nabla^2 + k_3^2)P(r, \theta) = 0$$

At low frequencies, $w_1(r, \theta)$ is the transverse displacement of a propagating flexural wave, and $w_2(r, \theta)$ is the transverse displacement of an evanescent flexural wave. At high frequencies, $w_1(r, \theta)$ becomes something like a Rayleigh wave, and $w_2(r, \theta)$ becomes a propagating "thickness-shear" wave. These waves add together to give the out-of-plane displacement as:

$$U_{zp}(r, \theta) = w_1(r, \theta) + w_2(r, \theta)$$

Later, I will show how $P(r, \theta)$ is something like a displacement potential for shear displacements in the plane of the plate, where $P(r, \theta)$ will contribute to $U_{rp}(r, \theta, z)$ and $U_{\theta p}(r, \theta, z)$, but not to $U_{zp}(r, \theta)$.

To compute the wavenumbers for these 3 wave types, I first compute the bending stiffness D_c and the flexural wavenumber k_c from the classical theory:

$$D_c \equiv \frac{E_p T_p^3}{12(1 - \nu_p^2)} = \frac{G_p T_p^3}{6(1 - \nu_p)} \quad k_c^4 \equiv \frac{\rho_p T_p \omega^2}{D_c}$$

Next, for the Mindlin theory, I compute the parameters I_p and S_p which are associated with rotatory inertia and shear strains respectively:

$$I_p \equiv \frac{T_p^2}{12} \quad S_p \equiv \frac{D_c}{\kappa^2 G_p T_p}$$

Using these parameters, the wavenumbers are computed as:

$$k_1^2, k_2^2 = \frac{k_c^4}{2} \left[S_p + I_p \pm \sqrt{(S_p - I_p)^2 + \frac{4}{k_c^4}} \right] \quad k_3^2 = \frac{2}{1 - \nu_p} \left[I_p k_c^4 - \frac{1}{S_p} \right]$$

Now I can express the displacements $U_{rp}(r, \theta, z)$ and $U_{\theta p}(r, \theta, z)$:

$$U_{rp}(r, \theta, z) = z \Psi_r(r, \theta) \quad U_{\theta p}(r, \theta, z) = z \Psi_\theta(r, \theta)$$

where $\Psi_r(r, \theta)$ and $\Psi_\theta(r, \theta)$ are Dyer's notation for the rotations of the plate fibers [64]. I use Dyer's notation here so the expressions I write below can be easily checked against Dyer's paper. However, be aware that in this notation, positive Ψ_r represents radial displacements that give a positive rotation about the θ -axis, and positive Ψ_θ represents circumferential displacements that give a negative rotation about the r -axis. Aware of this, we will proceed using Dyer's notation:

$$\begin{aligned} \Psi_r(r, \theta) &= (\alpha_1 - 1) \frac{\partial w_1}{\partial r} + (\alpha_2 - 1) \frac{\partial w_2}{\partial r} + \frac{1}{r} \frac{\partial P}{\partial \theta} \\ \Psi_\theta(r, \theta) &= (\alpha_1 - 1) \frac{1}{r} \frac{\partial w_1}{\partial \theta} + (\alpha_2 - 1) \frac{1}{r} \frac{\partial w_2}{\partial \theta} - \frac{\partial P}{\partial r} \end{aligned}$$

where the parameters α_1 and α_2 are:

$$\alpha_1 = \frac{2k_2^2}{(1 - \nu_p)k_3^2} \quad \alpha_2 = \frac{2k_1^2}{(1 - \nu_p)k_3^2}$$

Note that the classical theory also assumes that the fibers remain straight and rotate, too, but the zero shear strains in that theory constrain the rotations to be $\Psi_r = -\partial U_{zp}/\partial r$ and $\Psi_\theta = -(1/r)\partial U_{zp}/\partial \theta$. The Mindlin theory would recover these relations if we could set $P = 0$ and somehow set $G_p \rightarrow \infty$ in the formula for S_p while holding E_p finite in the formula for D_c . This would set $S_p \rightarrow 0$, so $k_3 \rightarrow i\infty$, which would set $\alpha_1 \rightarrow 0$ and $\alpha_2 \rightarrow 0$. Thus, Dyer interprets the classical theory as assuming an infinite transverse shear modulus [64].

Now I can express the quantities that really interest us, which are F_z , M_r , and M_θ . Recall that I chose my sign convention for the resultants in Fig. 4-3, and my convention for the resultants agrees with the convention used by Dyer [64]. Thus, I can copy the expressions from Dyer's paper, where we see the transverse shear force along an arc of constant r :

$$F_z(r, \theta) = \frac{D_c}{S_p} \left[\Psi_r + \frac{\partial U_{zp}}{\partial r} \right] = \frac{D_c}{S_p} \left[\alpha_1 \frac{\partial w_1}{\partial r} + \alpha_2 \frac{\partial w_2}{\partial r} + \frac{1}{r} \frac{\partial P}{\partial \theta} \right]$$

the twisting moment along an arc of constant r :

$$M_r(r, \theta) = -D_c \frac{1 - \nu_p}{2} \left[\frac{1}{r} \left(\frac{\partial \Psi_r}{\partial \theta} - \Psi_\theta \right) + \frac{\partial \Psi_\theta}{\partial r} \right]$$

and the bending moment along an arc of constant r :

$$M_\theta(r, \theta) = D_c \left[\frac{\partial \Psi_r}{\partial r} + \frac{\nu_p}{r} \left(\Psi_r + \frac{\partial \Psi_\theta}{\partial \theta} \right) \right]$$

Next, to apply these equations to our purposes, I impose an angular dependence of $e^{i\nu\theta}$, which will now be implied, and I write:

$$w_1(r, \theta) \propto J_\nu(k_1 r) \quad w_2(r, \theta) \propto J_\nu(k_2 r) \quad P(r, \theta) \propto J_\nu(k_3 r)$$

From this, I can write:

$$\begin{bmatrix} 0 & \alpha_1 & 0 & \alpha_2 & i\nu & 0 \\ c_{21} & c_{22} & c_{23} & c_{24} & c_{25} & c_{26} \\ c_{31} & c_{32} & c_{33} & c_{34} & c_{35} & c_{36} \\ c_{41} & c_{42} & 0 & 0 & 0 & 0 \\ 0 & 0 & c_{53} & c_{54} & 0 & 0 \\ 0 & 0 & 0 & 0 & c_{65} & c_{66} \end{bmatrix} \begin{bmatrix} w_1/r \\ \partial w_1/\partial r \\ w_2/r \\ \partial w_2/\partial r \\ P/r \\ \partial P/\partial r \end{bmatrix} = \begin{bmatrix} (S_p/D_c) F_z \\ r[D_c(1 - \vartheta_p)]^{-1} M_r \\ r[D_c(1 - \vartheta_p)]^{-1} M_\theta \\ 0 \\ 0 \\ 0 \end{bmatrix} \quad (\text{E.5})$$

where the coefficients for the twisting moment are:

$$\begin{aligned} c_{21} &= i\nu(\alpha_1 - 1) & c_{22} &= -i\nu(\alpha_1 - 1) & c_{23} &= i\nu(\alpha_2 - 1) & c_{24} &= -i\nu(\alpha_2 - 1) \\ c_{25} &= \nu^2 - k_3^2 r^2/2 & c_{26} &= -1 \end{aligned}$$

and the coefficients for the bending moment are:

$$\begin{aligned} c_{31} &= (\alpha_1 - 1)[\nu^2 - k_1^2 r^2/(1 - \vartheta_p)] & c_{32} &= -(\alpha_1 - 1) \\ c_{33} &= (\alpha_2 - 1)[\nu^2 - k_2^2 r^2/(1 - \vartheta_p)] & c_{34} &= -(\alpha_2 - 1) \\ c_{35} &= -i\nu & c_{36} &= i\nu \end{aligned}$$

The remaining coefficients ensure that w_1 , w_2 , and P behave as Bessel functions:

$$\begin{aligned} c_{41} &= r dJ_\nu(k_1 r)/dr & c_{42} &= -J_\nu(k_1 r) & c_{53} &= r dJ_\nu(k_2 r)/dr & c_{54} &= -J_\nu(k_2 r) \\ c_{65} &= r dJ_\nu(k_3 r)/dr & c_{66} &= -J_\nu(k_3 r) \end{aligned}$$

Eq. (E.5) gives us the response of the plate to out-of-plane excitations. I set one entry in the right-hand side to be non-zero, and solve the system by Gaussian elimination. By default, I normalize the Bessel functions $J_\nu(x)$ exponentially with respect to their arguments as $J_\nu(x)e^{ix}$. I normalize them as $[\Gamma(\nu)/(x/2)^\nu] J_\nu(x)$ if $|(x/2)^\nu/\Gamma(\nu)| < 0.01$.

Finally, I should discuss how we might give the parameter κ some appropriate

value. Mindlin's original paper gives one formula that makes the flexural wavespeed approach the wavespeed of Rayleigh waves at high frequencies. This gives Mindlin's flexural waves the correct *ratio* of strain energy to potential energy, but the strain and potential energies themselves are most surely inaccurate, because the the Mindlin theory has the straight fibers remain straight. Thus, this value of κ need not be considered to be the "correct" value, even if we are interested in exciting flexural waves in the plate, because it will probably get the *impedance* of flexural waves wrong! Mindlin also gives another formula ($\kappa = \pi/\sqrt{12} \approx 0.9069$) that predicts the resonance of the "thickness-shear" mode. Again, this value of κ need not be considered to be the "correct" value.

E.3 Symmetry vs. Antisymmetry

Typically, admittance matrices are symmetric when they describe the velocities and rotations of a structure responding to point forces and moments. In such a case, the equality of the terms across the diagonal can be proven by some theorem of dynamic reciprocity.

However, the admittance matrices constructed in this thesis are not necessarily symmetric. This appears to be due to the fact that in this thesis I define the excitations and velocities to be distributed over the circumference with some phase shift in a traveling wave description. This section of this appendix demonstrates a case of antisymmetry caused by this effect.

For this demonstration, I consider the plate to be rigid with some outer radius R_p . I consider any applied forces to have the angular dependence $e^{i\theta}$. Thus, this demonstration considers the order $\nu = 1$ only. I introduce a pair of Cartesian coordinate axes x and y in the plane of the plate, which were introduced in Fig. 5-1. I let F_x and F_y be the net forces applied to the plate in the x and y -directions, respectively. I let V_x and V_y be the rigid body velocity components in the x and y -directions. I assume all quantities have an implied time factor of $e^{-i\omega t}$.

Furthermore, for this demonstration, I let the rigid body velocity components be related to the applied forces according to some impedance Z :

$$V_x = \frac{F_x}{Z} \quad V_y = \frac{F_y}{Z} \quad (\text{E.6})$$

This impedance could be $-i\omega$ times the mass of the plate, if the impedance represents a purely inertial effect. Or, the impedance could include a resistive effect, if we imagine dashpots connected to the plate to resist its motion. My point here is that Z is general enough to represent any resistance or reactance to a rigid body motion.

Now I will calculate Y_{21} , which is the velocity at the outer edge $r = R_p$ in the θ -direction due to a ring force in the r -direction. Let the plate be excited by a radial ring force $F_r e^{i\theta}$, where F_r is the amplitude of the radial ring force in units of force per length around the circumference. In this case, the net forces on the plate are:

$$F_x = \int_{-\pi}^{\pi} F_r e^{i\theta} \cos(\theta) R_p d\theta = \pi F_r R_p \quad F_y = \int_{-\pi}^{\pi} F_r e^{i\theta} \sin(\theta) R_p d\theta = i\pi F_r R_p$$

This forcing induces no rigid body rotations. There is only a rigid body translation:

$$V_x = \frac{\pi F_r R_p}{Z} \quad V_y = \frac{i\pi F_r R_p}{Z}$$

And from V_x and V_y , we know the velocity in the θ -direction:

$$v_\theta(\theta) = -V_x \sin(\theta) + V_y \cos(\theta) = \frac{i\pi F_r R_p}{Z} e^{i\theta}$$

Thus, we have the result:

$$Y_{21} = \frac{i\pi R_p}{Z} \quad (\text{E.7})$$

Now, I will calculate Y_{12} , which is the velocity at the outer edge $r = R_p$ in the r -direction due to a ring force in the θ -direction. Let the plate be excited by a circumferential ring force $F_\theta e^{i\theta}$, where F_θ is the amplitude of the ring force in units of force per length around the circumference. In this case, the net forces on the plate

are:

$$F_x = \int_{-\pi}^{\pi} -F_{\theta} e^{i\theta} \sin(\theta) R_p d\theta = -i\pi F_{\theta} R_p \quad F_y = \int_{-\pi}^{\pi} F_{\theta} e^{i\theta} \cos(\theta) R_p d\theta = \pi F_{\theta} R_p$$

From these forces, the velocities are:

$$V_x = -\frac{i\pi F_{\theta} R_p}{Z} \quad V_y = \frac{\pi F_{\theta} R_p}{Z}$$

And, the velocity in the r -direction is:

$$v_r(\theta) = V_x \cos(\theta) + V_y \sin(\theta) = -\frac{i\pi F_{\theta} R_p}{Z} e^{i\theta}$$

Thus, the admittance Y_{12} is:

$$Y_{12} = -\frac{i\pi R_p}{Z} \tag{E.8}$$

This demonstration shows that, in this case, the entries Y_{21} and Y_{12} are equal in magnitude but opposite in sign.

E.4 Checking Admittances

Finally, I checked the numerically computed values of the admittance matrix entries in the following three ways:

First, I checked the special case of axisymmetric excitations. Setting the order equal to zero, I observe the numerical results $Y_{12} \doteq Y_{21} \doteq 0$, $Y_{34} \doteq Y_{43} \doteq 0$, and $Y_{45} \doteq Y_{54} \doteq 0$. This is what we should get for axisymmetric excitations.

Second, I checked power flow. If the plate is given some material damping, then I observe that all of the on-diagonal entries have positive real parts. This means that any of the 5 resultants will inject positive net power into the plate (when applied individually). Also, if the material damping is set equal to zero, then I observe that all of the on-diagonal entries have numerically vanishing real parts. This means that any

of the 5 resultants will inject no net power into the plate (when applied individually). These results are correct. I haven't thought about reciprocity or power relations that might be derived to constrain the off-diagonal entries.

Third, I checked the rigid body dynamics that are recovered when the frequency is low, so there are no waves across the plate. Let M_p be the total mass of the plate. Considering the rigid body dynamics of a disk of mass M_p , we can expect to see the following as $\omega \rightarrow 0$:

- Rigid body rotation about the z -axis is recovered by setting the order equal to zero. In this case, $-i\omega Y_{22}$ is the translational acceleration in the circumferential direction at the outer edge of the plate due to a circumferential ring force of 1 N/m, so the angular acceleration is $-i\omega Y_{22}/R_p$ due to a net moment of $2\pi R_p^2$. Considering that the rigid body moment of inertia of the plate about the z -axis is $M_p R_p^2/2$, we re-arrange these quantities to find that $Y_{22} \rightarrow 4\pi R_p/(-i\omega M_p)$.
- Rigid body translation in the z -direction is recovered by setting the order equal to zero. In this case, $-i\omega Y_{33}$ is the translational acceleration in the axial direction due to a net axial force of $2\pi R_p \times 1$ N/m. Thus, $Y_{33} \rightarrow 2\pi R_p/(-i\omega M_p)$.
- Rigid body translations in the r and θ -directions are recovered by setting the order equal to one. In this case, I let the rigid body impedance Z be $-i\omega M_p$ in Eq. (E.6). Then, Eq. (E.7) gives us $Y_{21} \rightarrow -\pi R_p/(\omega M_p)$ and Eq. (E.8) gives us $Y_{12} \rightarrow \pi R_p/(\omega M_p)$. Also, one can show that $Y_{11} \rightarrow Y_{22} \rightarrow i\pi R_p/(\omega M_p)$. Thus, as the frequency goes to zero for $\nu = 1$,

$$\begin{bmatrix} Y_{11} & Y_{12} \\ Y_{21} & Y_{22} \end{bmatrix} \rightarrow \frac{\pi R_p i}{\omega M_p} \begin{bmatrix} 1 & -i \\ i & 1 \end{bmatrix} \quad (\text{E.9})$$

- Rigid body rotations about the x and y -axes are recovered by setting the order equal to one. The x and y -axes I'm using are shown in Fig. 5-1. First, let's establish the net moments that can be created by setting the order equal to one. To see how the phase is involved, it will help to write the factor $e^{-i\omega t}$ explicitly:

- ▷ A ring force $F_z e^{i(\theta-\omega t)}$ N/m in the z -direction applies a net moment about the x -axis of $i\pi R_p^2 F_z e^{-i\omega t}$ N-m and a net moment about the y -axis of $-\pi R_p^2 F_z e^{-i\omega t}$ N-m.
- ▷ A ring moment $M_r e^{i(\theta-\omega t)}$ N-m/m about the r -axis applies a net moment about the x -axis of $\pi R_p M_r e^{-i\omega t}$ N-m and a net moment about the y -axis of $i\pi R_p M_r e^{-i\omega t}$ N-m.
- ▷ A ring moment $M_\theta e^{i(\theta-\omega t)}$ N-m/m about the θ -axis applies a net moment about the x -axis of $-i\pi R_p M_\theta e^{-i\omega t}$ N-m and a net moment about the y -axis of $\pi R_p M_\theta e^{-i\omega t}$ N-m.

Next, consider that the rigid body moment of inertia of the plate about the x or y -axis is $M_p R_p^2/4$. Also, consider that if the plate is a rigid body rotating about the point $\{x, y, z\} = \{0, 0, 0\}$, then $\dot{U}_z = -R_p \Omega_\theta$. Finally, considering how the net moments act on the moment of inertia, we can establish:

$$\begin{bmatrix} Y_{33} & Y_{34} & Y_{35} \\ Y_{43} & Y_{44} & Y_{45} \\ Y_{53} & Y_{54} & Y_{55} \end{bmatrix} \rightarrow \frac{4\pi i}{\omega M_p} \begin{bmatrix} R_p & -i & -1 \\ i & 1/R_p & -i/R_p \\ -1 & i/R_p & 1/R_p \end{bmatrix} \quad (\text{E.10})$$

I have confirmed that my numerical implementation of the plate's admittance matrix recovers all of these asymptotic results when I substituted very low numerical values of frequencies (e.g., 10^{-3} and 10^{-6} times the ring frequency of the shell, where the plate and the shell had the same material properties). This is a very satisfying check on the program, considering that the plate's admittance matrix is implemented using much algebra that involves Bessel functions of many different arguments and orders, yet these simple asymptotic results are recovered accurately. Also, the symmetry and antisymmetry within the matrix is notable.

Appendix F

Admittance Matrix for the DGM Shell Model

This appendix develops techniques for defining and computing a 5×5 admittance matrix for the DGM shell model, as the DGM shell model is excited by distributions of stresses from an internally attached plate or stiffener.

F.1 Resultant Forces and Moments

Suppose the DGM shell model is excited by a body force $\mathbf{f}(r, \theta, z)$ concentrated onto the cylindrical surface $r = r'$, and having an angular dependence of $e^{i\nu\theta}$. Concentrating the force onto some surface $r = r'$ means the force can represent the loads applied to the DGM shell model by an internally attached plate or stiffener, and using the factor $e^{i\nu\theta}$ means that the derivations that follow will be valid for a given order ν in a synthesis of orders that solve a scattering problem. I write such a body force as:

$$\mathbf{f}(r, \theta, z) = \delta(r - r')e^{i\nu\theta} [\mathbf{a}_r f_r(z) + \mathbf{a}_\theta f_\theta(z) + \mathbf{a}_z f_z(z)] \quad (\text{F.1})$$

Considering that I will use this body force to attach a plate of thickness T_p , I define the body force to be zero outside of the interval $-T_p/2 \leq z \leq T_p/2$:

$$f_r(z) \equiv f_\theta(z) \equiv f_z(z) \equiv 0 \quad |z| > T_p/2 \quad (\text{F.2})$$

Also, it will be useful to consider these functions in terms of odd and even parts:

$$f_r(z) = c_1 f_{r_o}(z) + c_2 f_{r_e}(z) \quad f_\theta(z) = c_3 f_{\theta_o}(z) + c_4 f_{\theta_e}(z) \quad f_z(z) = c_5 f_{z_o}(z) + c_6 f_{z_e}(z)$$

where the subscripts *o* and *e* mean “odd” and “even” with respect to $z = 0$. I have introduced the complex constants c_1 through c_6 to allow the normalization:

$$\int_{-T_p/2}^{T_p/2} f_{r_e}(z) dz \equiv \int_{-T_p/2}^{T_p/2} f_{\theta_e}(z) dz \equiv \int_{-T_p/2}^{T_p/2} f_{z_e}(z) dz \equiv 1 \quad (\text{F.3})$$

$$\int_{-T_p/2}^{T_p/2} f_{r_o}(z) z dz \equiv \int_{-T_p/2}^{T_p/2} f_{\theta_o}(z) z dz \equiv \int_{-T_p/2}^{T_p/2} f_{z_o}(z) z dz \equiv 1 \quad (\text{F.4})$$

Expressed in these terms, $\mathbf{f}(r, \theta, z)$ causes 3 resultant forces and 2 resultant moments:

$$F_r(\theta) = \int_{-T_p/2}^{T_p/2} c_2 e^{i\nu\theta} f_{r_e}(z) dz = c_2 e^{i\nu\theta} \quad (\text{F.5})$$

$$F_\theta(\theta) = \int_{-T_p/2}^{T_p/2} c_4 e^{i\nu\theta} f_{\theta_e}(z) dz = c_4 e^{i\nu\theta} \quad (\text{F.6})$$

$$F_z(\theta) = \int_{-T_p/2}^{T_p/2} c_6 e^{i\nu\theta} f_{z_e}(z) dz = c_6 e^{i\nu\theta} \quad (\text{F.7})$$

$$M_r(\theta) = - \int_{-T_p/2}^{T_p/2} c_3 e^{i\nu\theta} f_{\theta_o}(z) z dz = -c_3 e^{i\nu\theta} \quad (\text{F.8})$$

$$M_\theta(\theta) = \int_{-T_p/2}^{T_p/2} c_1 e^{i\nu\theta} f_{r_o}(z) z dz = c_1 e^{i\nu\theta} \quad (\text{F.9})$$

Note that I define the moments to be positive when they act about the positive coordinate axes. Also, for future reference, note that the normalizations in Eqs. (F.3) and (F.4) have the consequence that:

$$\text{Im}\{f_{r_e}(z)\} = \text{Im}\{f_{\theta_e}(z)\} = \text{Im}\{f_{z_e}(z)\} = 0$$

$$\text{Im}\{f_{r_o}(z)\} = \text{Im}\{f_{\theta_o}(z)\} = \text{Im}\{f_{z_o}(z)\} = 0$$

Thus, Eqs. (F.5-F.9) give us the complex conjugates of the resultants as:

$$\begin{aligned} F_r^*(\theta) &= [c_2 e^{i\nu\theta}]^* & F_\theta^*(\theta) &= [c_4 e^{i\nu\theta}]^* & F_z^*(\theta) &= [c_6 e^{i\nu\theta}]^* \\ M_r^*(\theta) &= -[c_3 e^{i\nu\theta}]^* & M_\theta^*(\theta) &= [c_1 e^{i\nu\theta}]^* \end{aligned}$$

F.2 Power Transfer

This paragraph develops an expression for the power flow associated with a complex force f acting in the same direction as a complex velocity v . I begin by writing:

$$f e^{-i\omega t} = (f_R + i f_I) e^{-i\omega t} \quad v e^{-i\omega t} = (v_R + i v_I) e^{-i\omega t}$$

where $f_R \equiv \text{Re}\{f\}$, $f_I \equiv \text{Im}\{f\}$, $v_R \equiv \text{Re}\{v\}$, and $v_I \equiv \text{Im}\{v\}$. Next, let's account for the relationship between f and v by supposing that the force acts on a “black box” containing a resistive device (a dashpot) and a reactive device (a mass or a spring). The power transferred to these mechanical devices can be accounted for separately. The peak power transferred to the resistive device is:

$$\begin{aligned} |f||v| \cos(\angle f - \angle v) &= |f||v| [\cos(\angle f) \cos(-\angle v) - \sin(\angle f) \sin(-\angle v)] \\ &= |f||v| \left[\frac{f_R v_R}{|f| |v|} + \frac{f_I v_I}{|f| |v|} \right] \\ &= f_R v_R + f_I v_I = \text{Re}\{f v^*\} \end{aligned} \tag{F.10}$$

Similarly, the peak power transferred to the reactive device is:

$$\begin{aligned} |f||v| \sin(\angle f - \angle v) &= |f||v| [\sin(\angle f) \cos(-\angle v) + \cos(\angle f) \sin(-\angle v)] \\ &= |f||v| \left[\frac{f_I v_R}{|f| |v|} - \frac{f_R v_I}{|f| |v|} \right] \\ &= f_I v_R - f_R v_I = \text{Im}\{f v^*\} \end{aligned} \tag{F.11}$$

Thus, the product $f v^*$ characterizes the power transfer at all instants for a time harmonic complex force $f e^{-i\omega t}$ and velocity $v e^{-i\omega t}$.

To apply this result to the DGM shell model, consider that the body force $\mathbf{f}(r, \theta, z)$ in Eq. (F.1) causes some displacement field, which I write here as:

$$\mathbf{u}(r, \theta, z) = [\mathbf{a}_r u_r(r, z) + \mathbf{a}_\theta u_\theta(r, z) + \mathbf{a}_z u_z(r, z)] e^{i\nu\theta}$$

Thus, I can characterize the power transfer between $\mathbf{f}(r, \theta, z)$ and the DGM shell model in terms of the quantity:

$$\int_{-T_p/2}^{T_p/2} [f_r(z) \dot{u}_r^*(r', z) + f_\theta(z) \dot{u}_\theta^*(r', z) + f_z(z) \dot{u}_z^*(r', z)] |e^{i\nu\theta}|^2 dz \quad (\text{F.12})$$

Note how the factor $|e^{i\nu\theta}|^2$ appears in this last expression, because the factor $e^{i\nu\theta}$ associated with $\mathbf{f}(r, \theta, z)$ is multiplied by the factor $[e^{i\nu\theta}]^*$ associated with $[\mathbf{u}(r, \theta, z)]^*$.

To simplify the expressions that follow, I will now assume ν is real, so $|e^{i\nu\theta}| = 1$. Equation (F.12) can now be accounted for in more detail by decomposing the forces and displacements into parts that are even and odd with respect to $z = 0$:

$$\int_{-T_p/2}^{T_p/2} (c_2 f_{re} \dot{u}_{re}^* + c_4 f_{\theta e} \dot{u}_{\theta e}^* + c_6 f_{ze} \dot{u}_{ze}^*) dz + \int_{-T_p/2}^{T_p/2} (c_1 f_{ro} \dot{u}_{ro}^* + c_3 f_{\theta o} \dot{u}_{\theta o}^* + c_5 f_{zo} \dot{u}_{zo}^*) dz$$

And, the velocities in this expression can be decomposed as:

$$\int_{-T_p/2}^{T_p/2} c_2 f_{re} \dot{u}_{re}^* dz = \int_{-T_p/2}^{T_p/2} c_2 f_{re} ([\dot{u}_{re}]_{c_2 f_{re}}^* + [\dot{u}_{re}]_{c_4 f_{\theta e}}^* + [\dot{u}_{re}]_{c_5 f_{zo}}^*) dz \quad (\text{F.13})$$

$$\int_{-T_p/2}^{T_p/2} c_4 f_{\theta e} \dot{u}_{\theta e}^* dz = \int_{-T_p/2}^{T_p/2} c_4 f_{\theta e} ([\dot{u}_{\theta e}]_{c_2 f_{re}}^* + [\dot{u}_{\theta e}]_{c_4 f_{\theta e}}^* + [\dot{u}_{\theta e}]_{c_5 f_{zo}}^*) dz \quad (\text{F.14})$$

$$\int_{-T_p/2}^{T_p/2} c_6 f_{ze} \dot{u}_{ze}^* dz = \int_{-T_p/2}^{T_p/2} c_6 f_{ze} ([\dot{u}_{ze}]_{c_1 f_{ro}}^* + [\dot{u}_{ze}]_{c_3 f_{\theta o}}^* + [\dot{u}_{ze}]_{c_6 f_{ze}}^*) dz \quad (\text{F.15})$$

$$\int_{-T_p/2}^{T_p/2} c_1 f_{ro} \dot{u}_{ro}^* dz = \int_{-T_p/2}^{T_p/2} c_1 f_{ro} ([\dot{u}_{ro}]_{c_1 f_{ro}}^* + [\dot{u}_{ro}]_{c_3 f_{\theta o}}^* + [\dot{u}_{ro}]_{c_6 f_{ze}}^*) dz \quad (\text{F.16})$$

$$\int_{-T_p/2}^{T_p/2} c_3 f_{\theta o} \dot{u}_{\theta o}^* dz = \int_{-T_p/2}^{T_p/2} c_3 f_{\theta o} ([\dot{u}_{\theta o}]_{c_1 f_{ro}}^* + [\dot{u}_{\theta o}]_{c_3 f_{\theta o}}^* + [\dot{u}_{\theta o}]_{c_6 f_{ze}}^*) dz \quad (\text{F.17})$$

$$\int_{-T_p/2}^{T_p/2} c_5 f_{zo} \dot{u}_{zo}^* dz = \int_{-T_p/2}^{T_p/2} c_5 f_{zo} ([\dot{u}_{zo}]_{c_2 f_{re}}^* + [\dot{u}_{zo}]_{c_4 f_{\theta e}}^* + [\dot{u}_{zo}]_{c_5 f_{zo}}^*) dz \quad (\text{F.18})$$

where $[\dot{u}_{re}]_{c_2 f_{re}}$ means the radial velocity that is even, caused by the forcing function $c_2 f_{re}$, and * means complex conjugate.

Note that the right-hand sides of Eqs. (F.13-F.18) contain 18 combinations of 6 velocity functions due to 6 forcing functions (instead of 36 conceivable combinations). This is correct, because Eqs. (F.13-F.18) implicitly take advantage of the symmetry and antisymmetry of the displacement fields for the different forcing functions. For example, the even radial forcing function f_{re} causes a radial displacement function u_r that is even, so Eq. (F.13) does not involve an odd velocity function $[\dot{u}_{ro}]_{c_2 f_{re}}$, because such a function would be zero.

This paragraph outlines a proof that the 18 velocity functions shown in Eqs. (F.13-F.18) are correct. First, consider ring forcing of the form $\delta(r - r')\delta(z)e^{i\nu\theta}$, as shown in Appendix A, and note the fact that for radial and circumferential ring forcing, \hat{u}_r^P and \hat{u}_θ^P are even in s , while \hat{u}_z^P is odd. For axial ring forcing, \hat{u}_z^P is even, while \hat{u}_r^P and \hat{u}_θ^P are odd. Second, consider that these statements are also true for the homogeneous displacements \hat{u}_r^H , \hat{u}_θ^H , and \hat{u}_z^H that solve multi-layered systems with radiation. Third, consider that functions that are even in s transform to be even in z , while functions that are odd in s transform to be odd in z . Fourth, if we consider convolving the Dirac deltas with even functions in space to form $c_2 f_{re}$, $c_4 f_{\theta e}$, and $c_6 f_{ze}$, then the symmetries and antisymmetries of the displacement functions are unchanged. However, by convolving the Dirac deltas with odd functions to form f_{ro} , $f_{\theta o}$, and f_{zo} , the symmetries and antisymmetries of the displacement functions are exchanged, so that f_{ro} and $f_{\theta o}$ cause u_r and u_θ to be odd, while u_z is even. For f_{zo} , u_r and u_θ are even, while u_z is odd. Thus, the velocities contained in Eqs. (F.13-F.18) are the complete and correct set.

Now I will explicitly set $c_5 f_{zo}(z)$ equal to zero, because it creates no resultant force or moment, and the physical effect of such a force could only be included in a more sophisticated model in the future. The expressions that remain are:

$$\int_{-T_p/2}^{T_p/2} c_2 f_{re} \dot{u}_{re}^* dz = \int_{-T_p/2}^{T_p/2} c_2 f_{re} ([\dot{u}_{re}]_{c_2 f_{re}}^* + [\dot{u}_{re}]_{c_4 f_{\theta e}}^*) dz \quad (\text{F.19})$$

$$\int_{-T_p/2}^{T_p/2} c_4 f_{\theta e} \dot{u}_{\theta e}^* dz = \int_{-T_p/2}^{T_p/2} c_4 f_{\theta e} ([\dot{u}_{\theta e}]_{c_2 f_{re}}^* + [\dot{u}_{\theta e}]_{c_4 f_{\theta e}}^*) dz \quad (\text{F.20})$$

and:

$$\int_{-T_p/2}^{T_p/2} c_6 f_{ze} \dot{u}_{ze}^* dz = \int_{-T_p/2}^{T_p/2} c_6 f_{ze} ([\dot{u}_{ze}]_{c_1 f_{ro}}^* + [\dot{u}_{ze}]_{c_3 f_{\theta o}}^* + [\dot{u}_{ze}]_{c_6 f_{ze}}^*) dz \quad (\text{F.21})$$

$$\int_{-T_p/2}^{T_p/2} c_1 f_{ro} \dot{u}_{ro}^* dz = \int_{-T_p/2}^{T_p/2} c_1 f_{ro} ([\dot{u}_{ro}]_{c_1 f_{ro}}^* + [\dot{u}_{ro}]_{c_3 f_{\theta o}}^* + [\dot{u}_{ro}]_{c_6 f_{ze}}^*) dz \quad (\text{F.22})$$

$$\int_{-T_p/2}^{T_p/2} c_3 f_{\theta o} \dot{u}_{\theta o}^* dz = \int_{-T_p/2}^{T_p/2} c_3 f_{\theta o} ([\dot{u}_{\theta o}]_{c_1 f_{ro}}^* + [\dot{u}_{\theta o}]_{c_3 f_{\theta o}}^* + [\dot{u}_{\theta o}]_{c_6 f_{ze}}^*) dz \quad (\text{F.23})$$

F.3 Defining Admittances

In this section, I introduce a vector of 5 velocities (3 translational and 2 rotational):

$$\mathbf{V} \equiv \{ \dot{U}_r, \dot{U}_\theta, \dot{U}_z, \Omega_r, \Omega_\theta \}$$

I define \dot{U}_r and \dot{U}_θ to depend linearly on F_r and F_θ as:

$$\dot{U}_r \equiv [\dot{U}_r]_{F_r} + [\dot{U}_r]_{F_\theta}$$

$$\dot{U}_\theta \equiv [\dot{U}_\theta]_{F_r} + [\dot{U}_\theta]_{F_\theta}$$

so they account for the integrals in Eqs. (F.19) and (F.20) as:

$$\int_{-T_p/2}^{T_p/2} c_2 f_{re} [\dot{u}_{re}]_{c_2 f_{re}}^* dz = F_r [\dot{U}_r]_{F_r}^* \quad \int_{-T_p/2}^{T_p/2} c_2 f_{re} [\dot{u}_{re}]_{c_4 f_{\theta e}}^* dz = F_r [\dot{U}_r]_{F_\theta}^* \quad (\text{F.24})$$

$$\int_{-T_p/2}^{T_p/2} c_4 f_{\theta e} [\dot{u}_{\theta e}]_{c_2 f_{re}}^* dz = F_\theta [\dot{U}_\theta]_{F_r}^* \quad \int_{-T_p/2}^{T_p/2} c_4 f_{\theta e} [\dot{u}_{\theta e}]_{c_2 f_{\theta e}}^* dz = F_\theta [\dot{U}_\theta]_{F_\theta}^* \quad (\text{F.25})$$

These equations can be re-arranged as:

$$\begin{Bmatrix} \dot{U}_r \\ \dot{U}_\theta \end{Bmatrix} = \begin{bmatrix} Y_{11} & Y_{12} \\ Y_{21} & Y_{22} \end{bmatrix} \begin{Bmatrix} F_r \\ F_\theta \end{Bmatrix}$$

where the entries Y are found by taking the complex conjugates of Eqs. (F.24) and (F.25) (to get \dot{U}_r and \dot{U}_θ), then dividing by F_r or F_θ to get admittances:

$$Y_{11} = \frac{[\dot{U}_r]_{F_r}}{F_r} = \frac{\int_{-T_p/2}^{T_p/2} c_2^* f_{re}^* [\dot{u}_{re}]_{c_2 f_{re}} dz}{F_r F_r^*} \quad Y_{12} = \frac{[\dot{U}_r]_{F_\theta}}{F_\theta} = \frac{\int_{-T_p/2}^{T_p/2} c_2^* f_{re}^* [\dot{u}_{re}]_{c_4 f_{\theta e}} dz}{F_\theta F_r^*}$$

$$Y_{21} = \frac{[\dot{U}_\theta]_{F_r}}{F_r} = \frac{\int_{-T_p/2}^{T_p/2} c_4^* f_{\theta e}^* [\dot{u}_{\theta e}]_{c_2 f_{re}} dz}{F_r F_\theta^*} \quad Y_{22} = \frac{[\dot{U}_\theta]_{F_\theta}}{F_\theta} = \frac{\int_{-T_p/2}^{T_p/2} c_4^* f_{\theta e}^* [\dot{u}_{\theta e}]_{c_4 f_{\theta e}} dz}{F_\theta F_\theta^*}$$

Noting that f_{re} and $f_{\theta e}$ are purely real, this reduces to:

$$Y_{11} \equiv \int_{-T_p/2}^{T_p/2} f_{re} [\dot{u}_{re}]_{f_{re}} dz \quad Y_{12} \equiv \int_{-T_p/2}^{T_p/2} f_{re} [\dot{u}_{re}]_{f_{\theta e}} dz \quad (\text{F.26})$$

$$Y_{21} \equiv \int_{-T_p/2}^{T_p/2} f_{\theta e} [\dot{u}_{\theta e}]_{f_{re}} dz \quad Y_{22} \equiv \int_{-T_p/2}^{T_p/2} f_{\theta e} [\dot{u}_{\theta e}]_{f_{\theta e}} dz \quad (\text{F.27})$$

Similarly, I define the velocities \dot{U}_z , Ω_r , and Ω_θ to depend linearly on the resultants F_z , M_r , and M_θ . Together, they account for the integrals in Eqs. (F.21-F.23) as:

$$\int_{-T_p/2}^{T_p/2} c_6 f_{ze} [\dot{u}_{ze}]_{c_1 f_{ro}}^* dz = F_z [\dot{U}_z]_{M_\theta}^*$$

$$\int_{-T_p/2}^{T_p/2} c_6 f_{ze} [\dot{u}_{ze}]_{c_3 f_{\theta o}}^* dz = F_z [\dot{U}_z]_{M_r}^*$$

$$\int_{-T_p/2}^{T_p/2} c_6 f_{ze} [\dot{u}_{ze}]_{c_6 f_{ze}}^* dz = F_z [\dot{U}_z]_{F_z}^*$$

$$\int_{-T_p/2}^{T_p/2} c_1 f_{ro} [\dot{u}_{ro}]_{c_1 f_{ro}}^* dz = M_\theta [\Omega_\theta]_{M_\theta}^*$$

$$\int_{-T_p/2}^{T_p/2} c_1 f_{ro} [\dot{u}_{ro}]_{c_3 f_{\theta o}}^* dz = M_\theta [\Omega_\theta]_{M_r}^*$$

$$\int_{-T_p/2}^{T_p/2} c_1 f_{ro} [\dot{u}_{ro}]_{c_6 f_{ze}}^* dz = M_\theta [\Omega_\theta]_{F_z}^*$$

$$\int_{-T_p/2}^{T_p/2} c_3 f_{\theta o} [\dot{u}_{\theta o}]_{c_1 f_{ro}}^* dz = M_r [\Omega_r]_{M_\theta}^*$$

$$\int_{-T_p/2}^{T_p/2} c_3 f_{\theta o} [\dot{u}_{\theta o}]_{c_3 f_{\theta o}}^* dz = M_r [\Omega_r]_{M_r}^*$$

$$\int_{-T_p/2}^{T_p/2} c_3 f_{\theta o} [\dot{u}_{\theta o}]_{c_6 f_{ze}}^* dz = M_r [\Omega_r]_{F_z}^*$$

These equations can be re-arranged as:

$$\begin{pmatrix} \dot{U}_z \\ \Omega_r \\ \Omega_\theta \end{pmatrix} = \begin{bmatrix} Y_{33} & Y_{34} & Y_{35} \\ Y_{43} & Y_{44} & Y_{45} \\ Y_{53} & Y_{54} & Y_{55} \end{bmatrix} \begin{pmatrix} F_z \\ M_r \\ M_\theta \end{pmatrix}$$

where the entries Y are found by writing:

$$\begin{aligned} Y_{33} &= \frac{\int_{-T_p/2}^{T_p/2} c_6^* f_{ze}^* [\dot{u}_{ze}]_{c_6 f_{ze}} dz}{F_z F_z^*} \\ Y_{34} &= \frac{\int_{-T_p/2}^{T_p/2} c_6^* f_{ze}^* [\dot{u}_{ze}]_{c_3 f_{\theta o}} dz}{M_r F_z^*} \\ Y_{35} &= \frac{\int_{-T_p/2}^{T_p/2} c_6^* f_{ze}^* [\dot{u}_{ze}]_{c_1 f_{r o}} dz}{M_\theta F_z^*} \\ Y_{43} &= \frac{\int_{-T_p/2}^{T_p/2} c_3^* f_{\theta o}^* [\dot{u}_{\theta o}]_{c_6 f_{ze}} dz}{F_z M_r^*} \\ Y_{44} &= \frac{\int_{-T_p/2}^{T_p/2} c_3^* f_{\theta o}^* [\dot{u}_{\theta o}]_{c_3 f_{\theta o}} dz}{M_r M_r^*} \\ Y_{45} &= \frac{\int_{-T_p/2}^{T_p/2} c_3^* f_{\theta o}^* [\dot{u}_{\theta o}]_{c_1 f_{r o}} dz}{M_\theta M_r^*} \\ Y_{53} &= \frac{\int_{-T_p/2}^{T_p/2} c_1^* f_{r o}^* [\dot{u}_{r o}]_{c_6 f_{ze}} dz}{F_z M_\theta^*} \\ Y_{54} &= \frac{\int_{-T_p/2}^{T_p/2} c_1^* f_{r o}^* [\dot{u}_{r o}]_{c_3 f_{\theta o}} dz}{M_r M_\theta^*} \\ Y_{55} &= \frac{\int_{-T_p/2}^{T_p/2} c_1^* f_{r o}^* [\dot{u}_{r o}]_{c_1 f_{r o}} dz}{M_\theta M_\theta^*} \end{aligned}$$

which reduces to:

$$\begin{aligned} Y_{33} &\equiv \int_{-T_p/2}^{T_p/2} f_{ze} [\dot{u}_{ze}]_{f_{ze}} dz & Y_{34} &\equiv - \int_{-T_p/2}^{T_p/2} f_{ze} [\dot{u}_{ze}]_{f_{\theta o}} dz & Y_{35} &\equiv \int_{-T_p/2}^{T_p/2} f_{ze} [\dot{u}_{ze}]_{f_{r o}} dz \\ Y_{43} &\equiv - \int_{-T_p/2}^{T_p/2} f_{\theta o} [\dot{u}_{\theta o}]_{f_{ze}} dz & Y_{44} &\equiv \int_{-T_p/2}^{T_p/2} f_{\theta o} [\dot{u}_{\theta o}]_{f_{\theta o}} dz & Y_{45} &\equiv - \int_{-T_p/2}^{T_p/2} f_{\theta o} [\dot{u}_{\theta o}]_{f_{r o}} dz \\ Y_{53} &\equiv \int_{-T_p/2}^{T_p/2} f_{r o} [\dot{u}_{r o}]_{f_{ze}} dz & Y_{54} &\equiv - \int_{-T_p/2}^{T_p/2} f_{r o} [\dot{u}_{r o}]_{f_{\theta o}} dz & Y_{55} &\equiv \int_{-T_p/2}^{T_p/2} f_{r o} [\dot{u}_{r o}]_{f_{r o}} dz \end{aligned}$$

To summarize this section, these integrals define a 5×5 admittance matrix that gives the correct instantaneous power transfer due to $\mathbf{f}(r, \theta, z)$ having an implied angular dependence of $e^{i\nu\theta}$:

$$\begin{pmatrix} \dot{U}_r \\ \dot{U}_\theta \\ \dot{U}_z \\ \Omega_r \\ \Omega_\theta \end{pmatrix} = \begin{bmatrix} Y_{11} & Y_{12} & 0 & 0 & 0 \\ Y_{21} & Y_{22} & 0 & 0 & 0 \\ 0 & 0 & Y_{33} & Y_{34} & Y_{35} \\ 0 & 0 & Y_{43} & Y_{44} & Y_{45} \\ 0 & 0 & Y_{53} & Y_{54} & Y_{55} \end{bmatrix} \begin{pmatrix} F_r \\ F_\theta \\ F_z \\ M_r \\ M_\theta \end{pmatrix}$$

with the restrictions that $f_{z0}(z) = 0$, ν is real, and $\mathbf{f}(r, \theta, z) = 0$ for $|z| > T_p/2$.

F.4 Convolution Properties

In this section, I review the transform properties of convolutions. Even though these properties are well-known, I still need to review them here to guarantee that I correctly account for any factors of 2π that arise to be consistent with my definition of the wavenumber transform:

$$f(z) = \int_{-\infty}^{\infty} \hat{f}(s)e^{isz} ds \quad \iff \quad \hat{f}(s) = \frac{1}{2\pi} \int_{-\infty}^{\infty} f(z)e^{-isz} dz$$

Suppose we have a function $f(z) \iff \hat{f}(s)$ and a function $g(z) \iff \hat{g}(s)$, where the transforms are defined by the integrals above. Let's consider the convolution of $f(z)$ and $g(z)$ over space:

$$f(z) \otimes g(z) \equiv \int_{-\infty}^{\infty} f(x)g(z-x) dx$$

where x is a dummy variable of integration. Applying my definition of the wavenum-

ber transform to both sides of this expression, we have:

$$\begin{aligned}
\frac{1}{2\pi} \int_{-\infty}^{\infty} [f(z) \otimes g(z)] e^{-isz} dz &= \frac{1}{2\pi} \int_{-\infty}^{\infty} \left[\int_{-\infty}^{\infty} f(x) g(z-x) dx \right] e^{-isz} dz \\
&= \frac{1}{2\pi} \int_{-\infty}^{\infty} f(x) \left[\int_{-\infty}^{\infty} g(z-x) e^{-isz} dz \right] dx \\
&= \int_{-\infty}^{\infty} f(x) \left[\frac{1}{2\pi} \int_{-\infty}^{\infty} g(z-x) e^{-is(z-x)} dz \right] e^{-isx} dx \\
&= \int_{-\infty}^{\infty} f(x) \hat{g}(s) e^{-isx} dx = 2\pi \hat{f}(s) \hat{g}(s)
\end{aligned}$$

Thus, my transform definitions give the property:

$$f(z) \otimes g(z) \iff 2\pi \hat{f}(s) \hat{g}(s) \quad (\text{F.28})$$

Next, let's define a convolution over wavenumber:

$$\hat{f}(s) \otimes \hat{g}(s) \equiv \int_{-\infty}^{\infty} \hat{f}(s') \hat{g}(s-s') ds'$$

where s' is a dummy variable of integration. Applying my definition of the wavenumber transform to both sides of this expression, we have:

$$\begin{aligned}
\int_{-\infty}^{\infty} [\hat{f}(s) \otimes \hat{g}(s)] e^{isz} ds &= \int_{-\infty}^{\infty} \left[\int_{-\infty}^{\infty} \hat{f}(s') \hat{g}(s-s') ds' \right] e^{isz} ds \\
&= \int_{-\infty}^{\infty} \hat{f}(s') \left[\int_{-\infty}^{\infty} \hat{g}(s-s') e^{isz} ds \right] ds' \\
&= \int_{-\infty}^{\infty} \hat{f}(s') \left[\int_{-\infty}^{\infty} \hat{g}(s-s') e^{i(s-s')z} ds \right] e^{is'z} ds' \\
&= \int_{-\infty}^{\infty} \hat{f}(s') g(z) e^{is'z} ds' = f(z) g(z)
\end{aligned}$$

Thus, my transform definitions give the property:

$$f(z)g(z) \iff \hat{f}(s) \otimes \hat{g}(s) \quad (\text{F.29})$$

F.5 Evaluating Admittances

In this section, I evaluate the admittances by assuming some simple forms for the applied body forces. Here I present my rationale carefully.

In the beginning of Chapter 4, I chose to model the plate with a plate theory, rather than the full 3D elastic theory. This approach is inherently approximate. Thus, it will be physically meaningful to match the *resultants* between the shell and the plate, while it will *not* be physically meaningful to match the *stresses* between the shell model and the plate model (nor would it be possible, as I showed in Fig. 4-2).

With this in mind, I will let all of the even force distributions be the rectangular function with unit area:

$$\begin{aligned} f_{re}(z) = f_{\theta e}(z) = f_{ze}(z) &= \frac{1}{T_p} & -T_p/2 \leq z \leq T_p/2 \\ &= 0 & |z| > T_p/2 \end{aligned}$$

where T_p is the thickness of the plate. This function transforms to be:

$$\hat{f}_{re}(s) = \hat{f}_{\theta e}(s) = \hat{f}_{ze}(s) = \frac{1}{2\pi} \int_{-T_p/2}^{T_p/2} \frac{1}{T_p} e^{-isz} dz = \frac{1}{2\pi} \frac{\sin(sT_p/2)}{(sT_p/2)} \quad (\text{F.30})$$

I justify this choice primarily by considering the rectangular function to be the lowest order of polynomial that can transfer the resultant forces to the shell. Coincidentally, it also happens that $f_{re}(z)$ and $f_{\theta e}(z)$ match the uniform stress distributions I assume for the inplane motions of the plate, but that is not my primary justification.

Similarly, I let the odd force distributions be the linearly varying function:

$$\begin{aligned} f_{ro}(z) = f_{\theta o}(z) &= \frac{12z}{T_p^3} & -T_p/2 \leq z \leq T_p/2 \\ &= 0 & |z| > T_p/2 \end{aligned}$$

where the integral of $f_{r_o}(z) z dz$ over z is one. This function transforms to be:

$$\hat{f}_{r_o}(s) = \hat{f}_{\theta_o}(s) = \frac{1}{2\pi} \int_{-T_p/2}^{T_p/2} \frac{12z}{T_p^3} e^{-isz} dz = \frac{-6i}{\pi s T_p^2} \left[\frac{\sin(sT_p/2)}{(sT_p/2)} - \cos(sT_p/2) \right] \quad (\text{F.31})$$

Similarly, I justify this choice by considering the linearly varying function to be the lowest order polynomial that can transfer the resultant moments to the shell.

The admittances defined above can now be evaluated elegantly in the wavenumber domain. Recall that Eq. (F.29) related a product in the spatial domain to a convolution in the wavenumber domain, and there was no factor of 2π involved. Thus, if we consider any two functions $f(z)$ and $v(z)$ and substitute them into Eq. (F.29), and we then let the wavenumber s equal zero, then we can write:

$$\begin{aligned} \left[\int_{-\infty}^{\infty} [f(z)v(z)] e^{isz} dz \right]_{s=0} &= [\hat{f}(s) \otimes \hat{v}(s)]_{s=0} \\ &= \left[\int_{-\infty}^{\infty} \hat{f}(s') \hat{v}(s-s') ds' \right]_{s=0} = \int_{-\infty}^{\infty} \hat{f}(s) \hat{v}(-s) ds \\ &= \left[\int_{-\infty}^{\infty} \hat{f}(s-s') \hat{v}(s') ds' \right]_{s=0} = \int_{-\infty}^{\infty} \hat{f}(-s) \hat{v}(s) ds \end{aligned}$$

where \otimes is the convolution, and s' is a dummy variable of integration. Next, to see how we can use this, consider letting $f_e(z)$ and $v_e(z)$ be even in z , so we know that $\hat{f}_e(s)$ and $\hat{v}_e(s)$ are even in s , and we can write:

$$\int_{-\infty}^{\infty} f_e(z)v_e(z) dz = 2 \int_0^{\infty} \hat{f}_e(s)\hat{v}_e(s) ds \quad (\text{F.32})$$

Or, if $f_o(z)$ and $v_o(z)$ are odd in z , then we know that $\hat{f}_o(s)$ and $\hat{v}_o(s)$ are odd in s , and we can write:

$$\int_{-\infty}^{\infty} f_o(z)v_o(z) dz = 2 \int_0^{\infty} \hat{f}_o(-s)\hat{v}_o(s) ds \quad (\text{F.33})$$

Knowing this, we can evaluate the entries of the upper 2×2 submatrix of the

admittance matrix. Considering Eqs. (F.28) and (F.32), we can write:

$$\begin{aligned}
Y_{11} &= \int_{-T_p/2}^{T_p/2} f_{re} [\dot{u}_{re}]_{f_{re}} dz = 2 \int_0^\infty (-i\omega 2\pi) \left[\frac{1}{2\pi} \frac{\sin(sT_p/2)}{(sT_p/2)} \right]^2 [\hat{u}_r(s)]_{\mathbf{a}_r \delta(z)} ds \\
Y_{12} &= \int_{-T_p/2}^{T_p/2} f_{re} [\dot{u}_{re}]_{f_{\theta e}} dz = 2 \int_0^\infty (-i\omega 2\pi) \left[\frac{1}{2\pi} \frac{\sin(sT_p/2)}{(sT_p/2)} \right]^2 [\hat{u}_r(s)]_{\mathbf{a}_\theta \delta(z)} ds \\
Y_{21} &= \int_{-T_p/2}^{T_p/2} f_{\theta e} [\dot{u}_{\theta e}]_{f_{re}} dz = 2 \int_0^\infty (-i\omega 2\pi) \left[\frac{1}{2\pi} \frac{\sin(sT_p/2)}{(sT_p/2)} \right]^2 [\hat{u}_\theta(s)]_{\mathbf{a}_r \delta(z)} ds \\
Y_{22} &= \int_{-T_p/2}^{T_p/2} f_{\theta e} [\dot{u}_{\theta e}]_{f_{\theta e}} dz = 2 \int_0^\infty (-i\omega 2\pi) \left[\frac{1}{2\pi} \frac{\sin(sT_p/2)}{(sT_p/2)} \right]^2 [\hat{u}_\theta(s)]_{\mathbf{a}_\theta \delta(z)} ds
\end{aligned}$$

We evaluate the expressions on the right numerically. Note how they involve a simple window in the wavenumber domain, multiplied by our wavenumber solutions for the displacements caused by ring forces concentrated with Dirac deltas $\delta(z)$. We get this by thinking of a convolution in z as a multiplication in s . This introduces a factor of 2π according to Eq. (F.28). For example, the integral for evaluating Y_{11} was written by considering:

$$[\dot{u}_{re}(z)]_{f_{re}} = -i\omega f_{re}(z) \otimes [u_r(z)]_{\mathbf{a}_r \delta(z)} \iff (-i\omega 2\pi) \hat{f}_{re}(s) [\hat{u}_r(s)]_{\mathbf{a}_r \delta(z)} \quad (\text{F.34})$$

Similarly, we can evaluate the entries of the lower 3×3 submatrix of the admittance matrix. The signs of the expressions below can be confusing, but I've written them in a way that can be checked methodically. First, on the first line for each admittance matrix entry, I assemble each integral over wavenumber so the integrand explicitly shows the factor of $(-i\omega 2\pi)$ from Eqs. (F.28) and (F.34), and I also write the argument $(-s)$ that arises for odd functions from Eq. (F.33). Then, on the second line for each admittance matrix entry, inside the integrals, I write the transforms of the windows with the signs they have in Eqs. (F.30) and (F.31). This will simplify the computer coding. Following these procedures, I write:

$$Y_{33} = \int_{-T_p/2}^{T_p/2} f_{ze} [\dot{u}_{ze}]_{f_{ze}} dz = 2 \int_0^\infty (-i\omega 2\pi) \hat{f}_{ze}(s) \hat{f}_{ze}(-s) [\hat{u}_{ze}(s)]_{\mathbf{a}_z \delta(z)} ds$$

$$\begin{aligned}
&= -4\pi i\omega \int_0^\infty \left[\frac{1}{2\pi} \frac{\sin(sT_p/2)}{(sT_p/2)} \right]^2 [\hat{u}_z(s)]_{\mathbf{a}_z\delta(z)} ds \\
Y_{34} &= -\int_{-T_p/2}^{T_p/2} f_{ze} [\dot{u}_{ze}]_{f_{\theta o}} dz = -2 \int_0^\infty (-i\omega 2\pi) \hat{f}_{ze}(s) \hat{f}_{\theta o}(-s) [\hat{u}_z(s)]_{\mathbf{a}_\theta\delta(z)} ds \\
&= -4\pi i\omega \int_0^\infty \left[\frac{1}{2\pi} \frac{\sin(sT_p/2)}{(sT_p/2)} \right] \frac{-6i}{\pi s T_p^2} \left[\frac{\sin(sT_p/2)}{(sT_p/2)} - \cos(sT_p/2) \right] [\hat{u}_z(s)]_{\mathbf{a}_\theta\delta(z)} ds \\
Y_{35} &= \int_{-T_p/2}^{T_p/2} f_{ze} [\dot{u}_{ze}]_{f_{ro}} dz = 2 \int_0^\infty (-i\omega 2\pi) \hat{f}_{ze}(s) \hat{f}_{ro}(-s) [\hat{u}_z(s)]_{\mathbf{a}_r\delta(z)} ds \\
&= 4\pi i\omega \int_0^\infty \left[\frac{1}{2\pi} \frac{\sin(sT_p/2)}{(sT_p/2)} \right] \frac{-6i}{\pi s T_p^2} \left[\frac{\sin(sT_p/2)}{(sT_p/2)} - \cos(sT_p/2) \right] [\hat{u}_z(s)]_{\mathbf{a}_r\delta(z)} ds \\
Y_{43} &= -\int_{-T_p/2}^{T_p/2} f_{\theta o} [\dot{u}_{\theta o}]_{f_{ze}} dz = -2 \int_0^\infty (-i\omega 2\pi) \hat{f}_{\theta o}(s) \hat{f}_{ze}(-s) [\hat{u}_\theta(s)]_{\mathbf{a}_z\delta(z)} ds \\
&= 4\pi i\omega \int_0^\infty \frac{-6i}{\pi s T_p^2} \left[\frac{\sin(sT_p/2)}{(sT_p/2)} - \cos(sT_p/2) \right] \left[\frac{1}{2\pi} \frac{\sin(sT_p/2)}{(sT_p/2)} \right] [\hat{u}_\theta(s)]_{\mathbf{a}_z\delta(z)} ds \\
Y_{44} &= \int_{-T_p/2}^{T_p/2} f_{\theta o} [\dot{u}_{\theta o}]_{f_{\theta o}} dz = 2 \int_0^\infty (-i\omega 2\pi) \hat{f}_{\theta o}(s) \hat{f}_{\theta o}(-s) [\hat{u}_\theta(s)]_{\mathbf{a}_\theta\delta(z)} ds \\
&= 4\pi i\omega \int_0^\infty \frac{-36}{\pi^2 s^2 T_p^4} \left[\frac{\sin(sT_p/2)}{(sT_p/2)} - \cos(sT_p/2) \right]^2 [\hat{u}_\theta(s)]_{\mathbf{a}_\theta\delta(z)} ds \\
Y_{45} &= -\int_{-T_p/2}^{T_p/2} f_{\theta o} [\dot{u}_{\theta o}]_{f_{ro}} dz = -2 \int_0^\infty (-i\omega 2\pi) \hat{f}_{\theta o}(s) \hat{f}_{ro}(-s) [\hat{u}_\theta(s)]_{\mathbf{a}_r\delta(z)} ds \\
&= -4\pi i\omega \int_0^\infty \frac{-36}{\pi^2 s^2 T_p^4} \left[\frac{\sin(sT_p/2)}{(sT_p/2)} - \cos(sT_p/2) \right]^2 [\hat{u}_\theta(s)]_{\mathbf{a}_r\delta(z)} ds \\
Y_{53} &= \int_{-T_p/2}^{T_p/2} f_{ro} [\dot{u}_{ro}]_{f_{ze}} dz = 2 \int_0^\infty (-i\omega 2\pi) \hat{f}_{ro}(s) \hat{f}_{ze}(-s) [\hat{u}_r(s)]_{\mathbf{a}_z\delta(z)} ds \\
&= -4\pi i\omega \int_0^\infty \frac{-6i}{\pi s T_p^2} \left[\frac{\sin(sT_p/2)}{(sT_p/2)} - \cos(sT_p/2) \right] \left[\frac{1}{2\pi} \frac{\sin(sT_p/2)}{(sT_p/2)} \right] [\hat{u}_r(s)]_{\mathbf{a}_z\delta(z)} ds \\
Y_{54} &= -\int_{-T_p/2}^{T_p/2} f_{ro} [\dot{u}_{ro}]_{f_{\theta o}} dz = -2 \int_0^\infty (-i\omega 2\pi) \hat{f}_{ro}(s) \hat{f}_{\theta o}(-s) [\hat{u}_r(s)]_{\mathbf{a}_\theta\delta(z)} ds \\
&= -4\pi i\omega \int_0^\infty \frac{-36}{\pi^2 s^2 T_p^4} \left[\frac{\sin(sT_p/2)}{(sT_p/2)} - \cos(sT_p/2) \right]^2 [\hat{u}_r(s)]_{\mathbf{a}_\theta\delta(z)} ds
\end{aligned}$$

$$\begin{aligned}
Y_{55} &= \int_{-T_p/2}^{T_p/2} f_{r_o}[\dot{u}_{r_o}]_{f_{r_o}} dz = 2 \int_0^\infty (-i\omega 2\pi) \hat{f}_{r_o}(s) \hat{f}_{r_o}(-s) [\hat{u}_r(s)]_{\mathbf{a}_r \delta(z)} ds \\
&= 4\pi i\omega \int_0^\infty \frac{-36}{\pi^2 s^2 T_p^4} \left[\frac{\sin(sT_p/2)}{(sT_p/2)} - \cos(sT_p/2) \right]^2 [\hat{u}_r(s)]_{\mathbf{a}_r \delta(z)} ds
\end{aligned}$$

Clearly, these integrals are all convergent, because their “tails” decay as s^{-3} or faster along the real s -axis. We introduced this decay ourselves by applying the resultant forces and moments to the shell using some simple window functions $f(z) \iff \hat{f}(s)$. Thus, the integrals are convergent, in the sense that they have some theoretically defined result that is finite. However, these integrals still must be computed with care, because the integrands have some properties that present special numerical challenges:

- The integrands grow exponentially away from the real s -axis. This growth is due to the functions $\sin(sT_p/2)$ and $\cos(sT_p/2)$. Therefore, large contour offsets cannot be used for numerical evaluation of the integrals, because large contour offsets would involve adding and subtracting numbers that would be very large compared to the final result desired, and the true answer would be lost in the numerical noise. To visualize the exponential growth involved away from the real axis, Fig. F-1 shows the sinc function $\sin(x)/x$ as a function of a non-dimensional complex variable x .
- The decay provided by the windows is only evident on a relatively large scale in the wavenumber domain. Consider that in the spatial domain, the plate is thin compared to the lengths of the waves that propagate in the shell. Thus, in the wavenumber domain, the poles corresponding to the propagating waves are clustered close to the origin compared to the scale of the decay of the windows that are used to apply the forces and moments to the shell. Therefore, the windows define the integrals to converge in theory, in the sense that the integral is defined to have a finite value as a result, but the windows do not yet help convergence numerically. Consider that the poles and branch cuts of the integrand should contain all of the information about the physics of the shell,

yet even when we integrate past the poles and branch cuts, there is still a large amount of integration still to be done before the integrand decays appreciably. Thus, the direct numerical evaluation of the integrals defined above is a poorly-posed numerical problem.

- Furthermore, the odd windows have a zero at the origin in the wavenumber domain, and considering that the windows occupy a larger wavenumber scale than the poles and branch cuts, we see that the windows are *steadily increasing* over the region of the wavenumber plane that describes the physics of the shell!

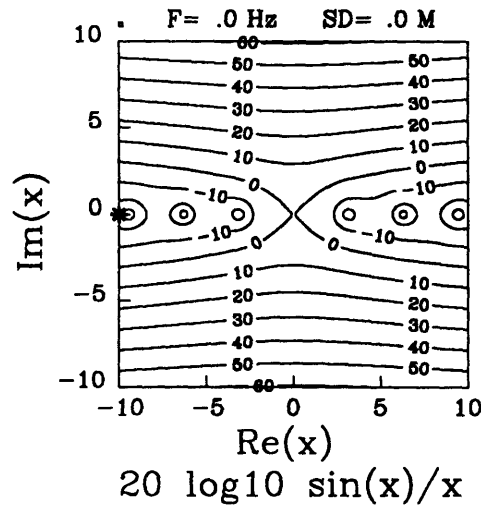


Figure F-1: The magnitude of the sinc function $\sin(x)/x$, plotted here as $20 \log_{10} |\sin(x)/x|$. As we would expect, the sinc function goes to 1 at the origin $x = 0$, and it has zeroes at $x = \pm\pi, \pm 2\pi, \pm 3\pi$, etc. Note the exponential growth away from the real s -axis.

To address these issues, it will be necessary to use small contour offsets. And, we should somehow subtract away the part of the integrand that occupies the large wavenumber scale and causes convergence problems. The different parts of the integrand could then be integrated adaptively using different, appropriate scales in the wavenumber domain. I recommend doing this as future work in Chapter 6.

F.6 Checking Admittances

In this section, I provide some ways to check the numerically computed values of the admittance matrix:

First, we can check the special case of axisymmetric excitations. Setting the order equal to zero, we should observe the numerical results $Y_{12} \doteq Y_{21} \doteq 0$, $Y_{34} \doteq Y_{43} \doteq 0$, and $Y_{45} \doteq Y_{54} \doteq 0$. This is what we should get for axisymmetric excitations.

Second, we can check power flow. All of the on-diagonal entries should have positive real parts. This will mean that any of the 5 resultants will inject positive net power into the shell (when applied individually). I haven't thought about reciprocity or power relations that might be derived to constrain the off-diagonal entries.

Third, we can check the global dynamics of the shell that can arise when the order is set equal to zero or one. To check these dynamics, let the shell have a single layer, and let the shell be in a vacuum. Let R_s be the average radius of the shell, T_s be the thickness of the shell, ρ_s be the density of the shell material, c_s be the shear wavespeed of the shell material, c_{Ls} be the longitudinal wavespeed of waves in a thin plate made of the shell material. Using these terms:

- The torsional mode of the shell should be recovered by setting the order equal to zero. In this case, $Y_{22} \approx 1/(2T_s\rho_sc_s)$. The factor of two arises because torsional waves propagate away from the origin in both directions toward $z \rightarrow \pm\infty$. Also, as $\omega \rightarrow 0$, the shell will act rigid across its thickness, so we can re-write the above approximation more rigorously as a limit: $Y_{22} \rightarrow 1/(2T_s\rho_sc_s)$ as $\omega \rightarrow 0$.
- The axial compression mode of the shell should be recovered by setting the order equal to zero. In this case, $Y_{33} \approx 1/(2T_s\rho_sc_{Ls})$. Again, the factor of two arises because waves propagate away from the origin in both directions toward $z \rightarrow \pm\infty$.
- The beam bending of the shell should be recovered by setting the order equal to one and letting the frequency become low. This fact was demonstrated by the

examples shown in Section 3.3.5. Here I will predict the admittances associated with beam bending. To evaluate this, I'll consider the shell to act as a beam that has a linear density ρ_b kg/m and a flexural wavenumber k_b m⁻¹. I'll consider the shell to be in a vacuum, but the shell need not be thin. Next, I'll consider the resulting "beam" to be excited by ring forces and moments that have a radius r' . Now, recall the Cartesian coordinate axes x and y that are both perpendicular to the z -axis, as shown in Fig. 5-1. Next, consider the following:

- ▷ A ring force $F_r e^{i(\theta-\omega t)}$ N/m in the r -direction applies a net force in the x -direction of $\pi r' F_r e^{-i\omega t}$ N and a net force in the y -direction of $i\pi r' F_r e^{-i\omega t}$ N.
- ▷ A ring force $F_\theta e^{i(\theta-\omega t)}$ N/m in the θ -direction applies a net force in the x -direction of $-i\pi r' F_\theta e^{-i\omega t}$ N and a net force in the y -direction of $\pi r' F_\theta e^{-i\omega t}$ N.
- ▷ A ring force $F_z e^{i(\theta-\omega t)}$ N/m in the z -direction applies a net moment about the x -axis of $i\pi r'^2 F_z e^{-i\omega t}$ N-m and a net moment about the y -axis of $-\pi r'^2 F_z e^{-i\omega t}$ N-m.
- ▷ A ring moment $M_r e^{i(\theta-\omega t)}$ N-m/m about the r -axis applies a net moment about the x -axis of $\pi r' M_r e^{-i\omega t}$ N-m and a net moment about the y -axis of $i\pi r' M_r e^{-i\omega t}$ N-m.
- ▷ A ring moment $M_\theta e^{i(\theta-\omega t)}$ N-m/m about the θ -axis applies a net moment about the x -axis of $-i\pi r' M_\theta e^{-i\omega t}$ N-m and a net moment about the y -axis of $\pi r' M_\theta e^{-i\omega t}$ N-m.

And, assuming a time factor of $e^{-i\omega t}$, it can be shown that the admittance of a beam to a unit transverse force is $k_b(1+i)/(4\rho_b\omega)$, and the admittance of a beam to a unit transverse moment is $k_b^3(1-i)/(4\rho_b\omega)$. Also, if the cross-section of the beam is rotating without deformation about $\{x, y, z\} = \{0, 0, 0\}$, then $\dot{U}_z = -r'\Omega_\theta$ if \dot{U}_z is measured at $r = r'$. Combining these facts, we predict that the admittances for the shell will take on the following forms for beam bending

as $\omega \rightarrow 0$ for $\nu = 1$:

$$\begin{bmatrix} Y_{11} & Y_{12} \\ Y_{21} & Y_{22} \end{bmatrix} \rightarrow \frac{\pi k_b r' (1+i)}{4\rho_b \omega} \begin{bmatrix} 1 & -i \\ i & 1 \end{bmatrix} \quad (\text{F.35})$$

$$\begin{bmatrix} Y_{33} & Y_{34} & Y_{35} \\ Y_{43} & Y_{44} & Y_{45} \\ Y_{53} & Y_{54} & Y_{55} \end{bmatrix} \rightarrow \frac{\pi k_b^3 r'^2 (1-i)}{4\rho_b \omega} \begin{bmatrix} r' & -i & -1 \\ i & 1/r' & -i/r' \\ -1 & i/r' & 1/r' \end{bmatrix} \quad (\text{F.36})$$

This should provide a satisfying check on the formulation and computer programming, considering that the shell's admittance matrix is implemented using integrals of many different integrands over wavenumber. Also, the symmetry and antisymmetry within the matrix is notable.

F.7 Velocities for the Empty Shell

Using the ideas and the nomenclature detailed in this appendix, this section defines the vector of velocities for the empty shell:

$$\mathbf{V}_{\text{empty}} \equiv \{ \dot{U}_r, \dot{U}_\theta, \dot{U}_z, \Omega_r, \Omega_\theta \}_{\text{empty}}$$

Equation (4.11) defined $\mathbf{V}_{\text{empty}}$ implicitly in terms of power flow:

$$\mathbf{F}_i^T \mathbf{V}_{\text{pi}}^* = \mathbf{F}_i^T \mathbf{V}_{\text{si}}^* + \mathbf{F}_i^T \mathbf{V}_{\text{empty}}^*$$

Therefore, to define $\mathbf{V}_{\text{empty}}$ explicitly here, I define $\mathbf{V}_{\text{empty}}$ in terms of the power flow due to a vector \mathbf{F} of unit forces and moments, so that multiplying by \mathbf{F}_i^T will give the power flow due to \mathbf{F}_i . To define this in detail, I use the same body force distributions that I used to define the effect of the plate on the shell (f_{re} , $f_{\theta e}$, etc.). Letting the axial wavenumber of the incident wave be s_i , and assuming s_i to be real, I write the following integrals that involve the empty shell velocities for the full

3D elastic model weighted by the distributed body forces that correspond to unit resultant forces and moments:

$$\begin{aligned}
[\dot{U}_r]_{empty}^* &\equiv \int_{-T_p/2}^{T_p/2} \frac{1}{T_p} [\dot{u}_r(r', \theta, 0)_{empty} e^{is_i z}]^* dz = \frac{\sin(s_i T_p/2)}{(s_i T_p/2)} \dot{u}_r^*(r', \theta, 0)_{empty} \\
[\dot{U}_\theta]_{empty}^* &\equiv \int_{-T_p/2}^{T_p/2} \frac{1}{T_p} [\dot{u}_\theta(r', \theta, 0)_{empty} e^{is_i z}]^* dz = \frac{\sin(s_i T_p/2)}{(s_i T_p/2)} \dot{u}_\theta^*(r', \theta, 0)_{empty} \\
[\dot{U}_z]_{empty}^* &\equiv \int_{-T_p/2}^{T_p/2} \frac{1}{T_p} [\dot{u}_z(r', \theta, 0)_{empty} e^{is_i z}]^* dz = \frac{\sin(s_i T_p/2)}{(s_i T_p/2)} \dot{u}_z^*(r', \theta, 0)_{empty} \\
[\Omega_r]_{empty}^* &\equiv \int_{-T_p/2}^{T_p/2} \frac{-12z}{T_p^3} [\dot{u}_\theta(r', \theta, 0)_{empty} e^{is_i z}]^* dz \\
&= \frac{12i}{s_i T_p^2} \left[\frac{\sin(s_i T_p/2)}{(s_i T_p/2)} - \cos(s_i T_p/2) \right] \dot{u}_\theta^*(r', \theta, 0)_{empty} \\
[\Omega_\theta]_{empty}^* &\equiv \int_{-T_p/2}^{T_p/2} \frac{12z}{T_p^3} [\dot{u}_r(r', \theta, 0)_{empty} e^{is_i z}]^* dz \\
&= \frac{-12i}{s_i T_p^2} \left[\frac{\sin(s_i T_p/2)}{(s_i T_p/2)} - \cos(s_i T_p/2) \right] \dot{u}_r^*(r', \theta, 0)_{empty}
\end{aligned}$$

Finally, I can verify these expressions in a very satisfying way. Consider that $(s_i T_p/2)$ is small for the frequency range of interest. Thus, it is instructive to consider how the expressions above behave as $(s_i T_p/2) \rightarrow 0$. In this case, the sinc function $[\sin(s_i T_p/2)]/(s_i T_p/2) \rightarrow 1$, so the expressions for the translational velocities reduce to:

$$[\dot{U}_r]_{empty}^* \rightarrow \dot{u}_r^*(r', \theta, 0)_{empty} \quad [\dot{U}_\theta]_{empty}^* \rightarrow \dot{u}_\theta^*(r', \theta, 0)_{empty} \quad [\dot{U}_z]_{empty}^* \rightarrow \dot{u}_z^*(r', \theta, 0)_{empty}$$

Or, taking the conjugates of these expressions, we have:

$$[\dot{U}_r]_{empty} \rightarrow \dot{u}_r(r', \theta, 0)_{empty} \quad [\dot{U}_\theta]_{empty} \rightarrow \dot{u}_\theta(r', \theta, 0)_{empty} \quad [\dot{U}_z]_{empty} \rightarrow \dot{u}_z(r', \theta, 0)_{empty}$$

These results are exactly what we want to see. And, to examine the expressions for the rotational velocities, consider that as $(s_i T_p/2) \rightarrow 0$,

$$\frac{12i}{s_i T_p^2} \left[\frac{\sin(s_i T_p/2)}{(s_i T_p/2)} - \cos(s_i T_p/2) \right] \rightarrow is_i$$

Thus, the expressions for the rotational velocities reduce to:

$$[\Omega_r]^*_{empty} \rightarrow i s_i \dot{u}_\theta^*(r', \theta, 0)_{empty} \quad [\Omega_\theta]^*_{empty} \rightarrow -i s_i \dot{u}_r^*(r', \theta, 0)_{empty}$$

Recalling that I assumed s_i to be real, the conjugates of these expressions are:

$$[\Omega_r]_{empty} \rightarrow -i s_i \dot{u}_\theta(r', \theta, 0)_{empty} \quad [\Omega_\theta]_{empty} \rightarrow i s_i \dot{u}_r(r', \theta, 0)_{empty}$$

Considering the implied axial dependence of $e^{i s_i z}$, these last two expressions mean:

$$[\Omega_r]_{empty} \rightarrow -\left. \frac{\partial \dot{u}_\theta(r', \theta, z)_{empty}}{\partial z} \right|_{z=0} \quad [\Omega_\theta]_{empty} \rightarrow \left. \frac{\partial \dot{u}_r(r', \theta, z)_{empty}}{\partial z} \right|_{z=0}$$

Again, these results are exactly what we want to see.

This page is blank.

Appendix G

Form Functions

This appendix organizes the mathematical arguments I use to compute form functions. In particular, I present mathematical details of the following subjects:

1. I review the mathematical description of an obliquely incident plane wave in terms of cylindrical harmonics.
2. I consider the cylindrically spreading field scattered from an infinite cylindrical shell. I review the definition of its form function, and I show how I compute form functions in terms of DGM solutions, where a shell can have any number of viscoelastic layers. Also, I review the simple analytical results for the special cases of acoustically soft and hard bodies.
3. I consider the spherically spreading field scattered from a stiffener inside a shell. I review the definition of its form function, and I show how I compute the form function in terms of DGM solutions.

G.1 An Obliquely Incident Plane Wave

An obliquely incident plane wave has been synthesized in terms of cylindrical harmonics before [10] [11]. A complete derivation is presented here to establish the nomenclature clearly. First, I reproduce Fig. 5-1 for easy reference here as Fig. G-1, and I define the following parameters:

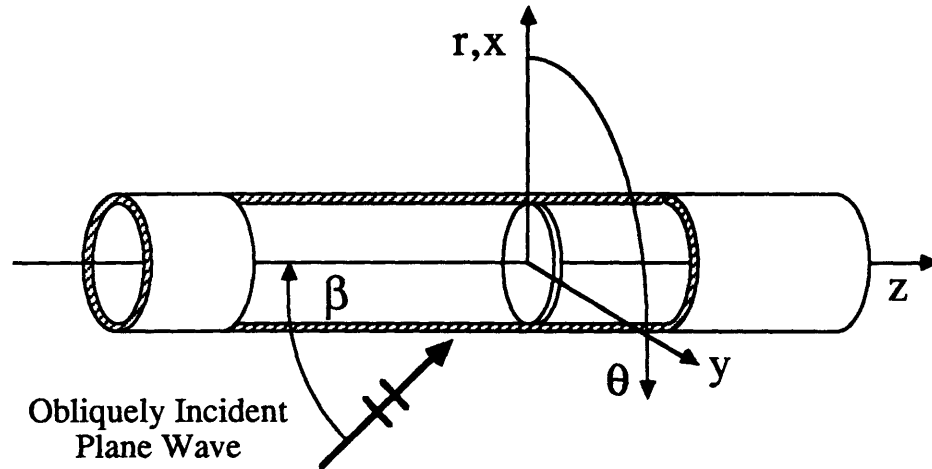


Figure G-1: Geometry for the acoustic scattering problem.

- Let β be the angle of incidence, measured where the incident wave's intensity vectors intersect the shell's axis. Let $\beta = 0$ correspond to a wave travelling parallel to the z -axis in the positive z -direction, and let $\beta = \pi/2$ correspond to broadside incidence.
- Let the intensity vectors of the incident wave be parallel to the shell's coordinate plane $\theta = 0$. This gives no loss of generality, considering the rotational symmetry of the shell with respect to θ .
- Let x be a Cartesian coordinate axis identical to the shell's r -axis in the plane $\theta = 0$. Thus, $x = 0$ corresponds to $r = 0$, and the incident wave's intensity vectors are parallel to the x - z plane.
- Let h_N be the wavenumber of the incident wave, because it is a compressional wave in the outermost layer of our cylindrically layered system.

- Let h_{xi} be the wavenumber of the incident wave projected onto the x -axis, and let h_{zi} be the wavenumber of the incident wave projected onto the z -axis. Thus, I define $h_{xi} \equiv h_N \sin \beta$ and $h_{zi} \equiv h_N \cos \beta$.

Given these parameters, the incident plane wave is most clearly described in the Cartesian $\{x, z\}$ coordinates by writing it as a travelling wave in the x - z plane:

$$p_i(x, z) = P_i e^{ih_{zi}z} e^{ih_{xi}x} \quad (\text{G.1})$$

where P_i is the magnitude of the pressure at $\{x, z\} = \{0, 0\}$. Equation (G.1) can be re-written in the shell's $\{r, \theta, z\}$ coordinates by noting that $x = r \cos \theta$, and by defining the parameter:

$$h_{ri}^2 \equiv h_N^2 - h_{zi}^2$$

This expression defines h_{ri} to have the form of a radial wavenumber in the context of separation of variables in cylindrical coordinates, but it also defines h_{ri} to equal h_{xi} . Thus, Eq. (G.1) can be re-written as:

$$p_i(r, \theta, z) = P_i e^{ih_{zi}z} e^{ih_{ri}r \cos \theta}$$

The r - θ dependence of this last equation can be re-written using Bessel functions by using an expression presented by Morse and Ingard [73], so Eq. (G.1) becomes:

$$p_i(r, \theta, z) = P_i e^{ih_{zi}z} \left[J_0(h_{ri}r) + 2 \sum_{m=1}^{\infty} i^m \cos(m\theta) J_m(h_{ri}r) \right] \quad (\text{G.2})$$

However, in this thesis, I develop formulations and computer codes that describe the θ -dependence of shells and plates in terms of $e^{i\nu\theta}$. Therefore, I need to re-write Eq. (G.2) to be compatible with those formulations and computer codes:

$$\begin{aligned} p_i(r, \theta, z) &= P_i e^{ih_{zi}z} \left[J_0(h_{ri}r) + \sum_{m=1}^{\infty} i^m (e^{im\theta} + e^{-im\theta}) J_m(h_{ri}r) \right] \\ &= P_i e^{ih_{zi}z} \left[J_0(h_{ri}r) + \sum_{m=1}^{\infty} i^m e^{im\theta} J_m(h_{ri}r) + \sum_{m=-\infty}^{-1} i^{|m|} e^{im\theta} J_{|m|}(h_{ri}r) \right] \end{aligned}$$

$$= P_i e^{ih_{zi}z} \sum_{m=-\infty}^{\infty} i^{|m|} e^{im\theta} J_{|m|}(h_{ri}r) \quad (\text{G.3})$$

And, I need to know the radial displacement of the incident wave, which I will call u_{ri} . I find u_{ri} using the momentum equation:

$$u_{ri}(r, \theta, z) = \frac{1}{\rho_N \omega^2} \frac{\partial p_i}{\partial r} = \frac{P_i e^{ih_{zi}z}}{\rho_N \omega^2} \sum_{m=-\infty}^{\infty} i^{|m|} e^{im\theta} \frac{dJ_{|m|}(h_{ri}r)}{dr} \quad (\text{G.4})$$

G.2 Cylindrically Spreading Waves

In this section, I consider the cylindrically spreading waves that result from the scattering of a plane wave from an infinite cylindrical shell. I review the definition of its form function, I show how I compute the form function in terms of the DGM solutions, and I review the special cases of acoustically soft and hard bodies.

To notate the expressions involved, I consider the total pressure field $p_t(r, \theta, z)$ to be the incident pressure field $p_i(r, \theta, z)$ plus the scattered pressure field $p_s(r, \theta, z)$:

$$p_t(r, \theta, z) = p_i(r, \theta, z) + p_s(r, \theta, z)$$

I consider these pressure fields in terms of contributions from integer orders m :

$$p_t = \sum_{m=-\infty}^{\infty} p_{tm} \quad p_i = \sum_{m=-\infty}^{\infty} p_{im} \quad p_s = \sum_{m=-\infty}^{\infty} p_{sm}$$

Similarly, I consider the radial displacements u_r associated with these pressure fields:

$$u_{rt} = \sum_{m=-\infty}^{\infty} u_{rtm} \quad u_{ri} = \sum_{m=-\infty}^{\infty} u_{rim} \quad u_{rs} = \sum_{m=-\infty}^{\infty} u_{rsm}$$

For the incident field, I already know p_{im} and u_{rim} from Eqs. (G.3) and (G.4):

$$\begin{aligned} p_{im}(r, \theta, z) &= P_i i^{|m|} J_{|m|}(h_{ri}r) e^{im\theta} e^{ih_{zi}z} \\ u_{rim}(r, \theta, z) &= \frac{P_i i^{|m|}}{\rho_N \omega^2} \frac{dJ_{|m|}(h_{ri}r)}{dr} e^{im\theta} e^{ih_{zi}z} \end{aligned}$$

To solve for the response numerically, I apply p_{im} and u_{rim} to the DGM model as a “right-hand side” for some given values of $e^{im\theta}$ and $e^{ih_z z}$, and then I solve numerically for the homogeneous solutions. This gives numerical solutions to the empty shell problem, order by order. Thus, by adding over the integer orders, the scattered pressure can be computed in terms of the DGM results as:

$$p_s(r, \theta, z) = \lambda_N h_N^2 \sum_{m=-\infty}^{\infty} \frac{A_N H_{|m|}^{(1)}(h_{ri} r)}{H_{|m|}^{(1)}(h_{ri} R_{N-1})} e^{im\theta} e^{ih_z z} \quad (\text{G.5})$$

where R_{N-1} is the outer radius of the shell, and A_N is the amplitude of the displacement potential ϕ_N in the outermost layer N .

Next, to compute the scattered pressure in the far field, consider that the asymptotic form of the Hankel function for large arguments can be written two ways for positive orders m [52]:

$$H_{|m|}^{(1)}(h_{ri} r) \rightarrow \frac{\sqrt{2} e^{i(h_{ri} r - |m|\pi/2 - \pi/4)}}{\sqrt{\pi h_{ri} r}} = \frac{\sqrt{2} i^{-|m|} e^{ih_{ri} r}}{\sqrt{i\pi h_{ri} r}} \quad (\text{G.6})$$

Substituting the latter formula into Eq. (G.5), we have:

$$p_s(r, \theta, z) \rightarrow \sum_{m=-\infty}^{\infty} \frac{\lambda_N h_N^2 A_N}{H_{|m|}^{(1)}(h_{ri} R_{N-1})} \left(\frac{\sqrt{2} i^{-|m|} e^{ih_{ri} r}}{\sqrt{i\pi h_{ri} r}} \right) e^{im\theta} e^{ih_z z}$$

which can finally be re-written as:

$$p_s(r, \theta, z) \rightarrow P_i \sqrt{\frac{R_{N-1}}{2r}} e^{ih_{ri} r} e^{ih_z z} \left\{ \frac{2\lambda_N h_N^2}{P_i \sqrt{i\pi h_{ri} R_{N-1}}} \sum_{m=-\infty}^{\infty} \frac{A_N i^{-|m|} e^{im\theta}}{H_{|m|}^{(1)}(h_{ri} R_{N-1})} \right\} \quad (\text{G.7})$$

The normalization outside the brackets is the normalization commonly used to define a form function for a cylindrically spreading scattered field. Thus, the quantity inside the brackets is the form function. Note that R_{N-1} is simply my nomenclature for the outer radius of the body. The form function is an asymptotic result for large r that depends only on θ , because the dependence on r and z is simple enough to be removed and placed outside the brackets. Also, the form function typically goes to

one at high frequencies in the backscattered direction for normal incidence, because the form function is normalized appropriately in terms of a high frequency geometrical ray interpretation.

Note that to observe backscattering, we substitute $\theta = \pi$ in these expressions. This is consistent with the geometry defined in Fig. G-1 and the plane wave introduced in Eq. (G.1). Thus, for backscattering, the factor $e^{im\theta}$ in Eq. (G.7) gives alternating signs, as $e^{im\pi} = (-1)^m$.

G.2.1 Acoustically Soft Body

This subsection reviews the special case of the cylindrical body being acoustically soft, so the total pressure at the outer radius of the body is zero. Considering the incident pressure field from Eq. (G.3), and letting the outer radius of the soft body be $r = R_1$, the scattered pressure field must be:

$$p_s(r, \theta, z) = -P_i e^{ih_z z} \sum_{m=-\infty}^{\infty} \frac{i^{|m|} J_{|m|}(h_{ri} R_1)}{H_{|m|}^{(1)}(h_{ri} r)} e^{im\theta} H_{|m|}^{(1)}(h_{ri} r)$$

This expression gives the desired relationship that $p_i + p_s = 0$ at the outer radius of the body. And, considering the large argument asymptotic form for the Hankel function from Eq. (G.6), we can write:

$$p_s(r, \theta, z) \rightarrow P_i \sqrt{\frac{R_1}{2r}} e^{ih_{ri} r} e^{ih_z z} \left\{ \frac{-2}{\sqrt{i\pi h_{ri} R_1}} \sum_{m=-\infty}^{\infty} \frac{J_{|m|}(h_{ri} R_1)}{H_{|m|}^{(1)}(h_{ri} R_1)} e^{im\theta} \right\} \quad (\text{G.8})$$

where the quantity in brackets is the form function.

Note how the series for p_s converges. For a fixed value of the argument $h_{ri} R_1$, increasing the order m causes the factor $J_{|m|}(h_{ri} R_1)/H_{|m|}^{(1)}(h_{ri} R_1)$ to decrease, according to the recurrence relations for Bessel functions [52]. Also, to observe backscattering, note that $\theta = \pi$ in Fig. G-1, so $e^{im\theta} = (-1)^m$.

It should be noted that this form function goes to infinity as the non-dimensional

frequency $h_{ri}R_1$ goes to zero. This is due to the contribution for $m = 0$. In the numerator of Eq. (G.8), $J_0(x)$ goes to 1 as $x \rightarrow 0$. In the denominator, $H_0^{(1)}(x) \rightarrow (2/\pi) \ln(x)$ as $x \rightarrow 0$ [52]. Thus, we should consider the denominator to go as $\sqrt{x} \ln(x)$ as $x \rightarrow 0$. From Abramowitz and Stegun, we find that $\lim_{x \rightarrow 0} x^\alpha \ln(x) = 0$ for $\alpha = 1/2$ [74], provided that $\text{Re}\{x\} > 0$. Thus, the denominator goes to zero as the numerator goes to one, and this causes the form function to go to infinity.

However, the terms for $m \neq 0$ go to zero. To show this, consider the asymptotic forms $J_\nu(x) \rightarrow (x/2)^\nu \Gamma(\nu + 1)$ and $H_\nu^{(1)}(x) \rightarrow (i/\pi) \Gamma(\nu) (x/2)^{-\nu}$, which are valid for $x \rightarrow 0$ and $\text{Re}\{\nu\} > 0$ [52]. Substituting $|m|$ for ν , we have $J_{|m|}(x)/H_{|m|}^{(1)}(x) \rightarrow (\pi/i)|m|(x/2)^{2|m|}$. Thus, the terms for $m \neq 0$ go to zero as $h_{ri}R_1$ goes to zero, so the $m \neq 0$ terms do not change our conclusion that the form function for the soft body goes to infinity as frequency goes to zero.

G.2.2 Acoustically Hard Body

This subsection reviews the special case of the cylindrical body being acoustically hard, so the total radial displacement at the outer radius of the body is zero. Letting R_1 be the outer radius of the body, and considering the incident displacement field from Eq. (G.4), the scattered pressure field must be:

$$p_s(r, \theta, z) = -P_i e^{ih_{zi}z} \sum_{m=-\infty}^{\infty} i^{|m|} \left(\frac{dJ_{|m|}(h_{ri}r)/dr}{dH_{|m|}^{(1)}(h_{ri}r)/dr} \right)_{r=R_1} e^{im\theta} H_{|m|}^{(1)}(h_{ri}r)$$

This expression gives the desired relationship that $\partial p_i / \partial r + \partial p_s / \partial r = 0$ at $r = R_1$. And, by substituting the large argument asymptotic form of the Hankel function, we find the pressure in the far field approaches the asymptotic form:

$$p_s(r, \theta, z) \rightarrow P_i \sqrt{\frac{R_1}{2r}} e^{ih_{ri}r} e^{ih_{zi}z} \left\{ \frac{-2}{\sqrt{i\pi h_{ri}R_1}} \sum_{m=-\infty}^{\infty} \left(\frac{dJ_{|m|}(h_{ri}r)/dr}{dH_{|m|}^{(1)}(h_{ri}r)/dr} \right)_{r=R_1} e^{im\theta} \right\} \quad (\text{G.9})$$

where the quantity in brackets is the form function. This form function goes to zero as the non-dimensional frequency $h_{r_i}R_1$ goes to zero.

Figure G-2 shows DGM calculations of the form functions for the acoustically soft and hard bodies at normal incidence. The soft body is modeled with a 3-layer DGM model. Layer 1 is a vacuum that extends over the interval $0 \leq r \leq R_1$. Layer 2 is a dummy fluid layer that extends over the interval $R_1 \leq r \leq R_2$, where $R_2 = 1.0001R_1$. Layer 3 is a fluid layer that extends to infinity. The dummy fluid layer is necessary in the DGM method so that there is a global matrix system to solve (in this case, 2×2). The fluid layers have identical densities and wave speeds. The hard body is modeled with a 2-layer DGM model. The two layers are fluid layers, where $\rho_1 = 1000\rho_2$ and $c_{c1} = 1000c_{c2}$.

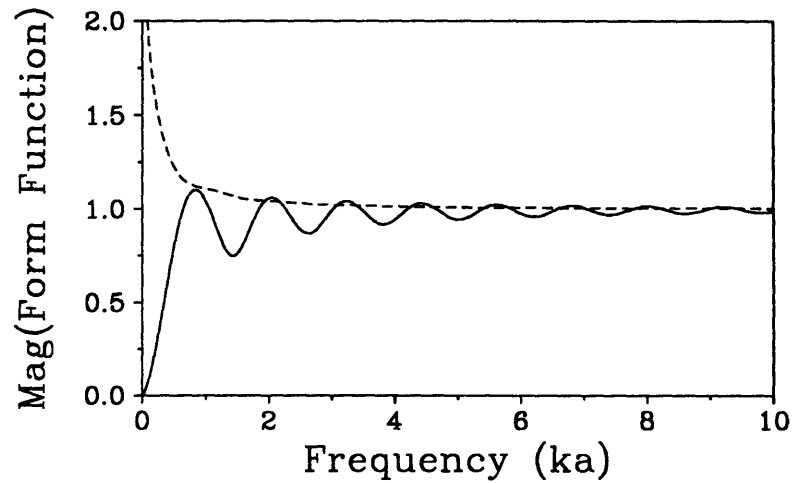


Figure G-2: DGM computations of the form functions for the acoustically soft and hard cylindrical bodies at normal incidence. The soft body is represented by the dashed line, and the hard body is represented by the solid line. The integer orders $-20 \leq m \leq 20$ were included.

G.3 Spherically Spreading Waves

In this section, I consider the waves caused by the reactions of the plate that is installed inside the shell. These waves are spherically spreading in the far field of the fluid (with the exception of the trapped waves that travel down the length of the shell

without decay). In this section, I define a form function for the spherically spreading waves, and I show how I compute this form function in terms of DGM solutions.

First, I solve for the response due to the incident wave acting on the empty shell, using the mathematical details shown above in this appendix. Then, I use the displacements of the empty shell problem to compute the reactions between the shell and the plate, as described in Chapter 4. Finally, I apply those reactions to the shell to compute the scattered field due to the plate, as shown in this section.

In the discussion that follows, the DGM solution discussed is the DGM solution to the reactions of the plate. The pressure caused by the reactions can be found as:

$$p_s(r, \theta, z) = \lambda_N h_N^2 \int_{-\infty}^{\infty} \sum_{m=-\infty}^{\infty} \frac{A_N H_{|m|}^{(1)}(h_r N r) e^{im\theta}}{H_{|m|}^{(1)}(h_r N R_{N-1})} e^{isz} ds$$

where $h_{rN}^2 = h_N^2 - s^2$ from Eq. (2.11), and A_N is the amplitude of the potential for the outermost layer, observed at the outermost interface radius R_{N-1} . Again, note that this is the DGM solution to the reactions, and not the DGM solution to the empty shell problem. Next, substituting the large argument asymptotic form for $H_{|m|}^{(1)}(h_r N r)$ from Eq. (G.6), we have:

$$p_s(r, \theta, z) \rightarrow \lambda_N h_N^2 \int_{-\infty}^{\infty} \sum_{m=-\infty}^{\infty} \frac{\sqrt{2} i^{-|m|} e^{ih_r N r}}{\sqrt{i\pi h_r N r}} \frac{A_N e^{im\theta}}{H_{|m|}^{(1)}(h_r N R_{N-1})} e^{isz} ds \quad (\text{G.10})$$

And, to observe the pressure in the far field at some angle γ from the shell's axis, let $z = R \cos \gamma$ and $r = R \sin \gamma$. Substituting these expressions into Eq. (G.10) and re-arranging, I can write:

$$p_s \rightarrow \frac{\sqrt{2} \lambda_N h_N^2}{\sqrt{i\pi}} \int_{-\infty}^{\infty} \left[\sum_{m=-\infty}^{\infty} \frac{A_N i^{-|m|} e^{im\theta}}{H_{|m|}^{(1)}(h_r N R_{N-1})} \right] \frac{e^{i(s \cos \gamma + h_r N \sin \gamma)R}}{\sqrt{h_r N R \sin \gamma}} ds \quad (\text{G.11})$$

The integral in Eq. (G.11) can be evaluated by the method of stationary phase.

Following the procedures in Junger and Feit (pages 102-104), I define:

$$\begin{aligned}\Psi(s) &\equiv (s \cos \gamma + h_{rN} \sin \gamma)R \\ \Phi(s) &\equiv \left[\sum_{m=-\infty}^{\infty} \frac{A_N i^{-|m|} e^{im\theta}}{H_{|m|}^{(1)}(h_{rN}R_{N-1})} \right] \frac{1}{\sqrt{h_{rN}R \sin \gamma}}\end{aligned}$$

Examining the phase $\Psi(s)$, I find:

$$\frac{\partial \Psi}{\partial s} = R \left[\cos \gamma - \frac{s \sin \gamma}{(h_N^2 - s^2)^{1/2}} \right] \quad \frac{\partial^2 \Psi}{\partial s^2} = -R \sin \gamma \left[\frac{1}{(h_N^2 - s^2)^{1/2}} + \frac{s^2}{(h_N^2 - s^2)^{3/2}} \right]$$

Let \bar{s} be the wavenumber where $\partial \Psi / \partial s = 0$. I find that $\bar{s} \equiv h_N \cos \gamma$. Geometrically, this corresponds to the wavenumber s that launches waves travelling along the angle γ with respect to the shell's axis. Thus, I can also write $h_{rN}|_{s=\bar{s}} = (h_N^2 - \bar{s}^2)^{1/2} = h_N \sin \gamma$. Knowing these things, I can write:

$$\Psi|_{s=\bar{s}} = h_N R \quad \left. \frac{\partial^2 \Psi}{\partial s^2} \right|_{s=\bar{s}} = -\frac{R}{h_N \sin^2 \gamma}$$

Now I can approximate the integral by the method of stationary phase:

$$p_s \rightarrow \frac{\sqrt{2} \lambda_N h_N^2}{\sqrt{i\pi}} \frac{\sqrt{2\pi} \Phi(s) e^{i[\Psi(s) \pm \pi/4]}}{|\partial^2 \Psi(s) / \partial s^2|^{1/2}} \Big|_{s=\bar{s}}$$

I choose the minus sign because $\partial^2 \Psi / \partial s^2$ is negative at $s = \bar{s}$. Thus, I have:

$$p_s \rightarrow \frac{2\lambda_N h_N^2}{\sqrt{i}} \left[\sum_{m=-\infty}^{\infty} \frac{A_N i^{-|m|} e^{im\theta}}{H_{|m|}^{(1)}(h_{rN}R_{N-1})} \right]_{s=\bar{s}} \frac{e^{ih_N R - \pi/4}}{R}$$

Finally, normalizing this, we have:

$$p_s \rightarrow \frac{P_i R_{N-1} e^{ih_{ri}R}}{2R} \left\{ \frac{4\lambda_N h_N^2}{P_i R_{N-1}} \left[\sum_{m=-\infty}^{\infty} \frac{A_N i^{-|m|} e^{im\theta}}{H_{|m|}^{(1)}(h_{rN}R_{N-1})} \right]_{s=\bar{s}} \right\} \quad (\text{G.12})$$

The normalization outside the brackets is the normalization commonly used to define a form function for a spherically spreading field. Thus, we will take the quan-

tity inside the brackets to be the form function for the spherically spreading field emanating from the reactions of the bulkhead.

This page is blank.

Bibliography

- [1] M. C. Junger and D. Feit. *Sound, Structures, and their Interaction*. MIT Press, Cambridge, Massachusetts, 2nd edition, 1986.
- [2] S. Baskar, V. V. Varadan, and V. K. Varadan. Thin shell theories and acoustic wave scattering by infinitely long cylindrical shells of arbitrary cross section. *J. Acoust. Soc. Am.*, **75**:1673–1679, 1984.
- [3] G. C. Gaunaurd and D. Brill. Acoustic spectrogram and complex-frequency poles of a resonantly excited elastic tube. *J. Acoust. Soc. Am.*, **75**:1680–1693, 1984.
- [4] G. C. Gaunaurd and M. F. Werby. Resonance response of submerged, acoustically excited thick and thin shells. *J. Acoust. Soc. Am.*, **77**:2081–2093, 1985.
- [5] N. D. Veksler. The analysis of peripheral waves in the problem of plane acoustic wave scattering by a circular cylindrical shell. *Acustica*, **69**:63–72, 1989.
- [6] N. D. Veksler and V. M. Korsunskii. Analysis and synthesis of backscattering from a circular cylindrical shell. *J. Acoust. Soc. Am.*, **87**:943–962, 1990.
- [7] G. C. Gaunaurd and M. F. Werby. Acoustic resonance scattering by submerged elastic shells. *ASME Appl. Mech. Rev.*, **43**:171–207, 1990.
- [8] A. Akay. Scattering of sound from concentric cylindrical shells. *J. Acoust. Soc. Am.*, **89**:1572–1578, 1991.

- [9] N. H. Sun and P. L. Marston. Ray synthesis of leaky Lamb wave contributions to backscattering from thick cylindrical shells. *J. Acoust. Soc. Am.*, **91**:1398–1402, 1992.
- [10] N. D. Veksler, V. M. Korsunskii, and S. A. Rybak. Scattering of an obliquely incident plane wave by a circular cylindrical shell. *Sov. Phys. Acoust.*, **36**:5–7, 1990.
- [11] F. Léon, F. Lecroq, D. Décultot, and G. Maze. Scattering of an obliquely incident plane wave by an infinite hollow cylindrical shell. *J. Acoust. Soc. Am.*, **91**:1388–1397, 1992.
- [12] J. M. Ho and L. B. Felsen. Nonconventional travelling wave formulations and ray-acoustic reductions for source-excited fluid loaded thin elastic spherical shells. *J. Acoust. Soc. Am.*, **88**:2389–2414, 1990.
- [13] S. G. Kargl and P. L. Marston. Ray synthesis of Lamb wave contributions to the total scattering cross section for an elastic spherical shell. *J. Acoust. Soc. Am.*, **88**:1103–1113, 1990.
- [14] S. G. Kargl and P. L. Marston. Observations and modeling of the backscattering of short tone bursts from a spherical shell: Lamb wave echoes, glory, and axial reverberations. *J. Acoust. Soc. Am.*, **85**:1014–1028, 1989.
- [15] A. Harari. Wave propagation in cylindrical shells with finite regions of structural discontinuity. *J. Acoust. Soc. Am.*, **65**:1196–1205, 1977.
- [16] C. H. Hodges, J. Power, and J. Woodhouse. The low frequency vibration of a ribbed cylinder, Part 1: Theory. *Journal of Sound and Vibration*, **101**:219–235, 1985.
- [17] C. H. Hodges, J. Power, and J. Woodhouse. The low frequency vibration of a ribbed cylinder, Part 2: Observations and interpretation. *Journal of Sound and Vibration*, **101**:237–256, 1985.

- [18] J. D. Achenbach, J. Bjarnason, and T. Igusa. Effect of vibrating sub-structure on acoustic radiation from a cylindrical shell. *ASME*, 1990.
- [19] Y. P. Guo. Sound scattering from an internally loaded cylindrical shell. *J. Acoust. Soc. Am.*, **91**:926–938, 1992.
- [20] A. Klauson and J. Metsaveer. Sound scattering by a cylindrical shell reinforced by lengthwise walls and ribs. *J. Acoust. Soc. Am.*, **91**:1834–1843, 1992.
- [21] A. Harari and B. E. Sandman. Radiation and vibrational properties of submerged stiffened cylindrical shells. *J. Acoust. Soc. Am.*, **88**:1817–1830, 1990.
- [22] M. L. Rumerman. Contribution of membrane wave reradiation to scattering from finite cylindrical steel shells in water. *J. Acoust. Soc. Am.*, **93**(1):55–65, 1993.
- [23] F. Hlawatsch and G. F. Boudreaux-Bartels. Linear and quadratic time-frequency signal representations. *IEEE Signal Processing Magazine*, pages 21–67, 1992.
- [24] L. Cohen. Time-frequency distributions - A review. *Proceedings of the IEEE*, **77**(7):941–981, 1989.
- [25] C. H. Hodges, J. Power, and J. Woodhouse. The use of the sonogram in structural acoustics and an application to the vibrations of cylindrical shells. *Journal of Sound and Vibration*, **101**(2):203–218, 1985.
- [26] C. Corrado. *Mid-Frequency Acoustic Backscattering from Finite Cylindrical Shells and the Influence of Helical Membrane Waves*. PhD thesis, Massachusetts Institute of Technology, 1993.
- [27] A. Leissa. *Vibrations of Shells*. American Institute of Physics, Woodbury, NY, 1993.
- [28] L. Cremer and M. Heckl (translated and revised by E. E. Ungar). *Structure-Borne Sound*, chapter 4, pages 284, 317. Springer-Verlag, 2nd edition, 1988.
- [29] Š. Markuš. *The Mechanics of Vibrations of Cylindrical Shells*, chapter 2, pages 36–101. Elsevier, 1988.

- [30] E. A. Skelton and J. H. James. Acoustics of an anisotropic layered cylinder. *Journal of Sound and Vibration*, **161**(2):251–264, 1993.
- [31] B. L. N. Kennett. *Seismic Wave Propagation in Stratified Media*. Cambridge University Press, 1983.
- [32] W. T. Thomson. Transmission of elastic waves through a stratified solid medium. *J. Appl. Phys.*, **21**:89–93, 1950.
- [33] N. A. Haskell. The dispersion of surface waves on multilayered media. *Bull. Seism. Soc. Am.*, **43**:17–34, 1953.
- [34] B. K. Sinha, T. J. Plona, S. Kostek, and S. K. Chang. Axisymmetric wave propagation in fluid-loaded cylindrical shells. I: Theory. *J. Acoust. Soc. Am.*, **92**:1132–1143, 1992.
- [35] T. J. Plona, B. K. Sinha, S. Kostek, and S. K. Chang. Axisymmetric wave propagation in fluid-loaded cylindrical shells. II: Theory versus experiment. *J. Acoust. Soc. Am.*, **92**:1144–1155, 1992.
- [36] M. Schoenberg, T. Marzetta, J. Aron, and R. P. Porter. Space-time dependence of acoustics waves in a borehole. *J. Acoust. Soc. Am.*, **70**:1496–1507, 1981.
- [37] D. P. Schmitt. Shear wave logging in elastic formations. *J. Acoust. Soc. Am.*, **84**:2215–2229, 1988.
- [38] D. P. Schmitt. Dipole logging in cased boreholes. *J. Acoust. Soc. Am.*, **93**:640–657, 1993.
- [39] H. Schmidt and F. B. Jensen. A full wave solution for propagation in multilayered viscoelastic media with application to Gaussian beam reflection at fluid-solid interfaces. *J. Acoust. Soc. Am.*, **77**:813–825, 1985.
- [40] H. Schmidt. Numerically stable global matrix approach to radiation and scattering from spherically stratified shells. *J. Acoust. Soc. Am.*, **94**(4):2420–2430, 1993.

- [41] F. B. Jensen, W. A. Kuperman, M. B. Porter, and H. Schmidt. *Computational Ocean Acoustics*. American Institute of Physics, New York, 1993.
- [42] H. Kolsky. *Stress Waves in Solids*. Dover Publications, 1963.
- [43] K. F. Graff. *Wave Motion in Elastic Solids*, chapter 2, page 275. Clarendon Press, Oxford, 1975.
- [44] K. Aki and P. O. Richards. *Quantitative Seismology: Theory and Methods*, volume 1, chapter 2, page 64. W. H. Freeman and Company, New York, 1980.
- [45] A. Ben-Menahem and S. J. Singh. *Seismic Waves and Sources*. Springer-Verlag, 1981.
- [46] J. Miklowitz. *The Theory of Elastic Waves and Waveguides*. North-Holland, 1984.
- [47] A. D. Pierce. Wave propagation on thin-walled elastic cylindrical shells. In M. F. McCarthy and M. A. Hayes, editors, *Elastic Wave Propagation*, pages 205–210. Elsevier, New York, 1989.
- [48] L. B. Felsen, J. M. Ho, and I. T. Lu. Three-dimensional Green’s function for fluid-loaded thin elastic cylindrical shell: Formulation and solution. *J. Acoust. Soc. Am.*, **87**:543–553, 1990.
- [49] L. B. Felsen, J. M. Ho, and I. T. Lu. Three-dimensional Green’s function for fluid-loaded thin elastic cylindrical shell: Alternative representations and ray acoustic forms. *J. Acoust. Soc. Am.*, **87**:554–569, 1990.
- [50] L. B. Felsen, J. M. Ho, and I. T. Lu. Erratum: Three-dimensional Green’s function for fluid-loaded thin elastic cylindrical shell: Alternative representations and ray acoustic forms. *J. Acoust. Soc. Am.*, **89**:1463–1464, 1991.
- [51] P. M. Morse and H. Feshbach. *Methods of Theoretical Physics*, chapter 1 and 13, pages 52–54 and 1759–1766. McGraw-Hill, 1953.

- [52] F. W. J. Olver. Bessel functions of integer order. In M. Abramowitz and I. A. Stegun, editors, *Handbook of Mathematical Functions*, chapter 9, pages 355–433. Dover, 1972.
- [53] J. D. Achenbach. *Wave Propagation in Elastic Solids*, chapter 2, pages 74–75. North-Holland and Elsevier, 1975.
- [54] G. Strang. *Linear Algebra and Its Applications*, chapter 1. Academic Press, 2nd edition, 1980.
- [55] D. E. Amos. Algorithm 644: A portable package for Bessel functions of a complex argument and nonnegative order. *ACM Transactions on Mathematical Software*, **12**(3):265–273, 1986.
- [56] J. J. Dongarra and E. Grosse. Distribution of mathematical software via electronic mail. *Communications of the ACM*, **30**(5):403–407, 1987.
- [57] W. H. Press, B. P. Flannery, S. A. Teukolsky, and W. T. Vetterling. *Numerical Recipes in Fortran*, chapter 4, pages 123–158. Cambridge University Press, 2nd edition, 1992.
- [58] J. F. M. Scott. The free modes of propagation of an infinite fluid-loaded thin cylindrical shell. *Journal of Sound and Vibration*, **125**(2):241–280, 1988.
- [59] G. V. Borgiotti and E. M. Rosen. The state vector approach to the wave and power flow analysis of the forced vibrations of a cylindrical shell. part I: Infinite cylinders in vacuum. *J. Acoust. Soc. Am.*, **91**:911–925, 1992.
- [60] F. Fahy. *Sound and Structural Vibration*, chapter 4, page 202. Academic Press, San Diego, California, 1989.
- [61] A. E. H. Love. *A Treatise on the Mathematical Theory of Elasticity*, chapter 8 and 9, pages 183–186 and 209. Dover, 4th edition, 1944.

- [62] C. A. Brebbia and J. Dominguez. *The Boundary Elements: An Introductory Course*, chapter 3 and 5, pages 142–143 and 263–265. Computational Mechanics Publications (Southampton, Boston) and McGraw-Hill (New York), 1989.
- [63] G. D. Manolis and D. E. Beskos. *Boundary Element Methods in Elastodynamics*. Unwin Hyman, London, Boston, 1988.
- [64] I. Dyer. Moment impedance of plates. *J. Acoust. Soc. Am.*, **32**:1290–1297, 1960.
- [65] H. Schmidt and S. Krenk. Asymmetric vibrations of a circular elastic plate on an elastic half space. *International Journal of Solids and Structures*, **18**(2):91–105, 1982.
- [66] S. Timoshenko. *Theory of Plates and Shells*, pages 89–90 and 257. McGraw-Hill, 1st edition, 1940.
- [67] R. D. Mindlin. Influence of rotary inertia and shear on flexural motions of isotropic, elastic plates. *J. Appl. Mech.*, **18**:31–38, 1951.
- [68] P. Ladevèze. *Local Effects in the Analysis of Structures*. Elsevier, 1985.
- [69] D. C. Champeney. *A Handbook of Fourier Theorems*. Cambridge University Press, 1987.
- [70] W. M. Ewing, W. S. Jardetzky, and F. Press. *Elastic Waves in Layered Media*, chapter 2. McGraw-Hill, 1957.
- [71] W. A. Nash. *Strength of Materials*, pages 376–380. McGraw-Hill, 2nd edition, 1972.
- [72] C. Wang. *Applied Elasticity*, pages 50–54. McGraw-Hill, 1953.
- [73] P. M. Morse and K. U. Ingard. *Theoretical Acoustics*, chapter 1, pages 12–13. Princeton University Press, 1968.
- [74] R. Zucker. Elementary transcendental functions. In M. Abramowitz and I. A. Stegun, editors, *Handbook of Mathematical Functions*, chapter 4. Dover, 1972.